Ferrite-based micro-inductors for Power Systems on Chip: from material elaboration to inductor optimisation

Thi Yen Mai Nguyen

THÈSE

En vue de l'obtention du

DOCTORAT DE L'UNIVERSITÉ DE TOULOUSE

Délivré par *Université Toulouse 3 Paul Sabatier (UT3 Paul Sabatier)*
Discipline ou spécialité : *Micro-nano systems*

Présentée et soutenue par *NGUYEN Thi Yen Mai*
Le *Mardi 9 Décembre 2014*

Titre : *Ferrite-based micro-inductors for Power Systems on Chip: from material elaboration to inductor optimisation*

Rapporteurs

LABOURE Eric, Université Paris Sud
ROY Saibal, Tyndall Institute

Ecole doctorale : *GEET*

Unité de recherche : *LAAS, CNRS*

Directeur(s) de Thèse :

BRUNET Magali, LAAS, CNRS
LAUR Jean-Pierre, LAAS, CNRS

Autre(s) membre(s) du Jury :

VALDEZ-NAVA Zarel, LAPLACE, CNRS
LEFRANC Pierre, G2E Lab
PARRA Thierry, UT3 Paul Sabatier
VOIRON Frédéric, IPDiA

Acknowledgement

This PhD thesis was carried out within the group of Power Management System Integration (ISGE) at Laboratory for Analysis and Architecture of Systems (LAAS) in collaboration with Laboratory on Plasma and Conversion of Energy (LAPLACE) and with the group of Power Electronics at Grenoble Electrical Engineering Laboratory (G2E lab).

Foremost, I thank the successive heads of the LAAS-CNRS, Raja Chatila, Jean Louis Sanchez and Jean Arlat who welcomed me during those three years of research. Then, I would like to thank Marise Bafleur and Frédéric Morancho, the successive heads of ISGE, for welcoming me in the group and enabling me to undertake my research.

I would like to express the deepest appreciation to my supervisors, Magali Brunet and Jean-Pierre Laur (LAAS). I am grateful for their time, ideas and offered funding to establish and enrich my PhD experience. Without their persistent support this dissertation would not have been accomplished.

I would like to thank Zarel Valdez-Nava, Vincent Bley and Céline Combettes (LAPLACE) for their cooperation in the magnetic materials. They gave me many advices and help for the fabrication of the ferrites and the ferrite pastes and also welcomed me at their laboratory for processing the magnetic materials. I thank Pascal Dufour and Marie-Claire Barthelemy (CIRIMAT) for the magnetic material fabrication and the TMA measurements. I would also like to thank Pierre Lefranc (G2E lab) for his guidance in simulation and optimization. He is always patient to explain the inductor modeling to me. Their contribution made my thesis.

During my PhD, working in the clean room needed lots of aid from the technicians. I would like to thank especially David Bourrier for his work in metal electro-deposition, Samuel Charlot for the process of screen printing, wire bonding and flip chip testing, David Colin for the process of cutting and polishing wafers, Jean-Christophe Marrot for the process of sintering, Ludovic Salvagnac for the process of metal deposition, Pierre-Francois Calmon for his fabrication of masks, Franck Carcenac for the training of SEM and EDX, Adrian Laborde and Laurent Mazenq for the training of the photolithography process and thank Monique Benoit for the supply of the experimental instruments.

I would like to thank Nicolas Mauran for his training and help in electrical measurements. I am grateful to his solutions for the problem in the equipment of measurement.

I also thank Claude Laffore, Ascension De Sousa Berdat, the successive secretaries of ISGE, Camille Cazeneuve, Claire Bardet (Personnel LAAS), Marie-Thérèse Funch (CNRS Delegation) and Marie Estruga (GEET) for helping me in administrative affairs.

I would like to acknowledge the funding sources of my PhD, PRIIM project.

Finally, I would like to thank my husband Dac-Kien Lai for his encouragement and his understanding of my research. I would like to express my gratitude to my Vietnamese friends for pleasant time we had together in Toulouse.

Toulouse, 24th January 2015

Yen Mai Nguyen

“Stay hungry. Stay foolish”

Steve Jobs, former CEO of Apple Computer and of Pixar Animation Studios

June 12, 2005

To my friends, my husband and my family

Toulouse 26th January 2015

Yen Mai Nguyen

Title: Ferrite-based micro-inductors for Power Systems on Chip: from material elaboration to inductor optimisation

Abstract:

On-chip inductors are key passive elements for future power supplies on chip (PwrSoC), which are expected to be compact and show enhanced performance: high efficiency and high power density. The objective of this thesis work is to study the material and technology to realize small size (<4 mm²) and low profile (< 250 µm) ferrite-based on-chip inductor. This component is dedicated to low power conversion (≈ 1 W) and should provide high inductance density and high quality factor at medium frequency range (5-10 MHz). Fully sintered NiZn ferrites are selected as soft magnetic materials for the inductor core because of their high resistivity and moderate permeability stable in the frequencies range of interest. Two techniques are developed for the ferrite cores: screen printing of in-house made ferrite powder and cutting of commercial ferrite films, followed in each case by sintering and pick-and place assembling to form the rectangular toroid inductor. Test inductors were realized first so that the characterization could be carried out to study the magnetic properties of the ferrite core and the volumetric core losses. The core losses were fit from the measured curve with Steinmetz equation to obtain analytical expressions of losses versus frequency and induction. The second phase of the thesis is the design optimization for the on-chip ferrite based inductor, taking into account the expected losses. Genetic algorithm is employed to optimize the inductor design with the objective function as minimum losses and satisfying the specification on the inductance values under weak current-bias condition. Finite element method for magnetics FEMM is used as a tool to calculate inductance and losses. The second run of prototypes was done to validate the optimization method. In perspective, processes of thick-photoresist photolithography and electroplating are being developed to realize the completed thick copper windings surrounding ferrite cores.

Résumé:

Les composants passifs intégrés sont des éléments clés pour les futures alimentations sur puce, compactes et présentant des performances améliorées: haut rendement et forte densité de puissance. L'objectif de ce travail de thèse est d'étudier les matériaux et la technologie pour réaliser de bobines à base de ferrite, intégrées sur silicium, avec des faibles empreintes (<4 mm ²) et de faible épaisseur (<250 µm). Ces bobines, dédiées à la conversion de puissance (≈ 1 W) doivent présenter une forte inductance spécifique et un facteur de qualité élevé dans la gamme de fréquence visée (5-10 MHz). Des ferrites de NiZn ont été sélectionnées comme matériaux magnétiques pour le noyau des bobines

en raison de leur forte résistivité et de leur perméabilité stable dans la gamme de fréquence visée. Deux techniques sont développées pour les noyaux de ferrite: la sérigraphie d'une poudre synthétisée au laboratoire et la découpe automatique de films de ferrite commerciaux, suivi dans chaque cas du frittage et le placement sur les conducteurs pour former une bobine rectangulaire. Des bobines tests ont été réalisées dans un premier temps afin que la caractérisation puisse être effectuée : les propriétés magnétiques du noyau de ferrite notamment les pertes volumiques dans le noyau sont ainsi extraites. L'équation de Steinmetz a permis de corréler les courbes de pertes mesurées avec des expressions analytiques en fonction de la fréquence et de l'induction. La deuxième phase de la thèse est l'optimisation de la conception de la micro-bobine à base de ferrite, en tenant compte des pertes attendues. L'algorithme générique est utilisé pour optimiser les dimensions de la bobine avec pour objectif ; la minimisation des pertes et l'obtention de la valeur d'inductance spécifique souhaitée, sous faible polarisation en courant. La méthode des éléments finis pour le magnétisme FEMM est utilisée pour modéliser le comportement électromagnétique du composant. La deuxième série de prototypes a été réalisée afin de valider la méthode d'optimisation. En perspective, les procédés de photolithographie de résine épaisse et le dépôt électrolytique sont en cours de développement pour réaliser les enroulements de cuivre épais autour des noyaux de ferrite optimisés et ainsi former le composant complet.

Table of contents

List of publication:

1) Low-profile small-size ferrite cores for powerSiP integrated inductors

Authors: Yen Mai Nguyen[1,3], Magali Brunet[1,3], Jean-Pierre Laur[1,3], David Bourrier[1,3], Samuel Charlot[1,3], Zarel Valdez-Nava[2,3], Vincent Bley[2,3], Céline Combettes[2,3]

1. CNRS, LAAS, 7 avenue colonel Roche, F-31400 Toulouse, France
2. CNRS, LAPLACE (Laboratoire Plasma et Conversion d'Energie), 118 route de Narbonne, F-31062 Toulouse, France
3. Université de Toulouse; UPS, INPT; LAAS, LAPLACE, Toulouse, France

Conference: European Conference on Power Electronics and Applications (EPE) 2013, 03-05 September, Lille (France)

2) Soft ferrite cores characterization for integrated micro-inductors

Authors: Yen Mai Nguyen[1,3], Thomas Lopez[1], Jean-Pierre Laur[1,3], David Bourrier[1,3], Samuel Charlot[1,3], Zarel Valdez-Nava[2,3], Vincent Bley[2,3], Céline Combettes[2,3], Magali Brunet[1,3]

[1]CNRS, LAAS, 7 avenue colonel Roche, F-31400 Toulouse, France
[2]CNRS, LAPLACE, 118 route de Narbonne, F-31062 Toulouse, France
[3]Université de Toulouse; UPS, INPT; LAAS, LAPLACE, Toulouse, France

Conference: International Conference on Micro and Nanotechnology for Power Generation and Energy Conversion Applications (PowerMEMS) 2013, 03-06 December, London (UK)

3) Soft ferrite cores characterization for integrated micro-inductors (published)

Authors: Yen Mai Nguyen[1,3], David Bourrier[1,3], Samuel Charlot[1,3], Zarel Valdez-Nava[2,3], Vincent Bley[2,3], Céline Combettes[2,3], Thomas Lopez[1], Jean-Pierre Laur[1,3] and Magali Brunet[1,3]

[1] CNRS, LAAS, 7 avenue colonel Roche, F-31400 Toulouse, France
[2] CNRS, LAPLACE, 118 route de Narbonne, F-31062 Toulouse, France
[3] Université de Toulouse; UPS, INPT; LAAS, LAPLACE, Toulouse, France

Journal : Journal of Micromechanics and Microengineering JMM, IOP Publishing

4) Modeling and design optimization of micro-inductor using genetic algorithm

Authors: Yen Mai nguyen[1], Pierre Lefranc[2], Jean-Pierre Laur[1], Magali Brunet[1]

[1]CNRS, LAAS, 7 avenue colonel Roche, Toulouse, France
[2]CNRS, G2Elab, F-38000 Grenoble, France

Conference: International Power Supply On Chip Workshop (PwrSoC) 2014, October 6-8, Boston (USA)

General introduction

Miniaturization of electronic devices has been attracting lots of research and development since the 60's. Power system is one of the important parts in electronic equipments including power source and power management. That refers to the generation and control of regulated voltages required to operate an electronic system. One major requirement for the power supply is high efficiency. Integrated circuit components such as DC/DC converters (step-down or step-up), voltage regulator and battery management are typical elements of power management. Figure 0-1 presents a generic distributed power management system in a mobile phone. In this general picture, this thesis will focus on the integrated inductor which is a part of a DC/DC converter.

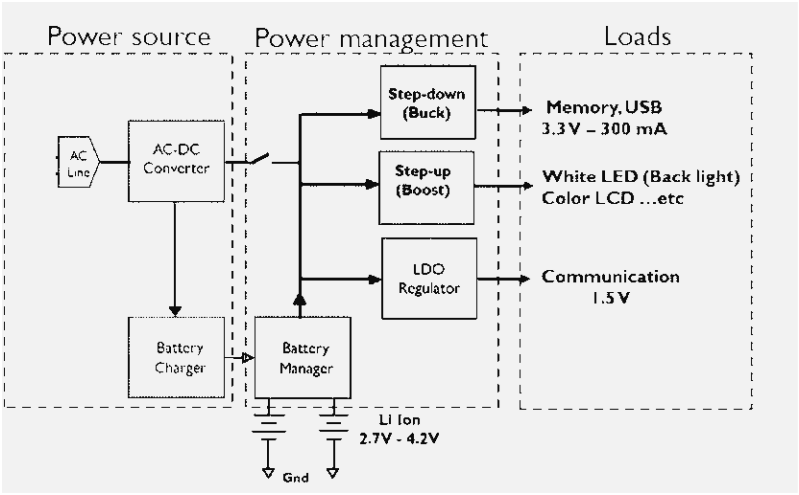

Figure 0-1: A generic distributed power management system in a cell phone

Buck and Boost converters are switched-mode power supplies that provide respectively lower and higher output voltages than the input voltages. These converters use at least two electronic switches (a diode and a transistor) and at least two energy storage elements, an inductor and a capacitor. Figure 0-1 shows a buck converter schematic and the two equivalent diagrams in the continuous mode operation. The inductor ensures the current filtering and the capacitor allows low output voltage ripples. The energy is stored in the inductor and capacitor at the "+.state", and is released at the "-.state". Inductors store the magnetic energy while capacitors store electrical energy. Historically, the standard for supply voltage was about ± 15V for a great number of electronic equipment. In recent years, the trend is towards lower supply voltages with higher switching frequencies. This is partially due to the process used to manufacture integrated circuits and the technology which allows reducing the size of transistors. These smaller sizes imply lower breakdown voltages which drive supply voltages to lower values. Reducing the supply voltage has a desirable effect of reducing the power dissipation of digital circuits [1].

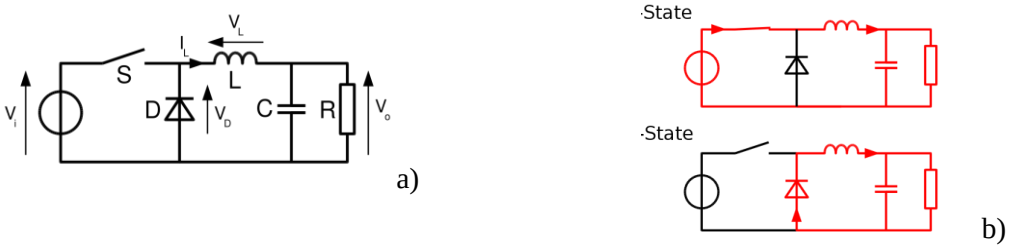

Figure 0-1: a) Buck converter schematic and b) equivalent diagrams in the continuous mode[2]

Non-isolated DC/DC converters are used in DC distributed power systems and directly built on the mother board next to the load. They are also called point-of-load (POL) converters. In order to achieve high efficiency, POL converters usually operate at a frequency lower than 1 MHz, in the range 100–600 kHz. Nowadays, mobile electronic devices such as smart-phones and tablets continue to require smaller point-of-load converters while maintaining high power conversion efficiency and a high power density for their numerous functions like image processing, voice recognizing, etc… There are many groups and companies doing research for the power solutions and there is huge improvement in last decades as we can observe clearly and lively in smart phones.

The passive components such as inductors in POL converters are bulky occupying a considerable footprint. In order to make POL converter smaller, it is necessary to: (i) increase significantly the switching frequency to reduce the size and weight of the inductors (ii) integrate the inductor effectively in a small footprint. The latest trend of POL converter is to integrate the inductor providing minimum footprint and profile; the operating frequency goes thus to higher range, typically few MHz to fulfill the high level of integration. So, the size of the POL converter becomes compatible with power Integrated Circuit (IC) dimensions in a new miniaturized product formats that can be referred to as power supply in package (PowerSiP) and power supply on chip (PowerSoC). In a power supply in package, the discrete passives and the IC are assembled side by side or stacked on each other beside other components in the converter. In an ultimate power supply on chip, the passives are monolithically integrated onto the power management IC. The development of high-frequency integrated power supply requires multidisciplinary researches combining the knowledge of different areas like semiconductor devices, converter design and magnetic materials. In this thesis, we are targeting inductors integrated on-chip, also called micro-inductors.

From state of the art of commercial converters and commercial integrated inductors, see Table 0-1 and Table A1-1 in the Annexes, we can determine where we are today from a technological standpoint, what the trends are, and what will be necessary to achieve integrated inductor for POL converters in the future. At the moment, almost all power supplies are with bulky inductors embedded in the package, very few of them are on chip. EP5348UI Enpirion® is a 400mA PowerSoC which integrates MOSFET switches, control, compensation, and the magnetics in a micro-QFN Package in a dimension

of 2.0mm x 1.75mm x 0.9mm, see Table 0-1 for more details. The EP5348UI offers a good compromise between the footprint and the efficiency to replace less efficient low-dropout regulators in space-constrained applications that require improved efficiency. For the power supply on chip, the power density is not very high, with low inductance density inductor. **In this thesis, we will focus on integration technology for inductors dedicated to low power (≈ 1 W) DC/DC converters with high power densities, high efficiencies (above 90%) and medium frequency (5-10 MHz).** We choose the medium frequency range because in the overall power system, we believe that with higher frequencies, switching losses and consumption of control devices will be too large and that might degrade the overall system efficiency. Within these application specifications, we will focus specifically on high power density inductors and their integration technology. We try to find simple feasible solutions for manufacturing together with high performance of inductor. The analysis for integrated inductors is broken down into three main issues: *(i) what magnetic material to choose for integrated inductors? (ii) what technology to fabricate? and (iii) how to design effectively?*

Table 0-1: Examples of commercial low-profile converters with embedded inductors

Year	2012	2012	2012	2009 -2011	2012
Institution/ Company	Murata	Altera's Enpirion	On Semi-conductor	Texas Instrument	Texas Instrument
Product	LXDC2HL	Enpirion EP5348UI	NCP6332	LM8801	TPS81256
Converter	Buck	Buck	Buck	Buck	Boost
Size (mm^3)	2.7x2.2x 1.1	2x1.75x 0.9	2x2x 0.75	1.07 x 1.27 x 0.6 < $7mm^2$	2.9x2.6x1
Output power (W)	1.25	2	6	1.7	5
Power density approx. ($W.cm^{-3}$)	190	600	2000	-	660
V_{in} (V)	2.3 to 5.5	2.5 to 5.5	2.3 to 5.5	2.3 to 5.5	2.5 to 4.85
V_{out} (V)	0.8 to 4	0.6 to V_{in}- V_{drop}	0.6 to V_{in}	1 to 2.9	4.85 to 5.2
I_{out} (A)	Max 0.6	0.4	1.2	Max 0.6	Max I_{in} 1.05
Efficiency (%)	Max 90%	Max 90%	Max 90%	90%	91%
Frequency (MHz)	3	9	3	6	4
Inductor				Not embedded	
Inductance	-	120nH	1µH	0.47µH	1µH
DC resistance (mΩ)	-	< 780	-	-	< 320
Technology	PowerSiP, Ferrite, inductor size 2.7x2.2x 0.7 mm^3	PowerSoC	PowerSiP	PowerSiP	PowerSiP

References

1. Analog Devices Inc. and H. Zumbahlen, *Linear Circuit Design Handbook, 2011* Elsevier Science.
2. N. Mohan, T. M. Undeland, and W. P. Robbins, *Power Electronics: Converters, Applications and Design, 3rd Edition*, 2003 Wiley.

Chapter 1 State of the art of integrated inductor

This chapter presents basic formula concerning inductors and the state of the art of integrated inductor in research considering different inductor structures, magnetic materials and processing technologies for cores.

1. Basic formulas for micro-inductors with magnetic core

1.1. Magnetic material

- Static magnetic permeability of a material

$$\mu = \frac{B}{H} = \mu_0 * \mu_r \qquad \textit{(Eq. 1.1)}$$

B is magnetic induction (T), H is the external magnetic field (A/m), μ_0 is vacuum permeability = $4\pi.10^{-7}$ (H/m) and μ_r is the relative permeability of the material.

- Complex permeability as function of frequency

When the magnetic material is exposed in an external alternating field $H = H_0 \exp(j\omega t)$, where $\omega = 2\pi f$ the frequency of oscillations and t is the time, the magnetic losses of the material are expressed by the phase discrepancy between B and H. To explain this phenomenon, we write the initial permeability in the complex form:

$$\mu_{(\omega)} = \frac{B_{(\omega)}}{H_{(\omega)}} = \frac{B_0 e^{j(\omega t-\delta)}}{H_0 e^{j\omega t}} = \frac{B_0}{H_0} e^{-j\delta}$$

$$\mu_{(\omega)} = \frac{B_0}{H_0}\cos\delta - j\frac{B_0}{H_0}\sin\delta$$

$$\mu_{(\omega)} = \mu'(\omega) - j\mu''(\omega) = \mu_0[\mu_r'(\omega) - j\mu_r''(\omega)] \qquad \textit{(Eq. 1.2)}$$

$\mu'(\omega)$ represents the reactive part of the initial permeability, $\mu''(\omega)$ is the dissipative part corresponding to magnetic losses. Magnetic losses are also represented by $\tan(\delta)$ which is the ratio of the dissipative part and the reactive part of the permeability:

$$\tan(\delta) = \frac{\mu''(\omega)}{\mu'(\omega)} = \frac{\mu_r''(\omega)}{\mu_r'(\omega)} \qquad \textit{(Eq. 1.3)}$$

1.2. Micro-inductor

A coil such as the one shown in Figure 1-1 has a self-inductance or inductance L, which is defined as:

$$L = \mu_0\mu_r' N^2 \frac{A_e}{l_e} \text{ (H)} \qquad \textit{(Eq. 1.4)}$$

Where N is number of turns, A_e is magnetic cross section, l_e is mean magnetic length.

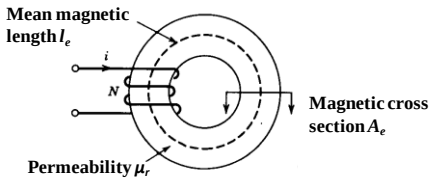

Figure 1-1: Schematic of a magnetic coil [1]

When we excite the coil with an alternating current I_{AC}, the alternating magnetic induction created in the magnetic core can be defined as

$$B_{AC} = \frac{L\, I_{AC}}{N\, A_e} \text{ (T)} \qquad \textit{(Eq. 1.5)}$$

When there is a continuous current I_{DC} in the winding conductor, the DC pre-magnetized field present in the magnetic core can be expressed as

$$H_{DC} = \frac{N\, I_{DC}}{l_e} \ (A/m) \qquad \textit{(Eq. 1.6)}$$

Magnetic energy stored in the inductor can be determined from the DC current as following

$$W_{magnetic}(t) = \frac{Li_{(t)}{}^2}{2} \qquad \textit{(Eq. 1.7)}$$

Quality factor Q of an inductor gives an indication of its performance in the circuit. It is dimensionless and indicates the energy losses relative to the energy stored within the inductor.

$$Q = \omega \frac{L}{R_{AC}} \qquad \textit{(Eq. 1.8)}$$

1.2.1. Copper losses in winding

Copper losses are a considerable portion of the total losses of the inductor and can be calculated by multiplying the resistance by the square of the rms current. However, when a high frequency current flows in a conductor, eddy currents induced in the winding lead to an increase of the conductor resistance and consequently to an increase of copper losses. Skin and proximity effects are highly frequency-dependent and must be considered for accurate losses prediction.

- Skin effect: when operating at high frequency, the current lines have the tendency to concentrate near the surface of the conductor with a thickness called skin depth δ_ω expressed as $\delta_\omega = \sqrt{\rho/\pi f \mu}$, in which ρ is resistivity of the conductor, f is excitation frequency, and $\mu = \mu_0\mu_r$ is permeability of the conductor material.
- Proximity effect: a current flowing in adjacent conductors creates a magnetic field which modifies the current line distribution in the conductor.

The influence of both skin and proximity effects must be modeled by an equivalent resistance R_{AC} of the conductor that causes losses proportional to $R_{AC}I_{ACrms}^2$, where I_{ACrms} is the rms value of the alternating current.

Regarding analytical expression, the Dowell equation is a generalized form of the solution for the diffusion equation of rectangular conductors adapted and applied to round conductors [2]. In this equation, instead of calculating losses directly, the AC resistance of the conductor is calculated. The ratio of the AC resistance to the DC resistance F_R can be calculated using the Dowel method.

$$F_R = \frac{R_{AC}}{R_{DC}} \qquad \textit{(Eq. 1.9)}$$

The graph of F_R vs. frequency shows us how quickly the resistance increases with the frequency [3]. A good design will obtain a small ratio F_R (ideally about 1) at the operating frequency.

1.2.2. Core losses in inductor

The core losses are due to magnetic materials in the inductor. There are three mechanisms for core losses:

- Hysteresis losses: when the excitation of magnetic field is alternating $H = H_0\exp(j\omega t)$ the magnetic material stores magnetic energy but does not return totally when H is reversed. The volumetric hysteresis losses correspond to energy dissipated in one hysteresis cycle and can be expressed as

  $$P_{hys} = \int_0^{Bmax} HdB \ (W.m^{-3}) \qquad \textit{(Eq. 1.10)}$$

  Total hysteresis losses depend on the operating frequency and are determined by the following expression

  $$P_{HYS} = K_H f^{\alpha_H} B_{ACm}^{\beta_H} \qquad \textit{(Eq. 1.11)}$$

  Where H is the magnetic field generated by the electrical excitation and B_{ACm} is the maximal magnetic induction, K_H and α_H, β_H are hysteresis losses coefficients. At low frequency, the hysteresis losses are sometime expressed as [4]

  $$P_{HYS} = K_H f B_{ACm}^2$$

- Eddy current losses: are losses due to the current induced in the core by a magnetic field, which depend on frequency, magnetic induction and the resistivity of the core material. Analytical expression of eddy current losses is given in the following equation:

$$P_{eddy} = C\frac{f^{\alpha_E} B_{ACm}{}^{\beta_E}}{\rho}(W.m^{-3}) \qquad (Eq.\ 1.12)$$

Where C is a coefficient which depends on the size of material and the form of alternating signal, α_E, β_E are eddy current losses coefficients.

- Resonance-relaxation losses/Residual losses: These losses are maximal when the functional frequency is close to resonance frequency of material identified by the maximum of $\mu_r''(\omega)$.

Concerning analytical expression, the Steinmetz equation is used to calculate core losses when the magnetic field is sinusoidal. The basic form of Steinmetz equation is

$$P_{core} = Kf^{\alpha} B_{ACrms}{}^{\beta}(mW.cm^{-3}) \qquad (Eq.\ 1.13)$$

Where P_{core} is the volumetric core loss, f is frequency of sinusoidal waveform, B_{ACrms} is the flux density inside the core, α, β and K are coefficients specific to each type of core and usually determined by curve fitting to the experimental curve. Once the Steinmetz parameters have been identified, it is straightforward to calculate core losses. Losses identified by Steinmetz equation include hysteresis, eddy current and residual losses. A limitation is that this equation is only good for sinusoidal excitation. In order to work with other different wave forms, recent developments try to modify SE equation, for example Modified Steinmetz Equation, Generalized Steinmetz Equation and Improved Generalized SE [5].

1.3. Micro-inductor in Buck converter

In the continuous mode conduction, the current wave form in the inductor is triangular as depicted in Figure 1-2.

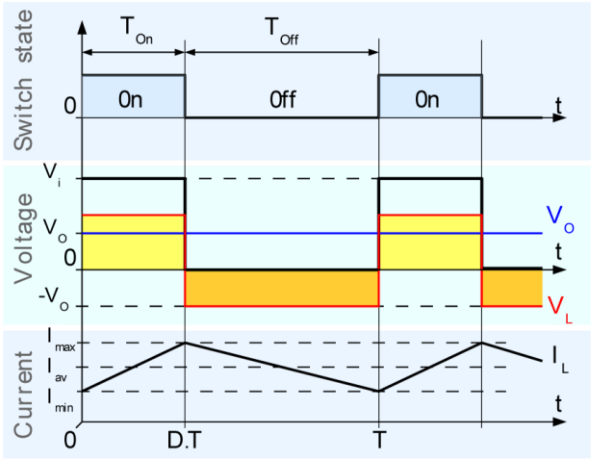

Figure 1-2: Inductor current wave-form in a Buck converter [1]

The value of inductance is fixed by the ripple current by the relation

$$\Delta I_L = \frac{D(1-D)*V_{in}}{f*L} \qquad \textit{(Eq. 1.14)}$$

Where *D* is duty cycle $D = \frac{V_{out}}{V_{in}}$. Ripple current is the AC triangular current flowing through the inductor.

The DC current is determined by the ratio of output power and voltage

$$I_{DC} = \frac{P_{out}}{V_{out}} \qquad \textit{(Eq. 1.15)}$$

However, when the inductor contains a magnetic core, at high current values, saturation phenomenon can occur. The inductor can operate indeed at the maximum magnetic induction B_{ACm} with $B_{ACrms} < B_{sat}$, where B_{sat} is the saturation induction of the magnetic core. Above B_{sat}, the permeability of the magnetic core is asymptotic to zero; the inductance drops consequently to a value close to an air-core inductor.

2. Literature review on integrated micro-inductors

The evolution of micro-inductors and the development of magnetic thin films can be traced back to the early studies in the late 1960s. However, significant developments in the area were reported from the early 1990s. Different research teams have been working on the development of integrated power converters for the last 20 years, with particular emphasis on integrated planar magnetic components. They use different materials, processing methods, and structures to fabricate micro-magnetic devices which we will review hereafter [6].

2.1. Micro-inductor structures

The design of a micro-inductor includes the windings and the core with consideration to inductance, resistance, efficiency or losses, size or footprint, and fabrication processes. Power inductors typically employ a magnetic core to enhance the inductance. Depending on the arrangement of conductors with respect to the magnetic core, the construction of a micro-inductor can be categorized into two different approaches. The first approach is to enclose the planar coils with a magnetic material. The second approach is to wrap the conductor around a planar magnetic core using a multilayer metal scheme. The main structures using the first approach are spiral inductors, racetrack inductors. The typical structures using the second approach are solenoid inductors and toroidal inductors. **Key output parameters of interest for design are high inductance densities, low DC and AC resistances, relatively high current withstanding, low core losses at the operating frequency**. The input parameters like material properties of magnetic core and conductor, the dimension of the core and windings, and

excitation currents at operation frequency will determine the performance of the inductor. The state-of-the-art integrated inductors are referenced in the Annex, Table A1-2a and b, Table A1-3, Table A1-4 and Table A1-5a and b. Their performances in term of inductance, footprint, resistance, maximum current, maximum frequency are listed in the tables. Thereafter, we report some examples of the four possible structures extracted from the state-of-the-art, i.e. spiral, racetrack, solenoid and toroidal.

The spiral type is a popular-researched structure to form a planar inductor. The copper windings are completely surrounded in magnetic material to achieve the required inductance. Spiral coils can be miniaturized more easily than other structures due to the ease of micro fabrication. In spiral inductor, the interconnection of multilevel conductor is not required and therefore, the micro fabrication is simpler. The shape of spiral inductor can be circular, square or hexagonal. The spiral inductor can stand a high DC current due to low concentrated magnetic flux. In 2013, Sugawa from Shinshu University presented carbonyl-iron powder (CIP)/epoxy based hybrid inductor on the glass substrate for large current application [7] (see Figure 1-3). The inductor is in 1-mm-square with 5.5nH of inductance and 18mΩ DC resistance of coil, the superimposed current can be up to 5.5A. The main drawback is that the inductance density of spiral inductor is limited. For anisotropic magnetic material, it is difficult to induce anisotropy in the magnetic core during core deposition. Another disadvantage is that it requires a long copper winding to make a turn, i.e. the DC resistance of spiral inductor is typical high.

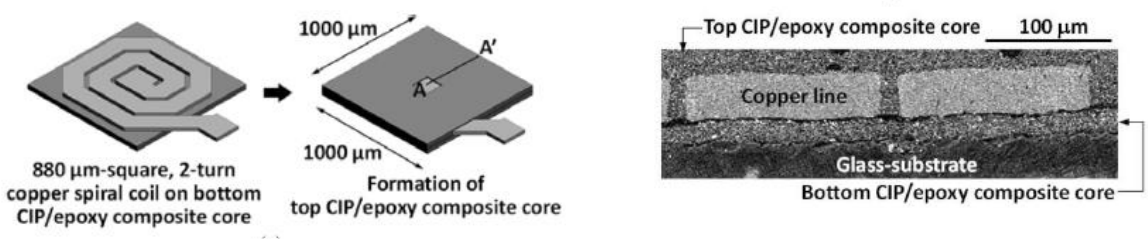

Figure 1-3 : Typical spiral structure with a planar coil and two layers of magnetic material, Shinshu University, in 2013 [7]

A racetrack inductor can be formed by stretching a circular spiral inductor. The magnetic core will typically be used to wrap the straight part of coils, hence take advantage of the uniaxial anisotropy of the magnetic material. A magnetic easy axis and hard axis can be generated during or after the deposition of cores in rectangular shape using an external magnetic field. Racetrack micro-inductors have been demonstrated in various Buck converters at high frequencies up to 100 MHz [6]. Compared to the square or circular shaped spiral inductors, the racetrack micro-inductors are more suited for power converters because its shape is long and rectangular and so, the easy axis orientation is not difficult. The losses due to the easy-axis hysteresis loop are smaller for racetrack inductors. In 2013,

Harburg presented a CoZrO-based racetrack inductor [8], see Figure 1-4. The magnetic layer is 20 µm thick and deposited by sputtering using shadow masks. The inductor offered an inductance of 1.1 µH and a DC resistance of 0.84 Ω at 8.3 MHz in a footprint of about 25 mm^2.

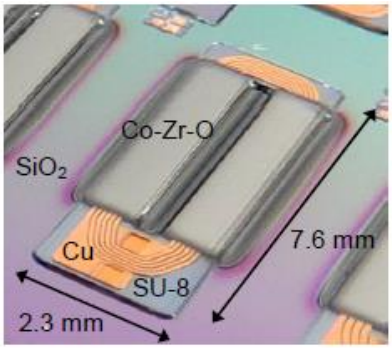

Figure 1-4 : Racetrack inductor fabricated on silicon with a 20-µm-thick Co-Zr-O magnetic core surrounding SU-8 insulated copper winding, Thayer school of engineering Dartmouth, USA , in 2013[8]

The toroidal structure is a widely used structure to fabricate micro-inductors, using multilevel metal schemes to wrap around a magnetic core. The toroidal structure has a closed magnetic path; therefore, the magnetic flux is concentrated in the magnetic core. As a consequence, the inductance density of the toroidal inductor is high. The closed magnetic path helps also reducing magnetic interference to neighbouring component. The length of conductor for one turn of winding is relatively short for toroidal structure; hence it is an advantage for toroidal inductors concerning DC resistance. However, with high concentrated magnetic flux, the rated current for toroidal inductors is often small unless the magnetic core has a high saturation induction (B_{sat}) or a low permeability to avoid saturation. In the toroidal-core design, connecting the bottom and top layers of conductor to encircle the core is difficult. This requires a proper interconnection between copper layers i.e. low-resistance contact and a connection over a vertical distance equal to the thickness of the core. Low-resistance contacts over a large vertical distance around the core are achieved by electroplated vias with carefully cleaned contact surfaces. It was demonstrated by Flynn et al. that flip-chip bonding could successfully bond the bottom and top copper winding to form toroidal inductor with small DC resistance: 100mΩ for an air-core inductor [9]. The copper windings were 90 µm-thick and 200 µm-wide. A similar inductor with electroplated Ni-Fe core is shown in Figure 1-5. The inductors showed high inductance values 0.3-1.7µH; however, the saturation current was smaller than 0.14 A and the cut-off frequency was smaller than 1 MHz. More details of the inductor performance are presented in Table A1-5a.

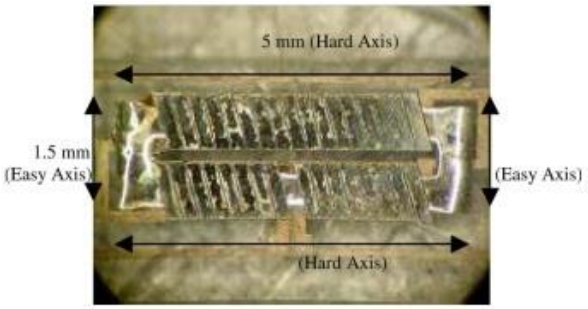

Figure 1-5 : Fabricated Ni-Fe based micro-inductor of approximately 5 mmx2 mmx0.25 mm, Herriot Watt University, Scotland, in 2009 [9]

The solenoid structure uses a bar shape magnetic core as opposed to a toroidal core. A bar of magnetic material is placed in the centre of the device, and the windings surround it. The solenoid structure doesn't have a closed magnetic path and hence the inductance density is limited. The leakage flux at the two ends of the solenoid is considerable and losses are high. In 2008, Lee presented a solenoid inductor (see Figure 1-6) with an inductance of about 70 nH, a device area of 0.88 mm^2. The inductance density was not very high: about 80nH.mm^{-2} [10].

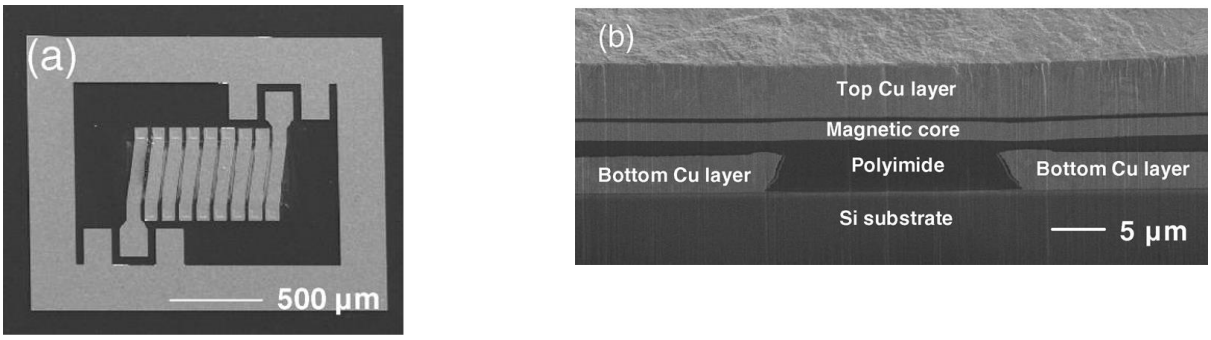

Figure 1-6 : (a) Solenoid inductor with 8.5 turns (b) Cross-section of solenoid inductor, Stanford University, in 2008 [10]

In 2008, 2011, Shen's group proposed a simple approach to form solenoid inductors in which existing bond wires are encapsulated in a ferrite filled epoxy core [11, 12]. Bond-wire inductors fabricated on PCB are shown in Figure 1-7. This approach can be easily adapted for realizing inductors on PCB, on-chip or in-package using aluminum or gold bond wire of 25– 280 µm diameter. This technology has been demonstrated in a 5-MHz Buck converter. However, the reported measured efficiency is low, only 52% i.e. losses are very high which may be due to the magnetic core itself or the inductor structure. The drawback of this technology is the low resolutions of the magnetic core fabrication.

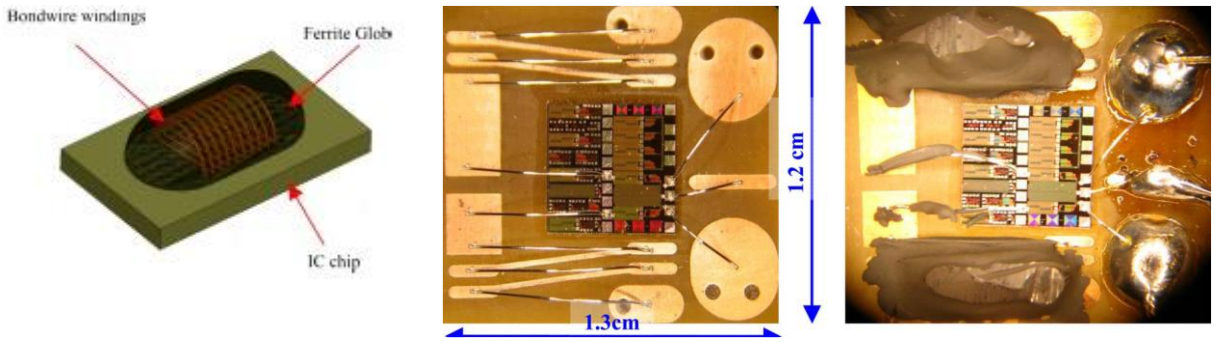

Figure 1-7 : Concept of multi-turn bond-wire inductor with ferrite epoxy globe core (image on the left), top view of the PSiP buck converter before (image at the middle) and after (image on the right) the ferrite globe cores were applied [11, 12]

Recently, the air-core inductors have been studied with multiple winding stacks by Christophe Meyer's group [13, 14]. These spiral air-core inductors have inductance of 100-130nH up to 100 MHz, see Figure 1-8. Their DC resistance is relatively high about 0.8Ω, and the resistance is about 50Ω at 100MHz. It is a disadvantage considering the losses, especially at high frequency.

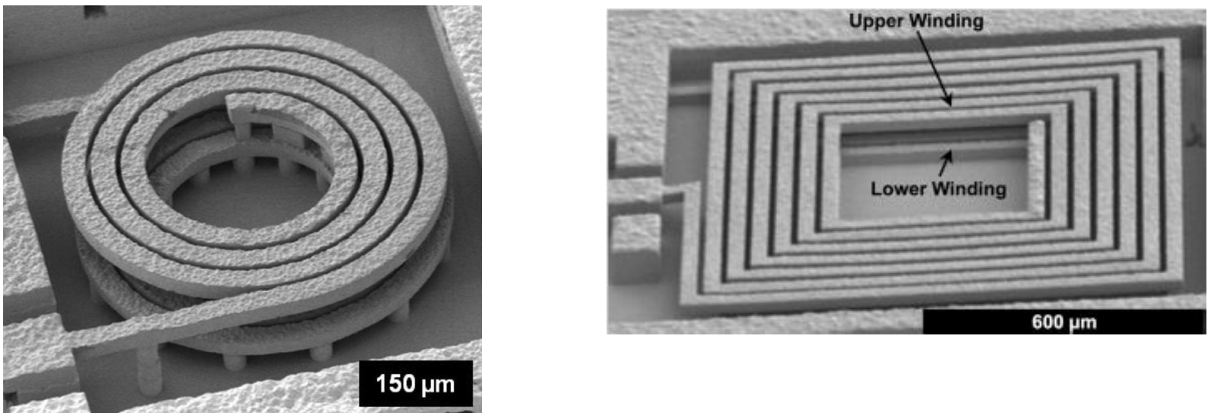

Figure 1-8 : Air-core micro-inductor realized in four and three layers of electroplated copper, USA army laboratory, in 2012 and 2014[13, 14]

An alternative approach for developing micro inductors with low profile and increased packaging densities, is to embed the inductors into the substrate i.e. the printed circuit board or the silicon. In 2013, Fang proposed a MnZn ferrite-composite-based toroidal inductor embedded in silicon [15], see Figure 1-9 . Due to the low permeability of the MnZn composite core the inductance of the inductor was limited to 43.6 nH within the inductor footprint of 2.9 mm^2. The DC resistance of the inductor was 280 mΩ. With the saturation current of 10 A, this inductor is suitable for high current application. More details of the inductor can be found in Table A1-5b.

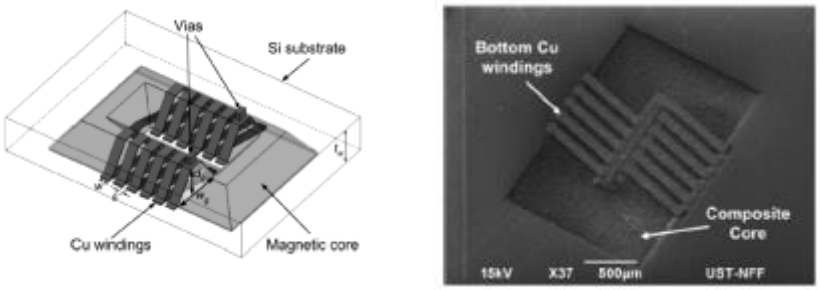

Figure 1-9: Silicon-embedded toroidal inductor with magnetic composite core and electroplated winding, Hong Kong University of science and technology, in 2013[15]

Sullivan and Sanders compared two micro-inductor structures, solenoid/toroidal and racetrack, in terms of distribution of external magnetic fields [16]. The racetrack inductor was shown to be the better design because the core encloses and shields the windings, resulting in low external fields, i.e. low losses and low electromagnetic interference. Robert Hahn et al. from Fraunhofer, in 2006, gave the comparison of planar toroidal and spiral coil ferrite inductor designs [17]. The magnetic flux distribution in toroidal coils is shown to be more homogeneous compared to planar spiral coils. Q-factor of toroidal coils is much higher than that of spirals at 1 MHz.

From previous discussion, it is clear that the choice of structure is critical in the design of a power micro-inductor in order to achieve a high inductance enhancement, minimize resistive losses at high frequency, and carry a current as high as possible without saturating the magnetic core. For comparison, the graph of L/R_{DC} ratio versus maximal operational frequency is given in Figure 1-10, this comparison misses the size and maximum current of the micro-inductor. The spiral inductors seem to have better performances at higher frequencies around 100 MHz while the toroidal inductors are better at the medium range about 10 MHz. Micro-inductors developed in research still have lower L/R_{DC} ratio than commercial discrete inductors. Thus, this graph shows the difficulty in integrating efficiently inductors onto a chip with microfabrication technologies.

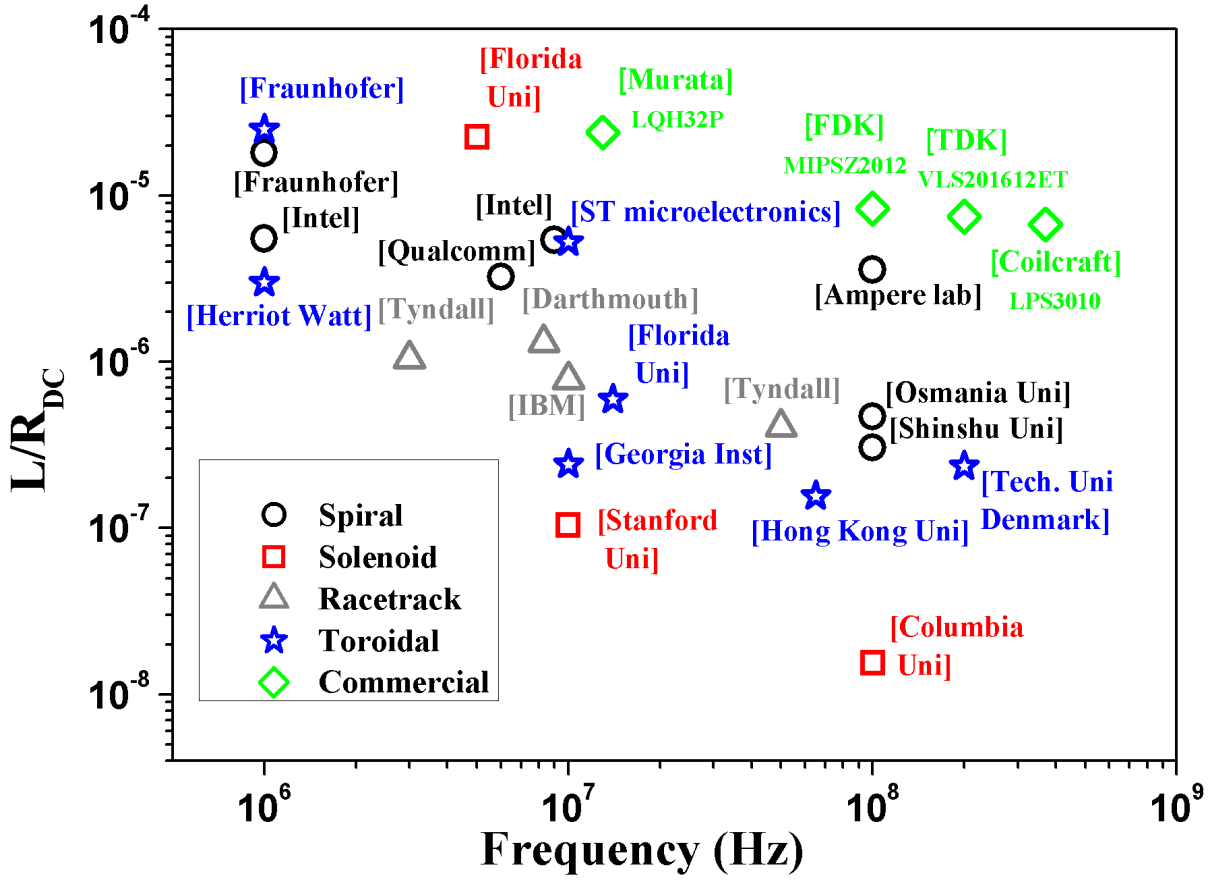

Figure 1-10 : The figure of merit L/R_{DC} versus maximal operational frequency

The previous discussion has reviewed and compared micro-inductors in terms of structures. However, the magnetic core material also plays a very important role in determining the performance of a thin-film micro-inductor. In the following section, magnetic materials and their processing technology, for usage in integrated micromagnetics, are discussed.

2.2. Materials and processing technology for magnetic cores

With further demands of miniaturization in power converters, magnetic core materials for power inductors must have low energy losses at high functional frequency and at the excitation of functional mode. The magnetic core material is expected to exhibit high resistivity and small coercive field to avoid the eddy current and hysteresis losses respectively. For applications with high current, the magnetic materials have to stand a high magnetic flux without saturation i.e. having a stable inductance with current and frequency. Table 1-1 lists the magnetic materials used for integrated inductors in the literature including ferromagnetic metal alloys, ferromagnetic metal oxides, nanogranular magnetics (nanoparticles of magnetic metal in ceramic matrix e.g. CoZrO), ferrites and ferrite composites. Amorphous metal alloys are also used for inductors although they are not listed in the table. The ferromagnetic metal alloys have advantages of high saturation induction, high permeability, low coercivity, but they have low resistivity (< 200 μΩ.cm). The ferromagnetic metal oxides have higher resistivity (several hundred μΩ.cm) with moderate permeability. Ferrites and ferrite composites have very high resistivity (> 10^6 μΩ.cm). Ferrite composites have limited permeability while ferrites have moderate to high permeability. Besides commercial materials, there are many researched and developed magnetic materials for high-frequency integration applications including granular films (CoZrO), thin-film alloys (CoNiFe), amorphous FeCo alloys, polymer-bonded materials and low temperature co-fired ceramic (LTCC) ferrites. These emerging materials can obtain stable permeabilities at higher frequencies than conventional materials. Based on the literature review, we reported in Figure 1-11 and Figure 1-12 respectively the permeability versus maximal frequency i.e. ferromagnetic resonance frequency and losses versus frequency for different magnetic materials.

Table 1-1 : Magnetic materials for integrated inductor's core in literature

	B_{sat} (T)	H_c (Oe)	μ_i	ρ ($\mu\Omega$cm)	F_{res}* (GHz)	Thickness (μm)	Ref
Ferromagnetic metal alloys							
$Ni_{80}Fe_{20}$ (Electroplating)	0.8	0.4	2200	20	<0.001	10-20	D Flynn 2009 [9], J Park 1998 [18]
$Ni_{45}Fe_{55}$ (Electroplating)	1.5	0.5	280-1000	45	>0.1	3.5-10	T O'Donnell 2010 [19], Wang 2007 [20], R Meere 2009 [21]
CoNiFe (Electroplating)	2.2	10	250	30	-	-	T. El Mastouli 2008 (LAAS) [22]
CoFeCu (Electroplating)	1.4	1	300	18	-	10	D Flynn 2009 [9]
Sandwich NiFe/(FeCo)N/NiFe	2.4	0.6	1000-	50	1.2	5nm/100nm/ 5nm	S X Wang 2000 [23]
CoZrTa (Sputtering)	1.44	0.4	600	100	0.5	2.2	D W Lee 2008 [10]
CoZrTa (Sputtering)	1.52	0.015	850-1100	100	1.4	4	D S Gardner 2009 [24]
$Ni_{80}Fe_{20}$ (Sputtering)	1.3		2000	20	0.64	4	D S Gardner 2009 [24]
FeBN (Sputtering)	1.95	30	4600	100	-	3	K H Kim 2002 [25]
CoHfTaPd (Sputtering)	1	0.5	-	170	-	9	Katayama 2000 [26]
FeCo based amorphous FCA (Electroplating)	1.5	1	300-700	120	-	-	L Trifon 2012, Enpirion [27]
Ferromagnetic metal oxides							
CoZrO (nanogranular) (Sputtering)	0.9	3	80	2000	3	20	S. Ohnuma 2001 [28], Daniel Harburg 2013 [8]
Sandwich CoZrO/ZrO_2 (Sputtering)	1	1	100	300	-	19nm/4nm multilayer 10	D Yao 2011, Darthmouth [29]
FeAlO (nanogranular) (Sputtering)	1.6	1	100	300	-	1	Y. Shimada 2003, Japan [30]
CoFeB-SiO_2 (hetero-amorpohous) (Sputtering)	0.8	5.6	50	104	3	0.5	M. Munakata 2002, Japan [31]
Ferrite							
$NiZnCuFe_2O_3$ (Screen printing)	0.46	4.1	120	10^8	-	40-100	Y. Fukuda 2003 [32]
$NiZnCuFe_2O_3$ (Sputtering)	0.22	42.8	28	-	>0.01	1-2.5	Seok Bae 2009 [33], Jaejin Lee 2011 [34]
$NiZnCuFe_2O_3$ (bulk)	-	-	272	-	0.022	-	Lucas 2012 [35]
ESL 40011® $NiZnCuFe_2O_3$ (LTCC tape)	0.33	1.7	192	-	0.01	-	Zhang 2013 [36]
Ferrite composite							
$MnZnFe_2O_3$ (Screen printing)	0.43	6-18	12-16	10^6	>0.01	200-1000	Lu 2008 [11], Park 1998 [18], Brandon 2003 [37],Kowase 2005[38]
$MnZnFe_2O_3$(Screen printing)	0.26	42	5	-	-	300	Fang 2013 [15]
$NiZnCuFe_2O_3$ (Screen printing)	0.23-0.25	17.6	25	10^8		100	Y. Fukuda 2003 [32], J Park 1997 [39], J Park 1998 [18]
$NiZnFe_2O_3$ (Screen printing)	0.2	15	6	-	>0.01	200	Wang 2011 [40]
$NiZnFe_2O_3$ (Screen printing)	0.27	20.7	7.2	-	>0.01	200	Bang 2009 [41]

*F_{res} = Self resonance frequency

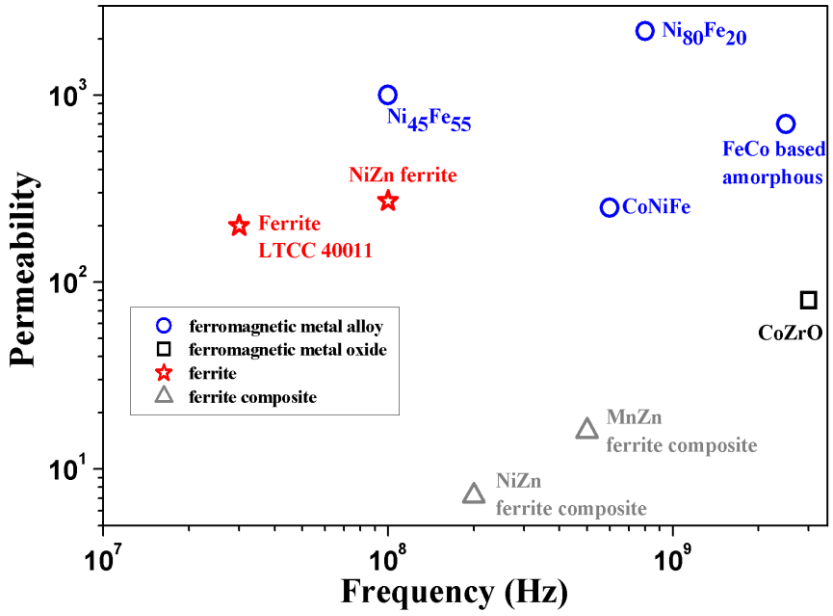

Figure 1-11 : Permeability versus maximal frequency for different magnetic materials

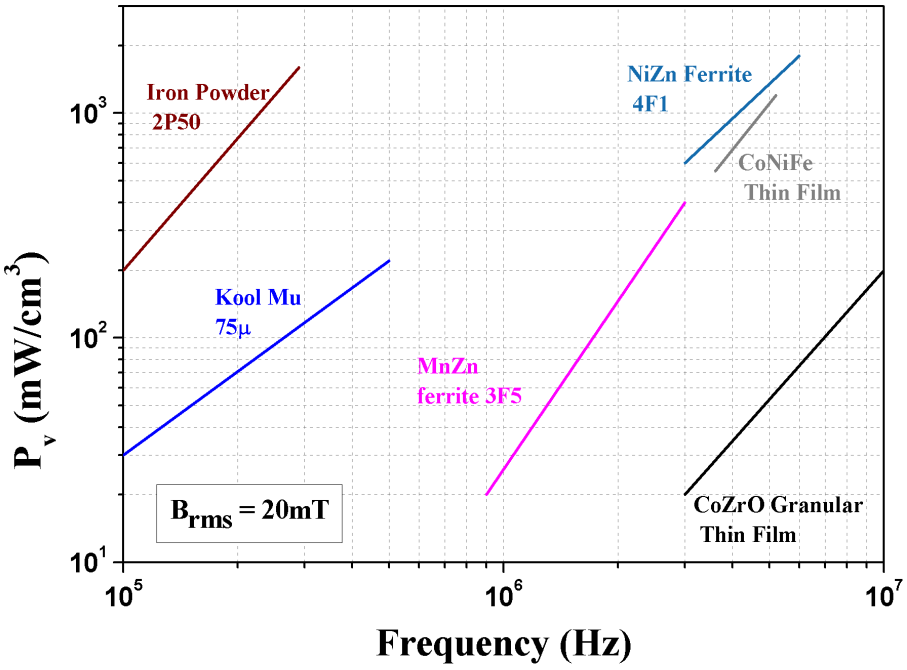

Figure 1-12 : Losses versus frequency for different magnetic materials [42]

Beside magnetic materials, it is also important to develop processing techniques that are cost-effective and compatible with high volume micro-fabrication for the incorporation of the magnetic materials in the micro-magnetic devices. Various approaches to deposit the magnetic core layer have been investigated and demonstrated over the last 20 years [6]. The most commonly used techniques are sputtering, electro-deposition and screen printing. The advantages and disadvantages of each deposition methods with corresponding magnetic materials will be discussed in this section.

Table 1-2 : Deposition technology and typical thickness

Deposition technology	Typical thickness
Screen printing	Hundreds µm
Sputter deposition	Hundreds nm to few µm
Electro deposition	Tens of µm

Sputter deposition is a popular approach for deposition of magnetic thin film cores. This technique has the advantage of depositing a wide range of magnetic materials, including ferromagnetic metal alloys and oxides. Sputtering has been investigated since 1990s for different types of magnetic materials for micro-inductors including CoZrNb[43], FeCoBC[44], FeHfO and CoFeHfO[45], FeZrO[46], FeCoBN and FeBN [25]. Since 2000, sputtering has been widely employed for depositing magnetic alloys with higher resistivity including CoHfTaPd thin film [26] and multilayer $CoZrTa/SiO_2$ [10]. The sputtered ferromagnetic materials have advantages of high saturation flux density, high resistivity and permeability. An anisotropy magnetization can be induced in magnetic materials during their deposition by application of an external magnetic field. Sputter deposition is compatible with low-temperature CMOS processing technology. Sullivan and his group in Dartmouth College have focused on developing granular nanocrystalline films as core materials for micro-inductors using sputter deposition. They investigated and reported the use of a variety of different core materials including $Co\text{-}MgF_2$ [47] and CoZrO [48]. Recently, in 2011, they reported laminated CoZrO thin films with ZrO_2 insulation in order to reduce the eddy current losses [29]. In recent work from Intel, Morrow et al. used sputtering to deposit laminated cores of permalloy in the demonstration of a fully integrated DC–DC converter with the micro-inductor fabricated on top of the power management IC [49]. Sputtering is an advanced technique with a uniform and well-controlled deposition process. This technique is suitable for depositing thin films up to a thickness of a few hundred nanometers to few micrometers. When the film is thicker than several micro-meters, stress can develop in the layer and etching of thick metallic films is an issue. Dry etching of thick films usually involves long etching times resulting in heating of the substrate and degradation of the magnetic film properties while wet etching of thick films results in severe undercutting. For thick films, sputtering is an expensive and slow process. Alternatively, sputtered films have been deposited through shadow masks up to tens of microns (20 µm); however, the problem of delamination and cracking still happened for the second layer of deposition due to an unfortunate issue of over-heating within the chamber [8].

Electroplating is a less costly method than sputter deposition techniques and more suitable for micro-inductor cores with large cross-sectional areas. The process is relatively inexpensive and compatible with standard microfabrication. The films deposited by electroplating have thickness of several micro-meters to several tens of micro-meter including alloys of NiFe with different composition such as

$Ni_{80}Fe_{20}$, $Ni_{45}Fe_{55}$, $Ni_{50}Fe_{50}$ [9, 20, 50] and others like CoPFe [51], CoNiFe [22], CoFeCu [9], NiFeMo [18, 52]. At LAAS, thin film ferromagnetic NiFe and CoFeNi metal alloys were developed with electrolytic deposition [22]. $Ni_{80}Fe_{20}$ is largely investigated as electrodeposited magnetic material due to its well-developed technologies in the recording-head industry. In fact, NiFe alloys have relatively low resistivity and they are not the ideal materials for inductors operating at high frequencies. With electroplating technique, only conductive materials can be electroplated; so, at high frequency operation eddy currents can be considerable and should be controlled by lamination. Recently, laminated thick films of electroplated metallic alloys were demonstrated for CoNiFe with about 40 layers, 1 μm thick for each layer separated by copper layers and SU-8 support [53]. The test inductor demonstrated a constant inductance of 1.6 μH up to 10 MHz, indicating suppressed eddy current losses. But one can argue that this rather complicated process with large number of steps (40 layers), could be difficult and costly to transfer to the industry for large scale manufacturing.

Screen printing is typically suitable for deposition of thin films with thickness in the range of several micrometers to hundreds of micrometer. The magnetic materials are typically suspended in a polymer matrix for deposition. NiZn and MnZn are the most popular soft ferrites which were deposited as magnetic cores for micro-fabricated inductors using screen printing since 1998 [18, 32, 38, 54]. This technique presents a good compromise between deposition of magnetic material with high resistivity ($>10^3$ Ω·m), low core losses and the simplicity of processing the polymer. Although screen printing offers a comparatively simple process, the requirement of a high-temperature sintering for realizing the magnetic phase in ferrite materials makes this process incompatible with standard silicon-based MEMS fabrication technology.

Considering the proposed magnetic materials in the literature, we see that although ferromagnetic metal alloys have big advantages of high saturation induction and low coercivity, they mostly show limited resistivity (< 200 μΩ·cm) which can result in high eddy current losses. In fact, they can be laminated to reduce eddy current but lamination is complicated and costly for very thick layers. Ferromagnetic metal oxides including nanogranular materials have higher resistivity but their fabrication technology is expensive for the core thickness higher than several micrometers.

On the other hand, ferrites and ferrite composites have high resistivity (> 10^6-10^8 μΩ·cm) and good compromise between permeability and losses. Their saturation induction is rather low (0.25-0.3T). Ferrites need to be sintered at high temperature (about 900° C) to realize the magnetic phase in order to get these optimum magnetic properties. In commercial products, thin film polymer-bonded ferrite is available as ceramic tape for LTCC technology in which ferrite powder is distributed in a polymer matrix. This thin ferrite tapes can be stacked together and sintered in a furnace to create a ferrite-

crystallized structure. They can be milled for building different designs of integrated magnetic components.

For on-chip integration, thin film ferrites can be deposited by different techniques including sputter deposition and screen printing. In Bae and Jaejin's work, thin film layers of NiZnCu ferrite were deposited by sputtering layer by layer of NiO, Fe_2O_3, ZnO and CuO metal oxides [33, 34]. The deposited multilayer oxide films were crystallized to give 1 or 2.5µm thick ferrite by post annealing at 800°C for 1 hour or 4 hours. This sputtered ferrites' thickness is most probably not sufficient to reach high inductance density and avoid saturation.

Alternatively, thin film layer of ferrite composite can be deposited by screen printing with thickness up to several hundred micrometers. This simple and low-cost technique has been investigated in many researches recently [15, 18, 32, 37, 38, 40, 41]. The ferrite powder is distributed in a polymer matrix and screen printed in a mold to form different shaped magnetic cores. However, ferrite composite is usually non-sintered, resulting in low performance of the inductor in terms of inductance. As mentioned, sintering means high temperatures (about 900°C) and regarding CMOS compatibility, such high temperatures can be a problem for most materials already present on the substrate but there are some ways to tackle this issue. For integrated ferrite-based micro-inductors, some authors have done sintering of the bottom and top ferrite layer in-situ [33]. Others have developed hybrid solutions where the core is fabricated off-chip [55].

3. Objectives for PhD thesis

An important criteria for the design and fabrication development of micro-inductors with high performance is to have a clear idea about the system integration, i.e. how/where the inductor is to be placed on a IPD (Integrated Passive Die) containing other passive components and in the total power system (with active components and drivers). The context of this PhD thesis is the project PRIIM[1], with IPDiA company as a leader, in which integrated passive components for DC-DC converters are to be developed Target specifications for integrated inductors are defined according to requests from clients using low-power DC-DC converters and are typically the followings: **an inductance in the range of 200-2000 nH at bias current of 0.6 A, an equivalent series resistance in the range of 0.1Ω - 0.2 Ω and operating at medium frequency 5-10 MHz**. Eventually, the footprint has to remain around 3 mm^2 (below commercial product size). The thickness of the micro-inductor should be less than 250 µm to constitute a competitive solution in comparison to current commercial inductors, for

1. [1] **PRIIM "Projet de Réalisation et d'Innovation Industrielle dédié aux Microsystèmes hétérogènes"** (10/2009 – 10/2013) – funded by OSEO

example LPS3010 inductor by Coilcraft [56]. To be competitive with commercial power converters, total profile of the system should be lower than 1 mm. Interposers carrying passive components are a good solution to reduce the profile of the system [57]: this solution is exploited by IPDiAs under the name PICS for Passive Integration Connecting Substrate, illustrated in Figure 1-13. In this solution, micro-inductors (for power converter solutions) could be placed on top of other passive components, such as 3D capacitors.

Within this project, beside the target specifications defined above, the additional constraints are:

- The technology of the power inductor has to be developed for enabling a future transfer into IPDiA's production line, which means compatibility with PICS substrates: no electromagnetic interference (EMI) if 3D capacitors are placed below the inductor, the use of existing interconnection technologies for metal windings, a maximum thickness for the component to fit in the package. With interposer technology, two dies with copper tracks may be stacked on top of each other and the inductor core will be put in between. The copper pillar with metal bump in the die is around 70 µm and the inductor core should not thicker than two copper pillars, i.e. 140 µm.
- Low cost fabrication process, which in general is achieved thanks to simplicity (minimum number of processing steps).

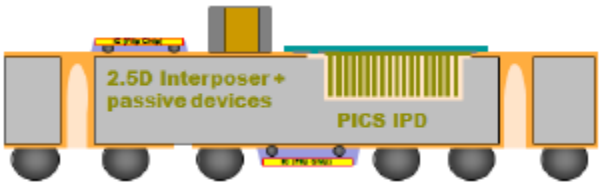

Figure 1-13 : Schematic of IPDiA 2.5D interposer with PICS Integrated passive devices (IPD) and external active dies in flip-chip or chip-on-silicon technologies[58]

**** Choice of material and technology**

Considering the constraints of limited thickness, minimum losses and high inductance, fully sintered ferrite from ferrite tapes and ferrite composites appear as a promising solution. Both of them can achieve high thickness up to hundreds of micrometer with fast and low cost manufacturing. Since they are sintered in a furnace to obtain crystallized ferrite structure, they offer pre-eminent permeability stable up to more than 10 MHz. Their losses are acceptable according to literature [42]. They are flexible for building the integrated inductor in terms of deposited thickness and different shaped design. The monolithic and hybrid solution may be developed for the integration. In our project, toroidal structure is chosen for inductor design in order to obtain high inductance density. Moreover, it

is easier to form the inductor by wrapping the windings around one layer of magnetic material rather than wrapping magnetic layers around the windings.

The motivation of this thesis is to study the soft ferrite materials and processing technologies to integrate the fully sintered ferrite core into the toroidal micro-inductor in a small footprint for working at frequency 5-10 MHz, with small AC/DC resistance and high inductance density according the target specifications. Design optimization is to be done to obtain the best performance for the integrated inductor.

The objectives of my thesis are:

- To develop a technology to fabricate fully sintered toroidal ferrite cores in small size, ideally below 3mm^2 with adequate thickness and integrate in electroplated copper winding to form micro-inductors with low-profile < 250 µm.
- To characterize, compare and choose the most suitable ferrite for the best performance of cores in terms of permeability and losses in the range 5-10 MHz.
- To find out the toroidal inductor design which will allow obtaining the targeted specifications or the best performance of inductor in terms of inductance density and losses in the range 5-10 MHz.

In Chapter 2, we will describe the material synthesis and technology development to produce ferrite rectangular cores for micro-inductors. Then, Chapter 3 will detail the results of ferrite cores characterization including microstructure, composition, permeability and losses. Once the main properties of the ferrite cores are identified, we will focus, in Chapter 4, on the design optimization for micro-inductors. The experimental approaches and development of processing technology to realize the final micro-inductor are presented in Chapter 5. Finally, some conclusions on the work are given, and perspectives are proposed for future work.

References

1. N. Mohan, T. M. Undeland, and W. P. Robbins, *Power Electronics: Converters, Applications and Design, 3rd Edition*, 2003 Wiley.
2. M. Kazimierczuk, *High-frequency Magnetic Components*, 2009, Chichester, U.K. J. Wiley, 486 pages.
3. N. Wang, T. O'donnell, and C. O'mathuna, "An Improved Calculation of Copper Losses in Integrated Power Inductors on Silicon", *IEEE Transactions on Power Electronics*, 28 (8), 3641-3647, 2013
4. J. Barranger, *Hysteresis and eddy-current losses of a transformer lamination viewed as an application of the poynting theorem*, 1965, Ohio Lewis Research Center.
5. C. R. Sullivan, "Overview of core loss prediction for non-sinusoidal waveforms", *Dartmouth Magnetic Components and Power Electronics Research Group*, 2012.

6. C. O. Mathuna, N. Wang, S. Kulkarni, and S. Roy, "Review of Integrated Magnetics for Power Supply on Chip (PwrSoC)", *IEEE Transactions on Power Electronics*, 27 (11), 2012
7. Y. Sugawa, K. Ishidate, M. Sonehara, and T. Sato, "Carbonyl-Iron/Epoxy Composite Magnetic Core for Planar Power Inductor Used in Package-Level Power Grid", *IEEE Transactions on Magnetics*, 49 (7), 4172-4175, 2013
8. D. V. Harburg, G. R. Khan, F. Herrault, J. Kim, C. G. Levey, and C. R. Sullivan, "On-chip RF power inductors with nanogranular magnetic cores using prism-assisted UV-LED lithography", *17th Transducers & Eurosensors Conference*, 701 - 704, 2013.
9. D. Flynn and M. P. Y. Desmulliez, "Design, Fabrication, and Characterization of Flip-Chip Bonded Microinductors", *IEEE Transactions on Magnetics*, 45 (8), 3055-3063, 2009
10. D. W. Lee, K.-P. Hwang, and S. X. Wang, "Fabrication and Analysis of High-Performance Integrated Solenoid Inductor With Magnetic Core", *IEEE Transactions on Magnetics*, 44 (11), 2008
11. J. Lu, H. Jia, A. Arias, X. Gong, Z. J. Shen, "On-chip bondwire transformers for power SOC applications", in *Applied Power Electronics Conference and Exposition (APEC)*, Austin, TX, 2008, 199-204
12. H. Jia, J. Lu, X. Wang, K. Padmanabhan, and Z. J. Shen, "Integration of a Monolithic Buck Converter Power IC and Bondwire Inductors With Ferrite Epoxy Glob Cores", *IEEE Transactions on Power Electronics*, 26 (6), 1627-1630, 2011
13. C. D. Meyer, S. S. Bedair, B. C. Morgan, and D. P. Arnold, "Influence of Layer Thickness on the Performance of Stacked Thick-Film Copper Air-Core Power Inductors", *IEEE Transactions on Magnetics*, 48 (11), 4436-4439, 2012
14. C. D. Meyer, S. S. Bedair, B. C. Morgan, and D. P. Arnold, "A Micromachined Wiring Board With Integrated Microinductor for Chip-Scale Power Conversion", *IEEE Transactions on Power Electronics*, 29 (11), 6052-6063, 2014
15. X. Fang, R. Wu, L. Peng, and J. K. O. Sin, "A Novel Silicon-Embedded Toroidal Power Inductor With Magnetic Core", *IEEE Electron Device Letters*, 34 (2), 292-294, 2013
16. C. R. Sullivan and S. R. Sanders, "Design of microfabricated transformers and inductors for high-frequency power conversion", *IEEE Transactions on Power Electronics*, 11 (2), 228-238, 1996
17. R. Hahn, S. Krumbholz, H. Reichl, *Low profile power inductors based on ferromagnetic LTCC technology*, in *56th Electronic Components & Technology Conference 2006, Vol 1 and 2, Proceedings*. 2006. p. 528-533.
18. J. Y. Park and M. G. Allen, "Development of magnetic materials and processing techniques applicable to integrated micromagnetic devices", *Journal of Micromechanics and Microengineering*, 8 (4), 1998
19. T. O'donnell, N. Wang, S. Kulkarni, R. Meere, F. M. F. Rhen, S. Roy, and S. C. O'mathuna, "Electrodeposited anisotropic NiFe 45/55 thin films for high-frequency micro-inductor applications", *Journal of Magnetism and Magnetic Materials*, 322 (9-12), 2010
20. N. Wang, T. O'donnell, S. Roy, P. Mccloskey, and C. O'mathuna, "Micro-inductors integrated on silicon for power supply on chip", *Journal of Magnetism and Magnetic Materials*, 316 (2), E233-E237, 2007
21. R. Meere, T. O'donnell, N. Wang, N. Achotte, S. Kulkarni, and S. C. O'mathuna, "Size and Performance Tradeoffs in Micro-Inductors for High Frequency DC-DC Conversion", *IEEE Transactions on Magnetics*, 45 (10), 4234 - 4237, 2009
22. T. El Mastouli, J. P. Laur, J. L. Sanchez, M. Brunet, D. Bourrier, and M. Dilhan, "Micro-iuductors integrated on silicon for dc-dc converters", *SPIE-INT SOC Optical engineering, Bellingham,WA 98227-0010 USA*, A8820-A8820, 2008.
23. S. X. Wang, N. X. Sun, M. Yamaguchi, and S. Yabukami, "Sandwich films - Properties of a new soft magnetic material", *Nature*, 407 (6801), 150-151, 2000

24. D. S. Gardner, G. Schrom, F. Paillet, B. Jamieson, T. Karnik, and S. Borkar, "Review of On-Chip Inductor Structures With Magnetic Films", *IEEE Transactions on Magnetics*, 45 (10), 4760-4766, 2009
25. K. H. Kim, J. Kim, H. J. Kim, and S. H. Han, "A megahertz switching dc/dc converter using FeBN thin film inductor", *IEEE Transactions on Magnetics*, 38 (5), 2002
26. Y. Katayama, S. Sugahara, H. Nakazawa, M. Edo, "High-power-density MHz-switching monolithic DC-DC converter with thin-film inductor", in *Power Electronics Specialists Conference (PESC 2000)*, Natl Univ Ireland, Galway, Ireland, 2000, 1485-1490
27. T. Liakopoulos, A. Panda, M. Wilkowski, A. Lotfi, K. H. Tan, L. Zhang, C. Lai, and D. Chen, "Introducing FCA, a New Alloy for Power Systems on a Chip and Wafer Level Magnetic Applications", *2012 13th International Conference on Electronic Packaging Technology & High Density Packaging (ICEPT-HDP 2012)*, 948-953, 2012
28. S. Ohnuma, H. J. Lee, N. Kobayashi, H. Fujimori, and T. Masumoto, "Co-Zr-O nano-granular thin films with improved high frequency soft magnetic properties", *IEEE Transactions on Magnetics*, 37 (4), 2251-2254, 2001
29. D. Yao, C. G. Levey, C. R. Sullivan, "Microfabricated V-Groove Power Inductors Using Multilayer Co-Zr-O Thin Films for Very-High- Frequency DC-DC Converters", *2011 IEEE Energy Conversion Congress and Exposition (ECCE)*, 2011
30. Y. Shimada, M. Yamaguchi, S. Ohnuma, T. Itoh, W. D. Li, S. Ikeda, K. H. Kim, and H. Nagura, "Granular thin films with high RF permeability", *IEEE Transactions on Magnetics*, 39 (5), 3052-3056, 2003
31. M. Munakata, M. Motoyama, M. Yagi, T. Ito, Y. Shimada, M. Yamaguchi, and K. I. Arai, "Very high electrical resistivity and heteroamorphous structure of soft magnetic (Co35.6Fe50B14.4)-(SiO2) thin films", *IEEE Transactions on Magnetics*, 38 (5), 3147-3149, 2002
32. Y. Fukuda, T. Inoue, T. Mizoguchi, S. Yatabe, and Y. Tachi, "Planar inductor with ferrite layers for DC-DC converter", *IEEE Transactions on Magnetics*, 39 (4), 2003
33. S. Bae, Y.-K. Hong, J.-J. Lee, J. Jalli, G. S. Abo, A. Lyle, B. C. Choi, and G. W. Donohoe, "High Q Ni-Zn-Cu Ferrite Inductor for On-Chip Power Module", *IEEE Transactions on Magnetics*, 45 (10), 4773-4776, 2009
34. J. Lee, Y.-K. Hong, S. Bae, J. Jalli, J. Park, G. S. Abo, G. W. Donohoe, and B.-C. Choi, "Integrated Ferrite Film Inductor for Power System-on-Chip (PowerSoC) Smart Phone Applications", *IEEE Transactions on Magnetics*, 47 (2), 2011
35. A. Lucas, "Etude et mise au point de transformateurs large bande radiofréquence", *L'Ecole normale superieure de Cachan*, PhD thesis, 234, 2012.
36. W. Zhang, M. Mu, D. Hou, Y. Su, Q. Li, and F. C. Lee, "Characterization of Low Temperature Sintered Ferrite Laminates for High Frequency Point-of-Load (POL) Converters", *IEEE Transactions on Magnetics*, 49 (11), 5454-5463, 2013
37. E. J. Brandon, E. Wesseling, V. White, C. Ramsey, L. Del Castillo, and U. Lieneweg, "Fabrication and characterization of microinductors for distributed power converters", *IEEE Transactions on Magnetics*, 39 (4), 2049-2056, 2003
38. I. Kowase, T. Sato, K. Yamasawa, and Y. Miura, "A planar inductor using Mn-Zn ferrite/polyimide composite thick film for low-voltage and large-current DC-DC converter", *IEEE Transactions on Magnetics*, 41 (10), 2005
39. J. Y. Park, L. K. Lagorce, and M. G. Allen, "Ferrite-based integrated planar inductors and transformers fabricated at low temperature", *IEEE Transactions on Magnetics*, 33 (5), 3322-3324, 1997
40. M. L. Wang, J. P. Li, K. D. T. Ngo, and H. K. Xie, "A Surface-Mountable Microfabricated Power Inductor in Silicon for Ultracompact Power Supplies", *IEEE Transactions on Power Electronics*, 26 (5), 1310-1315, 2011

41. D. H. Bang and J. Y. Park, "Ni-Zn Ferrite Screen Printed Power Inductors for Compact DC-DC Power Converter Applications", *IEEE Transactions on Magnetics*, 45 (6), 2762-2765, 2009
42. F. C. Lee and Q. Li, "High-Frequency Integrated Point-of-Load Converters: Overview", *IEEE Transactions on Power Electronics*, 28 (9), 4127-4136, 2013
43. T. Sato, H. Tomita, A. Sawabe, T. Inoue, T. Mizoguchi, and M. Sahashi, "A magnetic thin film inductor and its application to a MHz switching DC-DC converter", *IEEE Transactions on Magnetics*, 30 (2), 1994
44. H. Tomita, T. Inoue, and T. Mizoguchi, "Hetero-amorphous Fe-Co-B-C soft magnetic thin films with uniaxial magnetic anisotropy and large magnetostriction", *IEEE Transactions on Magnetics*, 32 (5), 1996
45. T. Sato, E. Komai, K. Yamasawa, T. Hatanai, and A. Makino, "Application of nanocrystalline Fe (or Co-Fe)-Hf-O magnetic films with high electrical resistivity to micro DC-DC converters", *IEEE Transactions on Magnetics*, 33 (5), 1997
46. Y. Sasaki, E. Komai, and T. Hatanai, "Thin film inductor for microswitchingconverters using a high resistive Fe-Zr-O film", *International Power Electronics Conference 2000 Proceedings IEEJ*, 315–319, 2000.
47. K. D. Coonley, G. J. Mehas, C. R. Sullivan, and U. J. Gibson, "Evaporatively deposited Co-MgF2 granular materials for thin-film inductors", *IEEE Transactions on Magnetics*, 36 (5), 2000
48. S. Lu, Y. Sun, M. Goldbeck, D. R. Zimmanck, C. R. Sullivan, "30-MHz power inductor using nano-granular magnetic material", in *38th IEEE Power Electronic Specialists Conference*, Orlando, FL, 2007
49. P. R. Morrow, C.-M. Park, H. W. Koertzen, and J. T. Dibene, II, "Design and Fabrication of On-Chip Coupled Inductors Integrated With Magnetic Material for Voltage Regulators", *IEEE Transactions on Magnetics*, 47 (6), 2011
50. N. Wang, E. J. O'sullivan, P. Herget, B. Rajendran, L. E. Krupp, L. T. Romankiw, B. C. Webb, R. Fontana, E. A. Duch, E. A. Joseph, S. L. Brown, X. Hu, G. M. Decad, N. Sturcken, K. L. Shepard, and W. J. Gallagher, "Integrated on-chip inductors with electroplated magnetic yokes (invited)", *Journal of Applied Physics*, 111 (7), 2012
51. R. W. Filas, T. M. Liakopoulos, and A. Lotfi, "Micromagnetic device having alloy of cobalt, phosphorous and iron", Sep. 2003.
52. J. Y. Park, S. H. Han, and M. G. Allen, "Batch-fabricated microinductors with electroplated magnetically anisotropic and laminated alloy cores", *IEEE Transactions on Magnetics*, 35 (5), 4291-4300, 1999
53. J. Kim, M. Kim, F. Herrault, J. Park, and M. G. Allen, "Highly Laminated Soft Magnetic Electroplated CoNiFe Thick Films", *IEEE Magnetics Letters*, 4 2013
54. Y. Mano, S. Bae, J. Moon, H. Jung, Y. Oh, "Planar inductor with ferrite layers for DC-DC converter", *Transducers '05, Digest of Technical Papers, Vols 1 and 2*, 2005
55. X. Yu, J. Kim, F. Herrault, and M. G. Allen, "Silicon-embedded toroidal inductors with magnetic cores: Design methodology and experimental validation", *Applied Power Electronics Conference and Exposition 29th (APEC)*, 763 - 767, 2014.
56. L. Inductor, "Coilcraft (http://www.coilcraft.com/lps3010.cfm)",
57. F. Murray, "Silicon based system-in-package : a passive integration technology combined with advanced packaging and system based design tools to allow a breakthrough in miniaturization", in *BIPOLAR/BiCMOS Circuits and Technology Meeting*, Santa Barbara, CA, 2005, 169-173
58. L. O. Stéphane Bellenger, Jean-René Tenailleau, "Silicon Interposers with Integrated Passive Devices: Ultra-Miniaturized Solution using 2.5D Packaging Platform ", 2014.

Chapter 2 Development of ferrite cores for toroidal inductors

Introduction

As argued in chapter 1, we have chosen to develop a ferrite based micro-inductor with a rectangular toroidal geometry. From the literature study, soft ferrites are chosen as magnetic material for our micro-inductor core with respect to the target specification in the frequency range 5-10 MHz. We decided to study these soft ferrites coming from two sources: (i) one is the commercial thin film LTCC ferrite (ii) the second one is the in-house made ferrite powder. In this chapter, after providing the general physics of soft ferrite materials and selecting appropriate materials, the geometry of proposed inductor design will be described. Then, details of the NiZn ferrite synthesis and deposition/shaping are presented in the last part of this chapter. For the purpose of characterization, the free-standing ferrite cores were realized from the commercial thin film ferrite and from the in-house made ferrite powder. These cores will be also used to integrate into the micro-inductor according to the hybrid integration approach described in Chapter 5.

1. Ferrite materials

1.1. General introduction

In general, ferrites are polycrystalline compounds of trivalent iron oxide Fe_2O_3 with bivalent transition metals such as FeO, NiO, ZnO, MnO, CuO, BaO, CoO, and MgO. Ferrites are classified by crystal structure or by magnetic behavior. According to crystal structure criteria, ferrites consist of spinel, garnet, perovskite, orthoferrite, and magnetoplumbite ferrites [1]. Soft ferrites include only spinel ferrites what have cubic close-packed crystal structure of oxygen with metal ion Me^{2+} and Fe^{3+} in tetrahedral and octahedral coordinations. Spinel ferrites also have high resistivity that satisfies our requirement to suppress the eddy current loss. Due to all that, spinel ferrites are our choice for the core of inductor.

The spinel ferrites (for simplification, we call “ferrites” hereinafter) have the general composition as $MeFe_2O_4$ which have cubic close-packed crystallized arrangement of oxygen atoms and metal ions Me^{2+}, Fe^{3+} into two different crystallographic sites, tetrahedral and octahedral. These sites have tetrahedral and octahedral oxygen coordination termed as A and B-sites respectively, see Figure 2-1. If A-sites, tetrahedral sites, are completely occupied by Fe^{3+} cations and B-sites are randomly occupied by Me^{2+} and Fe^{3+} cations, the structure is referred to as an inverse spinel. When A-sites are occupied by Me^{2+} cations and B-sites are occupied by Fe^{3+} cations, the structure is referred as a normal spinel. The intermediate case exists in which both sites contain a fraction of Me^{2+} and Fe^{3+} cations. The magnetic moments of cations in the A and B-sites are aligned parallel with respect to one another. The

arrangement between A-sites and B-sites is anti-parallel. Because the number of octahedral position is double that of tetrahedral position, there is a positive net of magnetic moment yielding a ferrimagnetic ordering for the crystal. The choice of metal cations and the distribution of ions between A-sites and B-sites offer a tunable magnetic system.

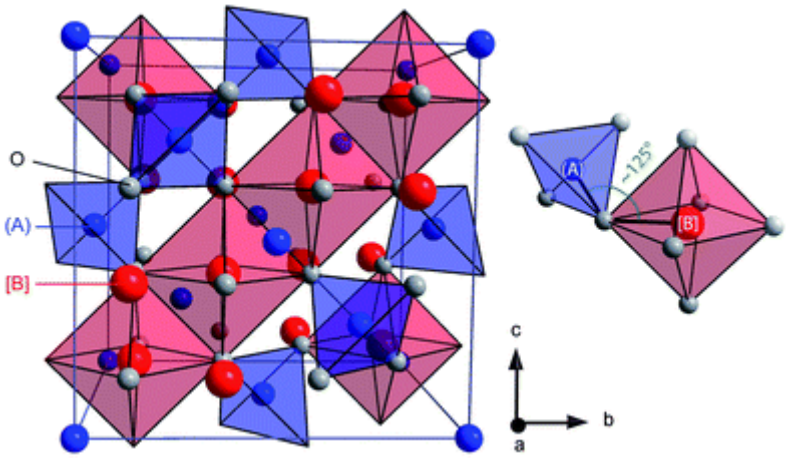

Figure 2-1 : Scheme of a unit cell and ferrimagnetic ordering of spinel ferrite structure [2]

In the spinel ferrite, the metal ions are separated by paramagnetic oxygen; they can't interact directly. The interaction among them is super exchange. The notion of "super exchange" was introduced by Kramer and Anderson [3] to explain the coupling between two sub-networks which takes place through electron of O^{2-} ions. The electronic configuration of oxygen atom is $(1s)^2 (2s)^2 (2p)^4$. Kramers proposed that an electron of 3d layer of a transition metal passes over the 2p – layer of oxygen. The same phenomenon occurs with the second metal ion to complete the 2p – layer of oxygen, resulting a coupling between two magnetic ions. Concerning the explanation of antiparallel coupling, it is supposed that the first metal M1 has a spin +1/2, it prefers interacting with the spin -1/2 of oxygen. The electron in the oxygen atom which possesses a spin +1/2 will interact with a metal ion M2 possessing a spin -1/2 for a reason of stability. So, we have an antiparallel coupling between two magnetic ions. The magnitude of this coupling is influenced by the distance and angle between ions M1-Oxygen-M2. The strongest interaction takes place at an angle of 180°. The interaction A-O-B is predominant.

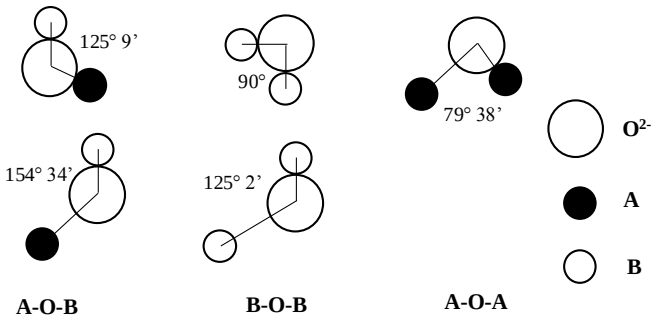

Figure 2-2 : Angle between different ion pairs in interaction [4, 5]

To minimize energy, a magnetic object is not uniformly magnetized but divided into magnetic domains called Weiss domains. In each domain, all magnetic moments are oriented in the same direction. These areas are separated by a Bloch wall within which the magnetization changes gradually to make the connection between two magnetic domains.

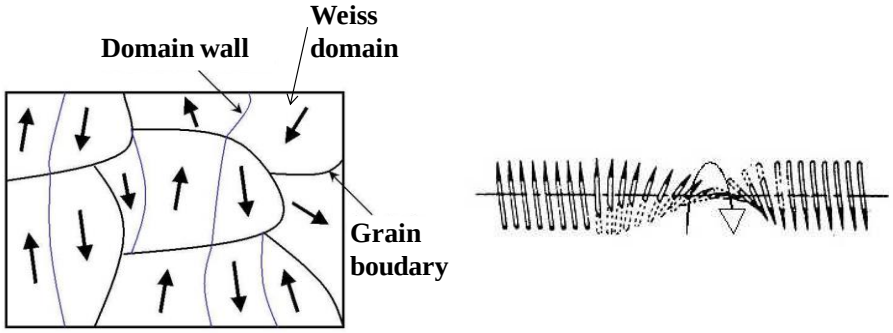

Figure 2-3 : Distribution of magnetic domain in the demagnetized state (left) and distribution of spin in Bloch/domain wall [5-7]

Basically, there are two magnetization mechanisms: (i) Magnetization mechanism by displacement of walls and (ii) magnetization mechanism by rotation of magnetic moments. The first one is also known as Globus-Guyot mechanism which was established in the year of 60s. He described a model in which static permeability of ferrite is directly proportional to grain size of ceramic/ferrite. The second one is known as Snoek mechanism. It assumes that the magnetization is established by the rotation of the magnetic moments. Literature has shown that the mechanism of the movement of walls dominates at low frequency and the magnetic rotation becomes predominant at high frequency.

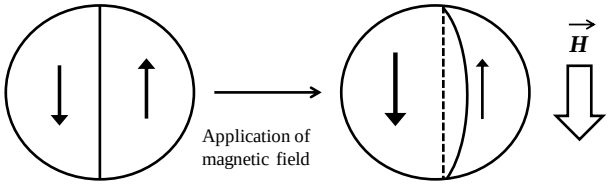

Figure 2-4 : Grains in Globus model

Regarding magnetic losses, the external magnetic field displaces the magnetic moments from its easy axis which will establish a restore force in order to return the original position. This movement can be damped due to defects present in the sample and that explains the magnetic losses. There are several types of losses: (i) Losses due to the reverse between easy and hard axis (probably at small induction) (ii) hysteresis losses, (iii) eddy current losses and supplementary losses due to the resonance/relaxation of walls and anomalous losses.

When the magnetic sample is put under an alternating magnetic field, it stores magnetic energy but does not return completely when remove this magnetic field. These energy losses can be explained by the presence of impurities in the material or defects in the crystal lattice that prevent the normal

movement of domain walls. Apart from the magnetic flux density, the magnetostriction also exhibits hysteresis versus the magnetic field, which creates hysteresis losses as well. To reduce the contribution of hysteresis losses, the most favorable condition is low magneto-crystalline anisotropy, no defects in materials i.e. no magnetic inclusions and no crystal defect, large grain size and low magnetostriction i.e. low magnetoelastic anisotropy. Concerning losses by eddy currents, the application of an alternating magnetic field will result in an induced current in the material. The circulation of these currents causes the heating in materials and that are losses, called eddy current losses. This loss depends on operational frequency and resistivity of material. The loss caused by eddy currents is generally negligible for ferrite thanks to their very high resistivity. The resonance/relaxation losses arise when the operating frequency approaches the resonance frequency of material. It is preferable to work at frequency far below the peak of $\mu_r''(f)$ to avoid these losses.

1.2. Choice of ferrite materials

The MnZn and NiZn ferrites are two representatives of spinel ferrites that have attracted a lot of research effort in last decades. The MnZn ferrites have high permeability; however, they are limited to the average frequencies. The maximum functional frequency of MnZn ferrites is around 1 to 2 MHz. Beyond these frequencies, the real permeability (μ') drops and magnetic losses (μ'') become very high, which results in increased power losses. Permeability of NiZn ferrites is moderately high and their resistivity is as high as 10^6 to 10^8 μΩ.cm. The maximal functional frequency of NiZn is medium high up to 10 MHz. Their coercivity is normally small. Therefore, NiZn ferrites were suitable and chosen for our magnetic cores. It is emphasized to look at permeability and magnetic losses for different NiZn ferrites in the family.

In 2010, Anthony Lucas studied and optimized NiZn bulk ferrites for high frequency applications with variation of Ni/Zn ratio, and the inclusion of Cu and Co [5]. We based our work on his study for choosing ferrites for our magnetic cores. According to his work, the role of Cu is to facilitate the phenomenon of diffusion which is the origin of calcining and sintering process. The presence of Cu in the NiZn ferrite helps to reduce the sintering temperature down to 800-900°C that will make NiZnCu ferrite more compatible with other micromachining processes such as LTCC technology. The introduction of Cu also helps to improve the densification during sintering. Moreover, according to his results, the addition of Co into NiZnCu ferrites proved to reduce the total loss at high frequency [5]. The introduced Co^{2+} ions block the movement of magnetic domain walls and therefore, reduce the losses associated with that movement i.e. reduce the total magnetic losses. However, the side effect of blocking the movement of domain walls is to decrease the permeability of the material and increase the cut-off frequency. We need a good compromise between permeability and cut-off functional frequency and also the total magnetic loss. With the same Co doping rate, the lower Ni/Zn ratio, the higher permeability and the lower magnetic resonance frequency.

We wanted to evaluate ferrite materials with two levels of permeabilities: 70 and 200 and with the lowest losses as possible i.e. high resistivity, low coercive field, high saturation induction and an operation frequency > 5 MHz. From Lucas' thesis report, we chose two composition of ferrites $Ni_{0.30}Zn_{0.55}Cu_{0.15}Co_{0.035}Fe_2O_4$ (named U70 with Ni/Zn = 0.54 and Co = 0.035%wt) and $(Ni_{0.24}Zn_{0.56}Cu_{0.20})_{0.965}Co_{0.035}Fe_2O_4$ (named U200 with Ni/Zn = 0.43, Co = 0.035%wt) based on these criteria. These two materials can give us a good view of the tradeoff of between inductance and functional frequency range and total magnetic losses. The Co doping rate in the Ni-Zn-Cu ferrite, which is 0.035%wt for both ferrites, has a very important role. U200 losses were reported as 200mW.cm^{-3} at 1.5 MHz under 25 mT [5].

As a back-up solution, we have looked at the commercial thin-film ferrite tape provided by ESL ElectroScience. From the literature review, we chose ESL 40010® and ESL 40011® (named 40010 and 40011 in this thesis) with the expected permeabilities of 60 and 200 respectively. These materials were characterized at macro-scale by Mu et al [8]. At 1.5 MHz and 20 mT, losses of 1000 mW.cm^{-3} and 2000 mW.cm^{-3} were measured for 40010 and 40011.

In this work, in-house made ferrites (U70 and U200) and commercial thin-film ferrites (40010 and 40011) will be characterized in thin film form. From the characterization results (reported in chapter 3), the extracted properties will be implemented in a design routine including modeling simulation (detailed in chapter 4).

2. Design of toroidal rectangular micro-inductor

The schematic design of the toroidal rectangular micro-inductor is presented in Figure 2-5 with the top view and cross section. The copper windings are constituted by the bottom copper tracks and top copper tracks connected through vias. The ferrite core is wrapped inside the copper windings.

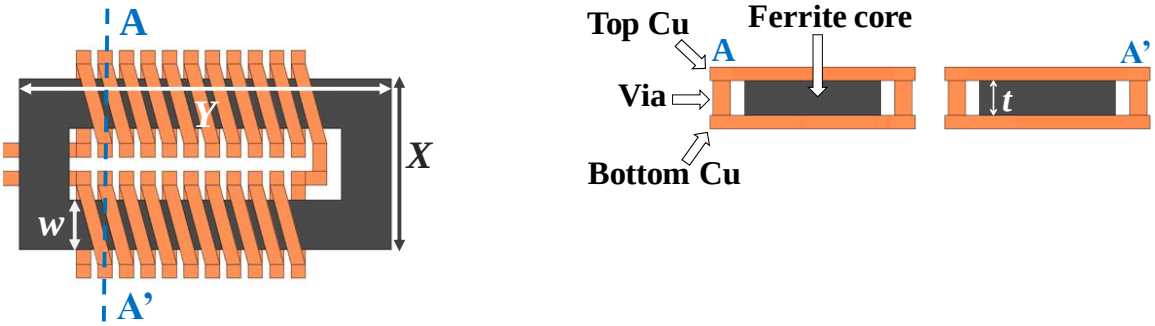

Figure 2-5: Schematic design of micro-inductors with top view and cross section

The width and length of the ferrite core are signed as *X* and *Y*. The magnetic core width is noted as *W*; *t* is thickness of the ferrite core. For copper tracks, t_c is the thickness, W_c is the width, *S* is the spacing between two tracks. Regarding vias, *x_via* and *y_via* are the width and length of cross-section; *h_via* is the height of the via.

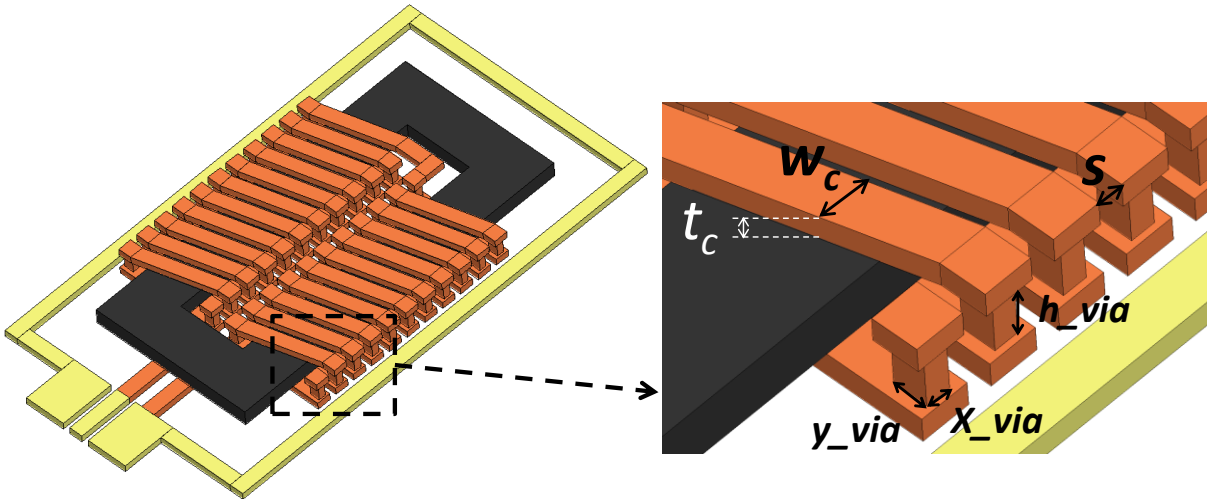

Figure 2-6 : Dimension of copper tracks and vias

The total thickness of the micro-inductor should be less than 250 µm to constitute a competitive solution in comparison to current commercial inductors and compatible with IPDiA's current technology as mentioned in chapter 1. To avoid difficulties in fabrication, the thickness of copper windings is set around 50 µm and the width of copper tracks is around 100 µm; the spacing between copper tracks is around 50 µm. With such copper tracks thickness, the magnetic core is limited to a thickness of 150 µm. For test inductors, ground-signal-ground contact pads and a ground ring are created around the inductor in order to test the device under RF probes.

Based on the target specifications of the inductor, the design was made by adjusting parameters of the core and winding dimensions. The geometrical input parameters are: core width, core length, magnetic core width, magnetic core thickness, thickness and width of copper wire and number of turns N. The output parameters are the DC and AC resistance, the total inductance and maximum magnetic induction. The first design was done with analytical expressions, given in Chapter 1. From analytical analysis, it is noticed that the larger the magnetic core width and core thickness (i.e. higher magnetic cross section) the higher the inductance of the inductor. In contrary, smaller magnetic length l ($l = 2X + 2Y - 4w$) is more favorable for high inductance. In the constrained dimension, the combination of X, Y, w, t and N that give the best output of total inductances, DC and AC resistances was selected for the test inductor. At the first place, only one preliminary design will be realized with four selected ferrites with which the pre-estimated inductances will be in the targeted range 200-1000 nH. A comparison will be made in order to find out the best magnetic core material for the inductor that can obtain high inductance at 5-10 MHz and generate smallest losses. This design is only preliminary due to lacks of information on material properties (losses vs. frequency, losses vs. B_{AC}, permeability vs. frequency, permeability vs. H_{DC}) but this design is necessary to define realistic core dimensions, i.e. close to optimized version. In the first run of experiment, the magnetic core width is 350 µm; these cores will be integrated in the micro-inductor with 21 turns of winding. Permeability and core losses density characterization of the developed ferrite materials shaped in the chosen dimensions will be carried out.

Eventually, we plan to include the extracted magnetic properties from these realized cores into future design optimization (see chapter 4).

The first geometrical inductor design is given in Table 2-1.

Table 2-1 : First geometrical inductor design

X	1 mm	W_c	100 µm
Y	2.6 mm	t_c	50 µm
W	350 µm	*S*	50 µm
t/h_via	110-140 µm	*x_via*	50µm
N	21	*y_via*	50 µm

For the purpose of process development and characterization, the version x2 and x3 of the designed inductor will be realized beside the original one. The original one is the x1 version with dimension stated in Table 2-1. For x2 and x3 version, the core and windings are double and triple in *X* and *Y* dimension, the thickness is kept the same.

3. Core realization

In order to serve characterization purposes, fully sintered ferrite cores were realized by two methods from two kinds of ferrite formation, thin film ferrite tape and in-house made ferrite powder. The details are given as followed.

3.1. Core realization from commercial thin film ferrite

The commercial thin film ferrites were supplied by ESL ElectroScience including 40010 and 40011. Each thin film layer is 70 µm thick. For adequate thickness, two thin film layers are bonded together. Then, they are cut by milling machine. The cut cores are then sintered at high temperature in order to form the ferrite phase and obtain optimum magnetic properties. The details of process are as follows:

- **Step1**: *Thermo-compression of thin film ferrites*

  Two layers of thin film ferrites, 1cm x1cm in size are stacked up. They are put in between a silicon wafer and a square silicon piece. This configuration is pressed under 800 N/cm^2 for 10 minutes at 90°C under vacuum of 10^{-3} mbar in a wafer bonding machine AML AWB04. More details of bonding procedure are given in the Annex.

- **Step 2**: *Cutting core by micro-milling machine*

  The double-layer films (about 140 µm thick) were then cut by a micro-milling machine Réalméca RV2 SP (200 µm end mill); the cutting dimensions were adjusted for shrinkage occurring during the sintering phase of these materials. Details of equipment and procedure for collecting cores are described in the Annex.

- **Step 3**: *Sintering ferrite-based cut cores*

  In order to determine the sintering temperature and duration, the thermomechanical analysis (TMA) was carried out for each type of ferrite using Setsys Evolution TMA.

The principle of TMA analysis is described in the Annex. The result of TMA analysis for thin film ferrite 40010 and 40011 is shown in Figure 2-7.

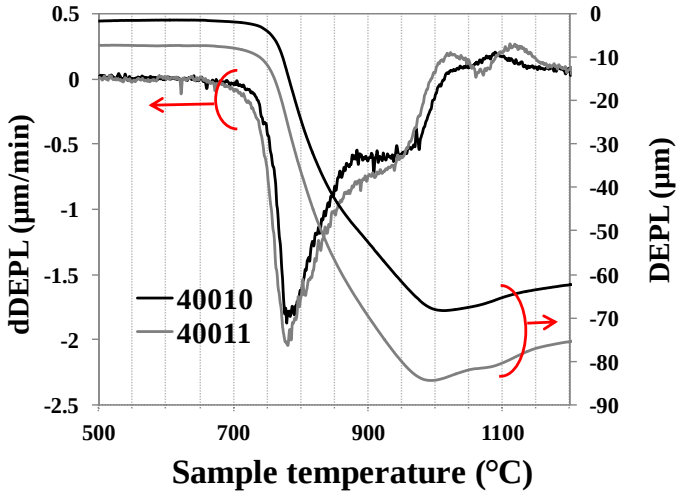

Figure 2-7 : Thermomechanical analysis of thin film commercial ferrites; DEPL is the deplacement of the sample, dDEPL is derivative of the deplacement.

The plateau regions of the derivative of displacement for 40010 and 40011 are from 850°C to 950°C; the solid state reactions happen in this range. Based on these TMA curves, the milled cores were sintered at 885°C and 950°C under flux of oxygen during 3 and 2 hours respectively. The porous ceramic plates and aluminum oxide powder sheet were used to protect cut cores from warping during sintering. The microscope image of thin film milled cores after sintering is shown in Figure 2-8. The footprint of cut cores after sintering is 1.0 x 2.6 mm^2 and the magnetic core width is 350 µm for the first design inductor (the standard deviations for the width and length of the cores are 24 µm for δ_x and 49 µm for δ_y; the standard deviation for magnetic core width δ_w is 26 µm). Core thicknesses were measured after sintering: for milled cores, thickness ranges between 108 – 110 µm.

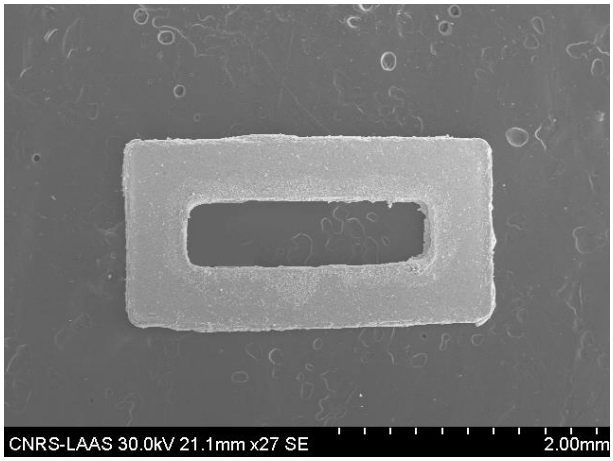

Figure 2-8 : Microscope image of ESL® thin-film milled cores after sintering

3.2. Core realization with in-house made ferrite powder by screen printing technology

The second method to realize cores is from in-house made ferrite powder namely U70 and U200 synthesized in CIRIMAT and LAPLACE laboratories, and deposited by screen printing technology in LAAS clean room.

Screen printing is a technique to fabricate thick films with high deposition rate in which the small particles of magnetic materials are suspended in a non-magnetic matrix. In screen printing, the ferrite powder is mixed with organics to form slurry. The ferrite powder is the main component of the slurry and the combination of other elements is called the vehicle. The point is that we try to load as much magnetic material as possible inside the slurry. The vehicle can be temporary or permanent. The temporary vehicle will decompose and disappear from the paste in the firing process.

NiZn ferrite powders were synthesized from metal oxides by ceramic conventional method or solid state reaction method. The ferrite powder is then mixed with organics including binders, plasticizers and dispersants provided by ESL® to form magnetic slurry. Dry film photo-resists were used to form thick photoresist molds on Kapton® polyimide substrates by photolithography technique. The ferrite paste was then filled into the mold by screen printing technique using DEK Horizon 01i equipment, followed by thirty minutes of vacuum treatment to degas the paste via a mechanical rotary pump. The ferrite composite was dried at 110°C for ten minutes and then collected manually after the photo-resist was removed. The procedure in schematic is shown in Figure 2-9. The details of processes in steps for printed cores are presented as follows:

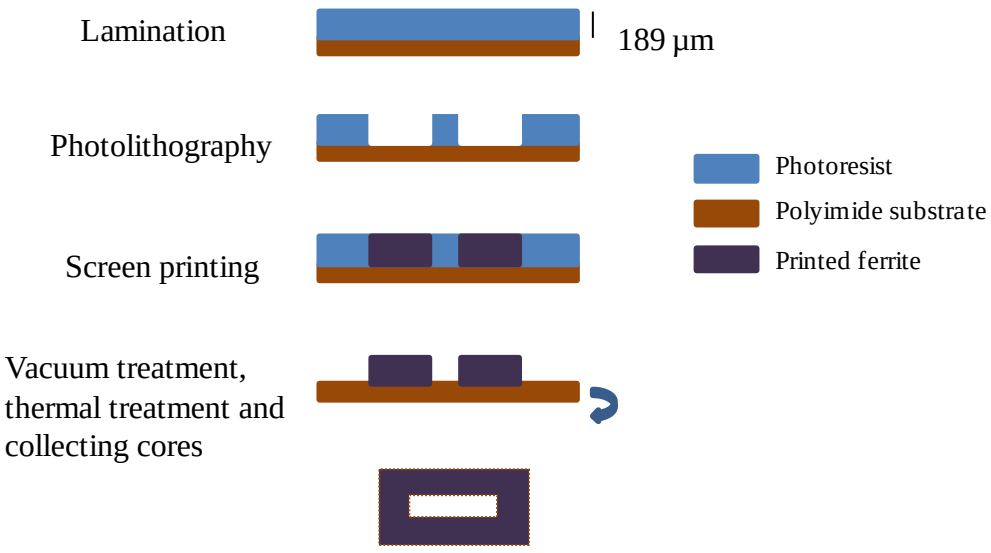

Figure 2-9 : Process for printing and collecting ferrite-based cores

- **Step 1**: *In-house made ferrite powder*

  The $Ni_{0.30}Zn_{0.55}Cu_{0.15}Co_{0.035}Fe_2O_4$ ferrite powder (U70) is made from NiO, ZnO, Fe_2O_3, Cu_2O and Co_3O_4 metal oxides by conventional ceramic processing method

according to a procedure developed in Lucas' thesis [5]. NiO, ZnO, Fe_2O_3, Cu_2O and Co_3O_4 with the molar ratio 0.3:0.55:1:0.075:0.01166 are mixed to form the original powder (U70). The original powder and 750 gram of zirconium balls (Φ = 1.2 – 1.7 mm) and 150 ml distilled water are mixed together using the attritor mixer during 30 minutes at the speed of 500 turns/minute. The slurry is taken out of the attritor and put into the furnace at 80°C until dry. The ground dried powder is put into the furnace and annealed at 800°C during 2 hours in air (with temperature rate of 200°C/hour). The annealed powder, 750 grams of zirconium balls (1.2 – 1.7 mm) and 150 ml distilled water are mixed again using the attritor mixer during 30 minutes and at the speed of 500 turns/minute. The slurry is taken out of the attritor and put into the furnace at 80°C until dry. These powders are ready to be pressed to form a ferrite pellet or mixed with organic liquids to form the ferrite paste. Problems can come from the contamination of the grinding media and the temperature of sintering. The U200 powder with the composition $(Ni_{0.24}Zn_{0.56}Cu_{0.20})_{0.965}Co_{0.035}Fe_2O_4$ (U200) was made using the same method. The composition of each fabricated powder is shown in the following table. More details on the equipments of ferrite powder fabrication are given in the Annex.

Table 2-2 : Synthesized ferrite powder (not sintered yet)

Powder	Composition	Size of particles
U70 (Ni/Zn = 0.54, Co = 0.035)	$Ni_{0.30}Zn_{0.55}Cu_{0.15}Co_{0.035}Fe_2O_4$	100-500nm
U200 (Ni/Zn = 0.43, Co = 0.035)	$(Ni_{0.24}Zn_{0.56}Cu_{0.20})_{0.965}Co_{0.035}Fe_2O_4$	100-500nm

- **Step 2**: *Making ferrite slurry*

According to ESL® recommendations, the content of ferrite powder should be around 60%-70% of the total weight when mixed with the organics. The ferrites, which have been used, are U70 and U200. The organic part includes a solvent (ESL 400A), a binder (ESL 401) and a dispersant (ESL 809) in which the solvent occupies 90%wt, binder 10%wt. Dispersant amount can be adjusted from one to some drops. The viscosity depends considerably on the amount of dispersant. The more dispersant added, the thinner the paste. Concerning the order of mixing, the ferrite powder is weighed first; then, the solvent is added into the ferrite, the combination is mixed well. A drop or some drops of dispersant are added into the mixture, and they are well mixed. Finally, the binder is weighed and added to the mixture. All are well mixed with mortar and pestle during 20 minutes to have a homogenous paste without aggregation. The viscosity of paste is very important for the success of screen-printed core. Therefore, three pastes were made varying the viscosity range: their compositions are given in the following table:

Table 2-3 : The composition of fabricated pastes

Paste P1	%m Powder	%m Organic Part		
	60%wt	40%wt		
	6g	4g		
		Solvant 400A	Dispersant 809	Binder 401
		90%wt	Some drops	10%wt
		3,6g	Some drops	0,4g

Paste P2	%m Powder	%m Organic Part		
	70%wt	30%wt		
	7g	3g		
		Solvent 400A	Dispersant 809	Binder 401
		90%wt	Some drops	10%wt
		2.7g	Some drops	0.3g

Paste P3	%m Powder	%m Organic Part		
	75%wt	25%wt		
	15g	5g		
		Solvent 400A	Dispersant 809	Binder 401
		90%wt	Some drops	10%wt
		4.5g	Some drops	0.5g

- **Step 3**: *Screen printing and collecting printed cores*

Kapton polyimide 500N® substrate was used and photolithography was performed with PH2050® dry photoresist film to form the core molds. Thickness of photoresist mold achieved is about 189 µm with four layers of dry films. The basic procedure for printing and collecting ferrite-based core is shown in Figure 2-9. The screen printing was carried out with P1, P2 and P3 paste.

- Screen printing with P1 paste (60% of ferrite powder)
  The P1 paste is too thin; hence, printed core is too thin and fragile. It was not possible to collect printed cores from P1 paste without breaking them.
- Screen printing with P2 paste (70% of ferrite powder)

The screen printing condition is pressure of 3 Kg, speed of 20 mm/s, 2 passes parallel. A layer of Kapton polyimide substrate 500N® was used to create a space between the squeegee and the substrate (see the Annex). The paste sticks on the squeegee after the first pass, then, in the second pass, there isn't enough paste in the wanted area. The printed core is degassed by vacuum in 30 minutes right after printing. It is verified that the problem of bubbles is eliminated by vacuum degas. The wafer is then slowly heated from 110°C (with a step at this temperature until the paste becomes dry) then 120°C, 130°C, 140°C and 160°C, for 1 minute at each temperature and finally, the dry photoresist film was peeled off and printed cores were collected by bending the polyimide substrate. The good point of screen printing with P2 paste is that the paste

is well thixotropic i.e. the paste has its viscosity which decreases when the force is applied on it and it returns to thicker upon standing. The printed core with P2 is quite homogenous at the center. However, the paste is thin and the printed core is thin as well. The paste can't be fully filled inside the mold at some places. Near the edge, a much thicker ring is formed and in the center the layer is much thinner (see Figure 2-10). It was only possible to collect without breaking x3 cores, not x2 and x1 cores. The x1 core is the one as designed for the first micro-inductor with the dimension stated in Table 2-1. The x2 and x3 cores are the ones with double and triple dimension in *X* and *Y*, the thickness *t* is the same as the x1 core.

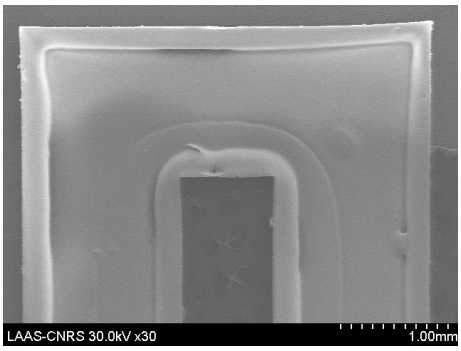

Figure 2-10 : Topology of x3 core printed from P2 (70% of ferrite powder)

- Screen printing with P3 paste (75% of ferrite powder)

In another try, P3 paste was used to print with screen printing machine without stencil mask using Kapton® polyimide support. Print condition is pressure of 3 Kg, speed of 20 mm/s and 2 passes parallel. Vacuum degas is 30 minutes right after printing. Problem of bubbles is eliminated by vacuum degas. Heat treatment process for P3 paste is similar to the treatment procedure applied for P2 paste. Then, the dry film was peeled off and printed cores were collected. With P3 paste, the pressure of 3 Kg gives good results. A thick layer can be printed and we succeeded collecting x1 cores (see Figure 2-13). Yet, because of the high ratio of powder and the small ratio of binder and dispersant, the paste is thick and difficult to deform during vacuum and heat treatment. The top topology of the x1 printed core is not totally flat (see Figure 2-13). The cores, especially the big ones, should be removed right after heat treatment for higher efficiency of collecting cores. Bending wafer is good for removing big cores. The small x1 cores were easily collected.

In this thesis, P3 paste was selected to fabricate printed cores. In next step, printed cores will be sintered.

- **Step 4**: *Sintering ferrite-based printed cores*

  The results of TMA analysis for printed U70 and U200 ferrites are shown in Figure 2-11. Based on these results, the printed U70 and U200 cores were sintered at 980°C during 2 hours under flux of oxygen. The porous ceramic plates and aluminum oxide powder sheet were used to protect printed cores from warping during sintering (see Figure 2-12). Low magnification SEM images of the printed core after sintering are shown in Figure 2-13. About one hundred cores were fabricated and ten samples were measured for dimensions. The footprint of the printed cores after sintering is 1.0 x 2.6 mm^2 with the standard deviations δ_x of 15 µm and δ_y of 30 µm; the magnetic core width is 350 µm with the standard deviation δ_w of 10 µm. The thickness of printed cores after sintering is in the range 90-105 µm.

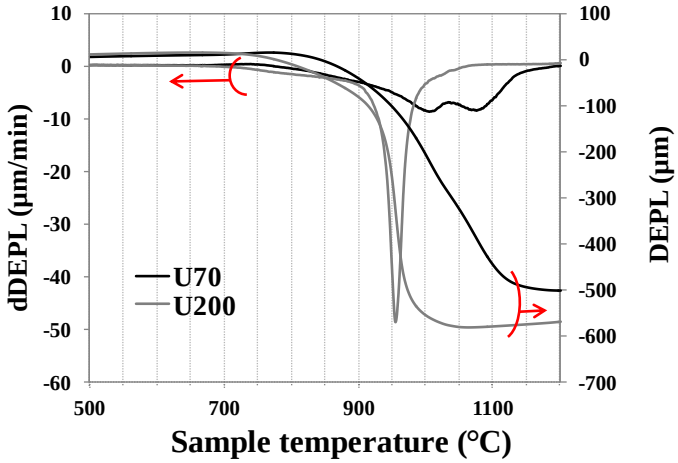

Figure 2-11: Thermomechanical analysis of in-house made ferrites

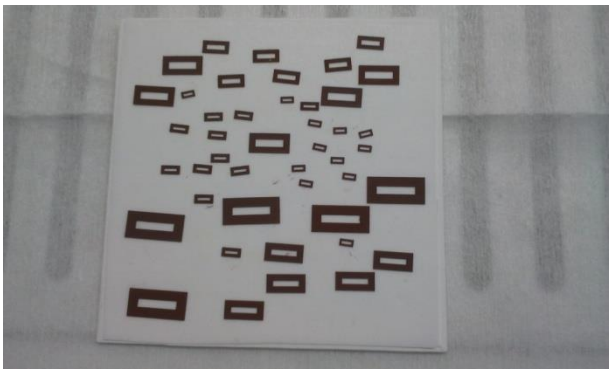

Figure 2-12: Printed cores were placed on the porous ceramic plates and aluminum oxide powder sheet (another aluminum oxide powder sheet and porous plate were placed on top of that before putting into the furnace) in order to avoid the warping of cores during sintering

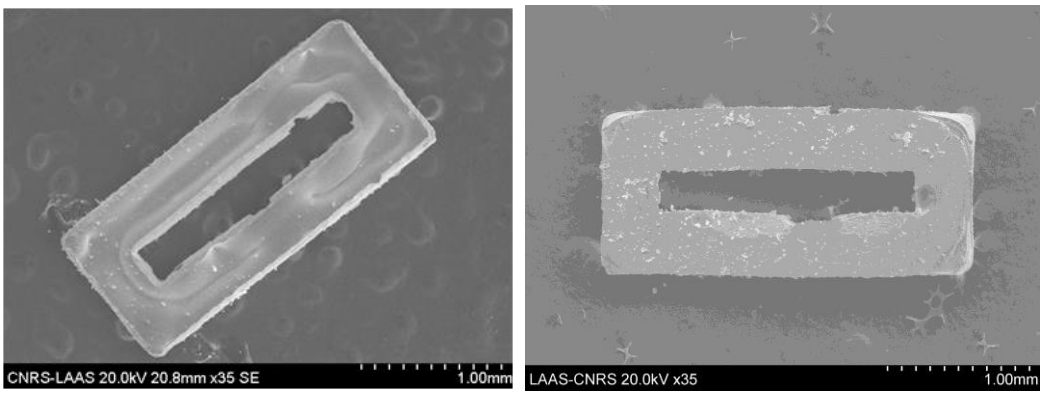

Figure 2-13: Microscope image of printed ferrite cores after sintering (top and bottom view), the small white particles on top of the core are made of aluminum oxide powder coming from the sintering process

Conclusion

Fully sintered ferrite cores were successfully realized from commercial thin film ferrite tapes and in-house made ferrite powders. Both cut cores and printed cores are reproducible in size, thickness and composition. The cut cores from commercial thin film ferrite have a more homogenous topology in the surface than screen printed ferrite cores. However, the dimension of cut cores is less precise than the printed ones due to the error deviation of cutting machine. Further development may be needed to improve the surface topology of printed cores, for example by using the stencil mask for the process of printing or applying a pressure on the printed core surface before the heat treatment process.

In the next chapter, both cut cores and printed cores will be fully characterized.

References

1. A. Goldman, *Modern Ferrite Technology*, 2006, USA Springer, 438.
2. V. Sepelak, I. Bergmann, S. Indris, A. Feldhoff, H. Hahn, K. D. Becker, C. P. Grey, and P. Heitjans, "High-resolution Al-27 MAS NMR spectroscopic studies of the response of spinel aluminates to mechanical action", *Journal of Materials Chemistry*, 21 (23), 8332-8337, 2011
3. P. W. Anderson, "New Approach to the Theory of Superexchange Interactions", *Phys. Rev.* , 115 (2), 1959
4. L. E. Smart and E. A. Moore, *Solid State Chemistry: An Introduction, third Edition*, 2005 Taylor and Francis.
5. A. Lucas, "Etude et mise au point de transformateurs large bande radiofréquence", *L'Ecole normale superieure de Cachan*, PhD thesis, 234, 2012
6. T. G. Pokhil and B. M. Moskowitz, "Magnetic domains and domain walls in pseudo-single-domain magnetite studied with magnetic force microscopy", *Journal of Geophysical Research-Solid Earth*, 102 (B10), 22681-22694, 1997
7. C. L. Dennis, R. P. Borges, L. D. Buda, U. Ebels, J. F. Gregg, M. Hehn, E. Jouguelet, K. Ounadjela, I. Petej, I. L. Prejbeanu, and M. J. Thornton, "The defining length scales of mesomagnetism: A review", *Journal of Physics-Condensed Matter*, 14 (49), R1175-R1262, 2002

8. M. Mu, Y. Su, Q. Li, F. C. Lee, "Magnetic Characterization of Low Temperature Co-fired Ceramic (LTCC) Ferrite Materials for High Frequency Power Converters", *2011 IEEE Energy Conversion Congress and Exposition (ECCE)*, 2011

Chapter 3 Soft ferrite core characterization

1. Introduction

The ferrite cores were successfully fabricated by milling and screen-printing techniques as presented in chapter 2. The ferrite core plays an important role in the inductor's performance; i.e. the properties of cores are necessary to design an inductor and magnetic properties of Ni-Zn ferrite core are sensitive to the chemical composition (Ni/Zn ratio, Co rate), and microstructure of cores (grain size, porosity). In particular, permeability is an indispensable parameter when designing inductors: high values of permeability are needed to reach high inductance density. Besides, it is important to extract losses in the magnetic core. Core losses are expected to be low in order to achieve high efficiency. All those properties should be evaluated before inductor fabrication. Four ferrites including two commercial ferrites: ESL 40010®, ESL 40011® (named 40010 and 40011 for this thesis) and two in-house made ferrite: U70 and U200 were selected as magnetic materials for inductor's cores. They are good candidates with high resistivity to minimize eddy current losses. Their permeabilities are high and stable to frequencies higher than 6 MHz. In this chapter, the results from magnetic and electrical characterizations for the four materials are compared and the most suitable ferrite will be chosen for future micro-inductor fabrication.

The ferrite cores will be characterized for micro-structure, chemical composition, *B-H* curve, complex permeability, inductance versus frequency and bias current, and volumetric core losses. Micro-structure of cores was observed by scanning electron microscopy Hitachi S4800 after sintering. Compositions of different ferrites were estimated by energy dispersive analysis (EDS). The principles of SEM and EDX analysis are described in the Annex. The magnetic properties or static B-H curves of thin film ferrites were characterized by a vibrating sample magnetometer (VSM) Versalab™ - 3 Tesla Cryogen-free from Quantum Design. The principle of VSM is given in the Annex. To extract the complex permeability of the ferrite materials, toroid shape samples were also prepared and measured in a magnetic material test fixture Agilent 16454A on an impedance analyzer Agilent 4294A. The dimension of tore samples was selected according to the sizes of the fixture holders in the test kit. Eventually, in order to extract magnetic properties such as inductance and core losses of fabricated rectangular cores, specific test inductors were fabricated.

2. Microstructure and composition analysis

Magnetization processes in the material are dependant not only on the composition but are also structure sensitive. It is known that there are two magnetization mechanisms: (i) magnetization by domain wall motion (ii) magnetization by spin rotation [1]. In the first mechanism, the intragranular porosity disturbs the domain wall motion. The domain wall of each grain is pinned to the grain

boundary. It means that the domain wall size corresponds to the grain size which is accessible via microstructure. It is important that the grains present no inclusion or pore which would pin the wall. Hence, it is interesting to study the microstructure of the material beside the composition.

Figure 3-1 shows the microstructure of different ferrites. The grains of thin-film 40010 and 40011 have a bimodal distribution, with large grains of 5-8 µm, covering around 50% of the volume, and small grains of 2-3 µm in diameter. Grain sizes of printed ferrite U70 and U200 are in the range of 1.5-6 µm. For all cores, the shrinkage was measured to be 15-20% with no cracks.

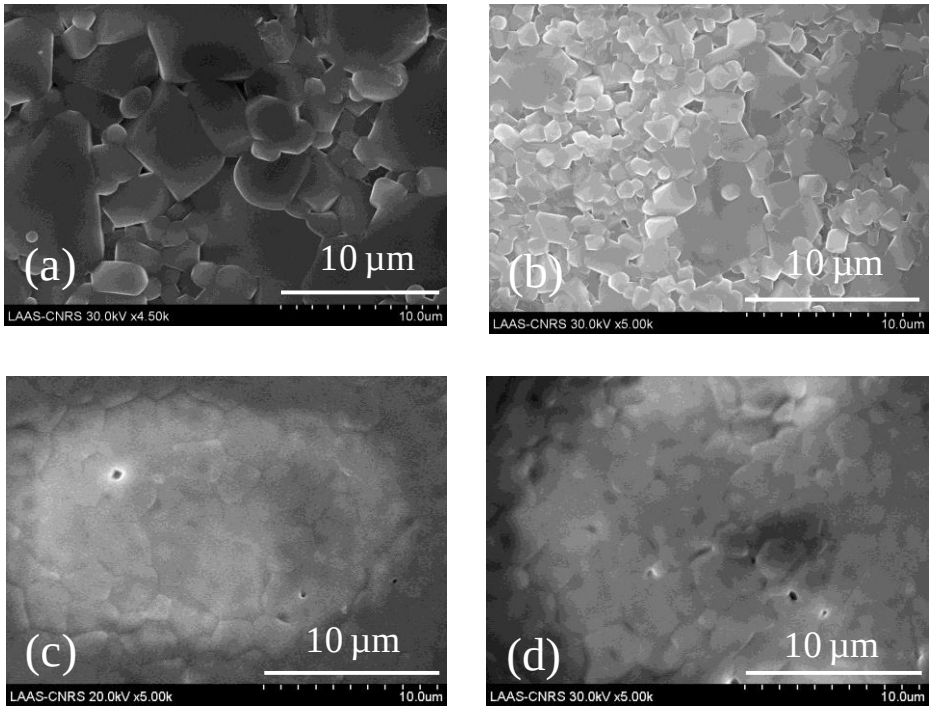

Figure 3-1. SEM images of ferrite microstructure for (a) 40010 sintered at 950°C/2hours and (b) 40011 sintered at 885°C/3hours, (c) (d) U70 and U200 sintered at 980°C/2hours

Grains formed with clear boundary means full sintering which enables optimum permeability. The initial permeability of ferrite depends on composition, but for a given composition it depends on microstructure and density of the material [2]. The porosity acts as a gap between grains which reduce permeability. Similarly, total losses of ferrites strongly depend on density and microstructure. Inter-granular porosity does not ensure a good continuity of magnetic field lines and hence, result in losses. In the case where ferrites are over sintered, with too high temperature or for too long period, grains are over grown; the defects will be created as pores inside the grains, or so-called intra-granular pores. These defects can trap the magnetization movement and degrade the magnetic properties. Hence, in order to have good magnetic properties in terms of initial permeability and losses, it is important to have fine and homogeneous microstructure and the best densification with less porosity, especially without intra-porosity.

The compositions of ferrites in the study are listed in Table 3-1. Ni/Zn ratio is higher for 40010 than for 40011. It is reported that higher Ni/Zn ratio brings lower permeability for Ni-Zn ferrite because the

increase of Ni will result in increasing of magneto-crystalline anisotropy which manifest itself by a decrease of permeability [2]. The higher magnetic anisotropy energy blocks the rotation movement of domain walls which will reduce the losses associated with this phenomenon.

Table 3-1. Composition of different ferrites estimated by SEM-EDS

Ferrite	**Composition**
40010 (Ni/Zn = 1.49)	$Ni_{0.49}Zn_{0.33}Cu_{0.18}Fe_2O_4$
40011 (Ni/Zn = 0.47)	$Ni_{0.28}Zn_{0.60}Cu_{0.12}Fe_2O_4$
U70 (Ni/Zn = 0.55, Co = 0.035)	$(Ni_{0.30}Zn_{0.55}Cu_{0.15})_{0.965}Co_{0.035}Fe_2O_4$
U200 (Ni/Zn = 0.43, Co = 0.035)	$(Ni_{0.24}Zn_{0.56}Cu_{0.20})_{0.965}Co_{0.035}Fe_2O_4$

3. Magnetic characterization

3.1. Static B-H curves

When the ferrites are placed in a magnetic field, the magnetization induction appears in the material. This reaction/behavior is expressed in the *B-H* curve, in which *H* is external magnetic field and *B* is the magnetization induction inside the ferrite. In here, the measurement is carried out with vibration frequency of 40 Hz and room temperature. The *B-H* characteristics of four ferrites are presented in Figure 3-2. The measured samples are free-standing, about 110 µm thick in a square dimension of 2x2 mm^2. The saturation induction obtained is in the range of 0.25-0.30 T, with a coercive field of 0.8-5.8 Oe (or 53-462 A/m). 40010 exhibits the highest coercive field which is due to the highest amount of magnetic phase (Ni and Fe) in 40010 ferrite compared to other ferrites ; a similar effect was observed when doing some copper substitution into Ni-Zn ferrites [3]. Magnetic remanences are 0.8-8% of the saturation magnetization.

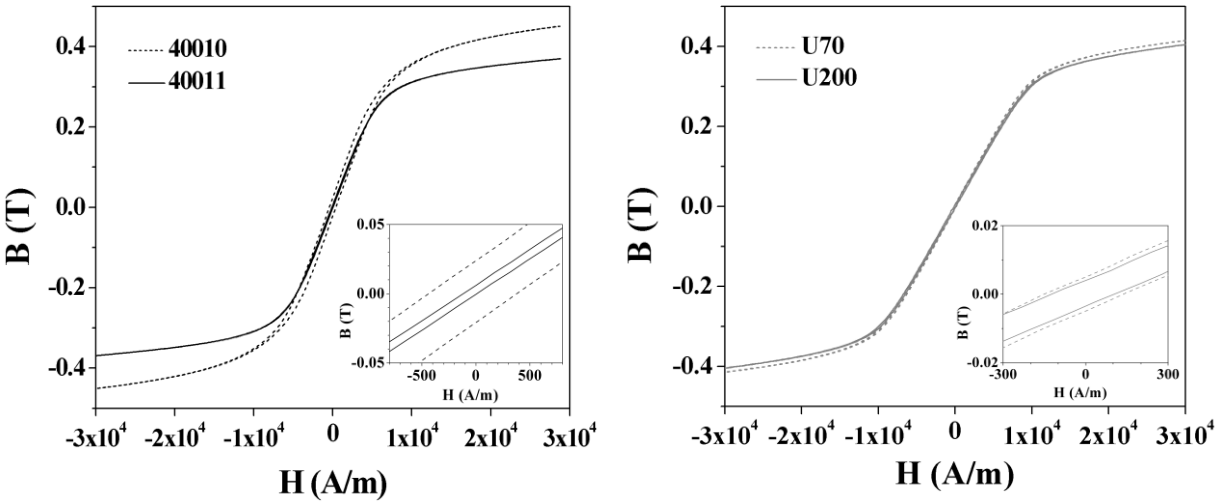

Figure 3-2. B-H curves of thin film ferrite measured by VSM, f = 40 Hz

It has to be noted that the slope of this static *B-H* curve doesn't reflect the dynamic value of permeability. At the functional mode of the applications, like integrated inductor in power converter, the ferrite is placed under much higher alternating magnetic field and the slope of the dynamic curve is

different from that of the static one. Beside, biasing a magnetic material with DC current will shift the minor alternating *B-H* loop (see Figure 3-3) and also have an effect on the effective permeability and the core losses. However, these static *B-H* curves are still necessary for us to study the saturation induction and coercivity and also to compare different materials.

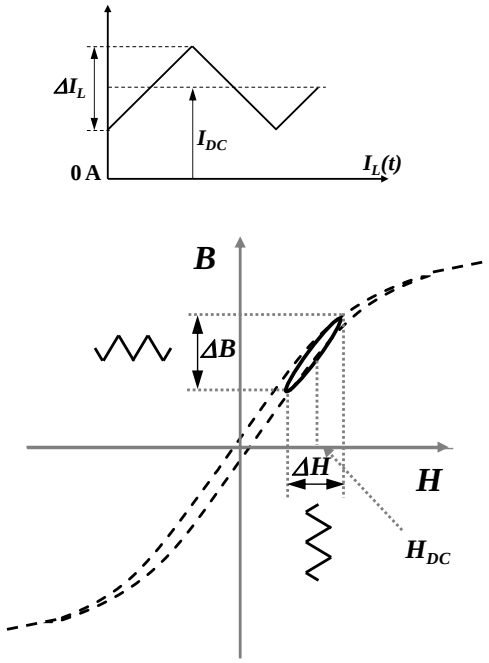

Figure 3-3: Novel dynamic B-H curve of ferrite in the integrated inductor under functional mode of the voltage converter[4]

3.2. Complex permeability

To extract the complex permeability ($\mu_r^* = \mu_r' - j\,\mu_r''$) of the ferrite materials, toroid shape samples were prepared and measured in a magnetic material test fixture Agilent 16454A on an impedance analyzer Agilent 4294A. The principle of this measurement is given in the Annex. The dimension of tore samples was selected according to the sizes of the fixture holders in the test kit.

Figure 3-4: Complex permeability measurement set-up; b and c: respectively internal and external diameter of the tore; h: thickness of the tore

The complex permeability of each material (40010, 40011, U70 and U200) was extracted as a function of frequency (as shown in Figure 3-5) from impedance measurements of ferrite tores mounted on the magnetic test fixture using the following equation:

$$\mu_r^* = \frac{2\pi(Z_m^* - Z_{sm}^*)}{j\omega\mu_0 h \ln\frac{c}{b}} + 1 \qquad \textit{(Eq. 3.1)}$$

in which Z^*_m is the impedance of the test fixture with the tore and Z^*_{sm} is the impedance of the test fixture without the tore; ω is measurement oscillation frequency $\omega = 2\pi f$, μ_0 is permeability of free space, h is thickness of the tore; b and c are internal and external diameter of the tore respectively.

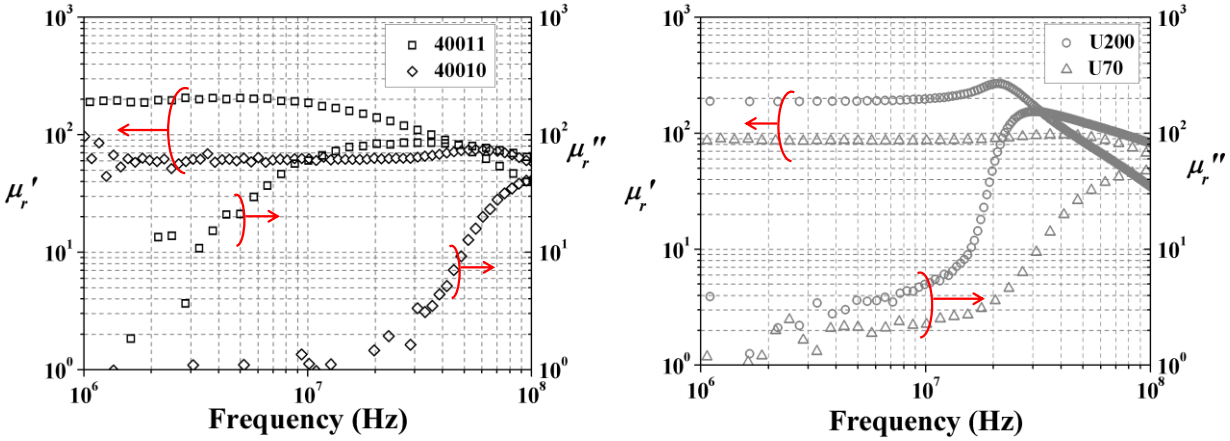

Figure 3-5: Measured complex permeability: ESL 40010® and 40011® ferrites sintered at 950°C/2h and 885°C/3h (b=4 mm, c=6 mm and h= 108 µm), U70 and U200 home-made ferrites sintered at 980°/2h (b=5 mm, c=14 mm and h=1.5 mm)

40011 ferrite presents a permeability of 200 stable up-to 10 MHz while for 40010; it is 60 and stable until 70 MHz. These measured values correspond to values provided by ESL®. The secondary permeability of 40010 at zero DC bias and small AC signal is small up-to 50 MHz, whereas that of 40011 increases quickly from 1-3 MHz. Since, higher secondary permeability (μ_r'') means higher losses, we expect higher losses from 40011 compared to 40010.

U70 and U200 have permeabilities of 86 and 190 stable up to 50 MHz and 10 MHz respectively. From the comparison of μ_r'', it is expected that U200 exhibits higher losses than U70.

When comparing U200 with 40011 films at 6 MHz, which is the frequency of interest: both show high primary permeability. However, secondary permeability for 40011 films is much higher than U200 film. We thus expect higher core losses density for 40011 than for U200 under the same operating conditions. Losses of U200 ferrite are small thanks to the cobalt contribution, as reported by Lucas [2]. Table 3-2 summarizes magnetic properties of selected ferrites.

These values of permeability will be used for inductor design. However, in these measurements, the excitation current is small (< 20 mA rms), i.e. small induction (< 0.4 mT); hence, these values of permeability can only be considered for the case of zero DC bias and small alternating excitation current.

Table 3-2: Magnetic properties of different ferrites

	40011	**40010**	**U200**	**U70**
Permeability μ_r'	200	60	190	86
Saturation induction B_s (T)	0.25	0.30	0.25	0.25
Coercive field H_c (Oe)	0.8	5.8	1.5	1.9
Resonance frequency f_{res} (MHz)	30	>100	30	100

In order to characterize the core performance while it is integrated in the inductor, test inductors are made with rectangular ferrite cores wounded by electroplated copper tracks and bonded gold micro-wires. The following section reports on the electrical characterization of these test inductors which lead to the extraction of magnetic properties (complex permeability, losses) of the ferrite cores.

4. Electrical characterization of test inductors with rectangular cores

The inductor design was made by adjusting parameters of the core and winding dimensions based on the target specifications as reported in section 2 of the previous chapter. At the beginning, only one preliminary design will be realized with four selected ferrites with the pre-estimated inductances in the targeted range. The best magnetic core material for the inductor with smallest losses at 6 MHz will be chosen after the comparison. In the first run of experiment, the magnetic core width is 350 µm; the footprint of cut and printed cores after sintering is 1.0x2.6 mm^2. These cores will be integrated in the micro test inductor with 21 turns of winding. Test inductors are fabricated on Si/SiO_2 substrate: 50 µm thick copper bottom tracks are deposited on Si/SiO2/Ti/Au wafer by electroplating through thick photoresist mold. At the end of this step, the seed layer is removed by wet etching in potassium iodide solution $KI+I_2$ for the gold layer and in a diluted HF acid solution for the titanium layer. Sintered ferrite cores are placed manually on Cu tracks. The ball-bonding 25µm-diameter gold wires are completing the winding. For test inductors, ground-signal-ground contact pads and a ground ring around the inductor are created in order to test the device under RF probes. Defined dimensions for test inductors are 1.54x2.64 mm^2 including the area occupied by the ferrite core and the copper tracks but not the ground-signal-ground contact pad and the ground ring i.e. the region inside the dash boundary in Figure 3-6. These test inductors were characterized by impedance analyzer to extract inductance and core losses. The inductances versus frequency and versus DC bias were characterized in this part using the impedance analyzer Agilent 4294A and the DC bias adapter 16200B with the current generator Keithley. The details of these apparatus are given in the Annex.

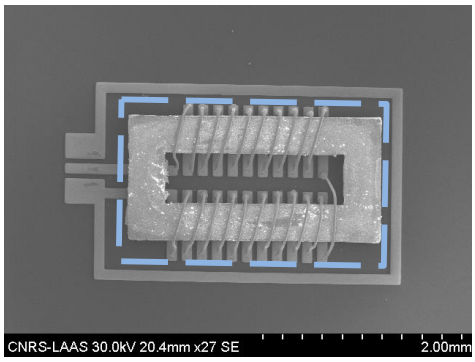

Figure 3-6: Test inductor for inductance characterization

4.1. Inductance versus frequency

Electrical characterizations were performed for different magnetic cores with 21-turn coil. Figure 3-7 shows the inductance of test inductors as a function of frequency. An inductance as high as 860 nH corresponding to 215 nH.mm^{-2} was obtained for the test inductor with 40011 core and 287 nH corresponding to 72 nH.mm^{-2} obtained for the test inductor with 40010 cores at 6 MHz while the air core inductor has only an inductance of 18 nH. The inductance of the test inductor with U200 core is 760 nH corresponding to 187 nH.mm^{-2}. An inductance of 560 nH corresponding to 138 nH.mm^{-2} was obtained for the test inductor with U70 core.

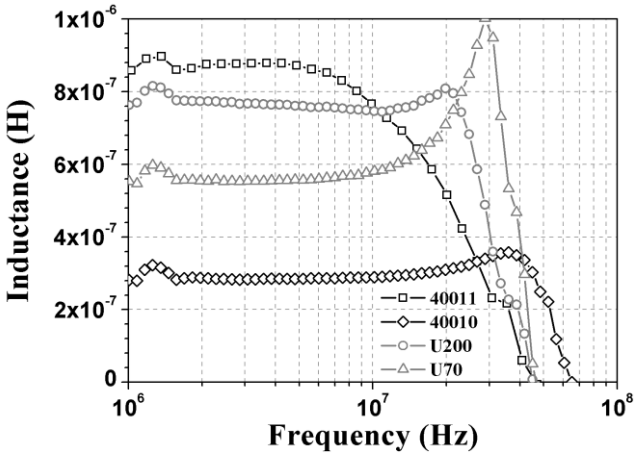

Figure 3-7: Measured inductance of the test inductors made of different cores versus frequency (I_{ACrms} = 10 mA)

These fully sintered ferrite cores can produce high values of inductance density as demonstrated. Thus, it is a real advantage for realizing small rectangular micro-inductors on chips compared to other reported non-sintered ferrite inductors [5-7]. For our target of high inductance density, 40011 and U200 are potential candidates.

4.2. Inductance versus DC bias current

Figure 3-8 shows the inductance versus superimposing DC bias current for the four test inductors. The

inductance drops quite rapidly, especially for 40011 and U200 ferrites. This is due to the non-linearity of the permeability versus DC magnetic field. The decrease of μ_r' versus pre-magnetization field was already observed by Mu et al [8]. The higher the initial permeability, the more severe is the drop. This behavior is a major drawback and it will have to be taken into account in the design optimization of micro-inductors. Meanwhile, 40010 cores have permeability more stable with DC bias current, yet they have lower permeability (see Figure 3-5 and Figure 3-8). To improve these performance, several solutions can be investigated in the future: on the material side, there are actually efforts to improve the performance by mixing the low-μ ferrite, e.g. 40010, together with the high-μ ferrite, e.g. 40011, so that they can operate at higher DC current [9]. Concerning the design, another solution might be to increase the size of the inductor: both the magnetic cross section and the magnetic length will be increased. The inductance remains at the expected value; however, the magnetic field inside the inductor under a certain DC current will become smaller due to larger magnetic length i.e. the inductor can operate at higher level of DC bias. For the latter solution, the parasitic problem caused by the larger copper tracks need to be considered.

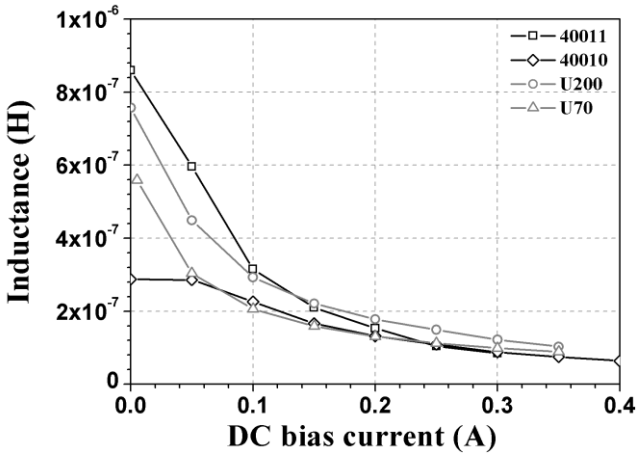

Figure 3-8: Measured inductance of the test inductors made of different cores versus DC bias current at 6 MHz (I_{ACrms} = 10 mA)

To summarize, the inductances of test inductors with different rectangular ferrite cores in footprint of 1.5x2.6 mm^2 were measured. The values are in the range 287-860 nH and stable up to 6-30 MHz at zero bias and small AC signal. DC current dependences of the inductance were characterized for four test inductors and it is shown that the ferrite with small permeability (like 40010) is more stable with DC bias current.

5. Electrical characterization for losses

Beside electrical characterizations providing expected inductance for inductors having ferrite cores, it is necessary to evaluate losses including winding losses i.e. copper losses and core losses i.e. iron losses. Electroplated copper windings are not realized at this stage, half of the test inductors'windings is done with wire-bonds: we only characterize the core losses in this part. In this part, for each ferrite

materials shaped in the chosen dimension, permeability and loss tangent are measured and then, core losses are extracted.

5.1. Requirements

The measurement method for losses must be adapted for the inductor configuration and its functional regime.

5.1.1. Test inductors

We use two types of test inductor: test inductor with magnetic core and test inductor without core i.e. air-core inductor. Triple bonding is made to reduce the resistance of test inductor. In order to make triple bonding, the size of test inductors for losses characterization is expanded three times. It is expected to minimize the influence of electrical resistance on the magnetic losses. Dimension of test inductors is shown in Figure 3-9. The number of winding is 21.

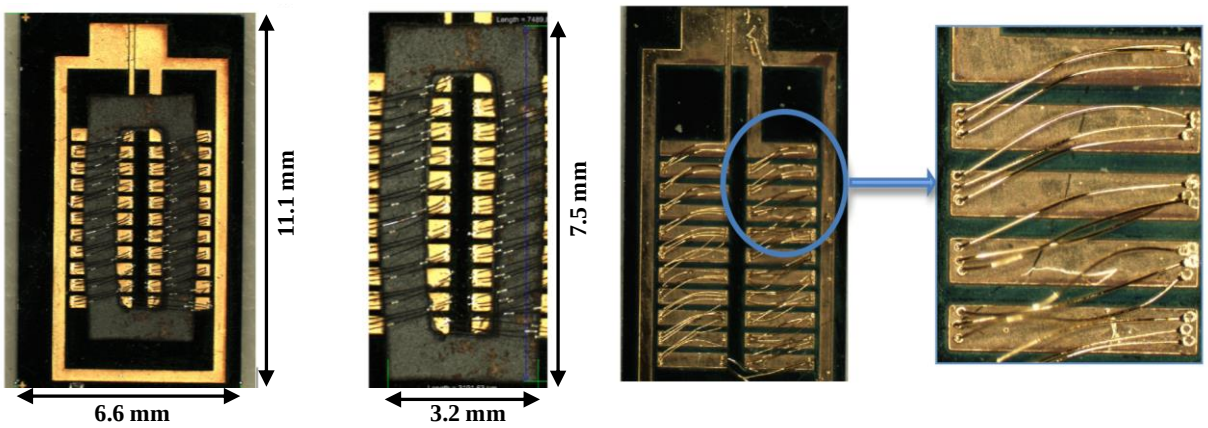

Figure 3-9: Top view of magnetic core test inductor and air-core test inductor

5.1.2. Functional regime

The objective is to determine magnetic losses of developed ferrite cores under the functional regime. Specifications defined in chapter 1 for the power DC-DC converter provide guidelines for measurements range:

- Frequency range: 1-10 MHz
- Current ripple of the inductor: in the converter, this signal is triangular with peak to peak amplitude about 200 mA. Hence, losses need to be characterized with AC signal up to 200 mA at least sinusoidal and better triangular.
- Average current in the inductor (I_{DC}): the specification indicates a converter output current of about 0.6 A. It is necessary that the losses calculation method takes into account this DC value.

All the losses will be given in $mW.cm^{-3}$.

5.2. Literature of different methods for measuring and calculating core losses

Calorimetric is generally used to extract energy losses of magnetic core in the macroscopic size [10, 11]. This method converts the difference of temperature into dissipated energy. Although the most direct, this method is not suitable for small size magnetic cores (micrometric size) such as the ones developed in this work: with losses in the order of mW, which are levels of power too difficult to detect by this technique.

The classical method to measure magnetic losses can be described as follows. The magnetic core has two windings: excitation winding and sensing winding. The voltage on the sensing winding and the current through the excitation winding are measured by oscilloscope. Then, the integral of the product of current and voltage waveforms gives the losses dissipated by the magnetic material. The advantage of this method is to exclude the winding losses from the measured core losses. One disadvantage is phase discrepancy, which will result in large error in losses calculation at high frequency. To handle this problem, one solution proposed in [12] is to add a serial resonant capacitor in the excitation winding. Similarly, one can extract losses as the product of current and voltage. But this method is not adaptable with our inductor and our measurement equipment because it requires a specific capacitor for one measured frequency with each test inductor and it is too complicated to gather all these devices. Another technique to measure losses inspired from the principle of resonance is proposed in [13]. The idea is to measure quality factor of the inductor as a function of alternating current, and then calculate indirectly the magnetic losses. The inductor is connected in series with a capacitor which will resonate at expected frequency, and then losses are obtained by approximation. However, this method only allows to measure losses at one frequency with the use of three or four circuits.

The chosen method to study losses in our project is adapted to our inductor and easy to set up for measuring at the frequency range 1-10 MHz.

5.3. Methods for losses calculation

5.3.1. Principle

The calculation of losses is effective when one of the following parameters is fixed: frequency *f*, amplitude of alternating current I_{AC}, and amplitude of continuous component I_{DC}.

An inductor can be considered in a parallel model or serial model, Figure 3-10. In two cases, we have resistance R_{CU} which is the resistance of conductor representing the copper losses. The other resistance R_S or R_P of the model represent core losses. We can choose serial model to work with constant current

or parallel model to work with constant potential. However, in the parallel model, the applied voltage to the resistance R_P can't be obtained precisely. Therefore, we choose the serial model for the method.

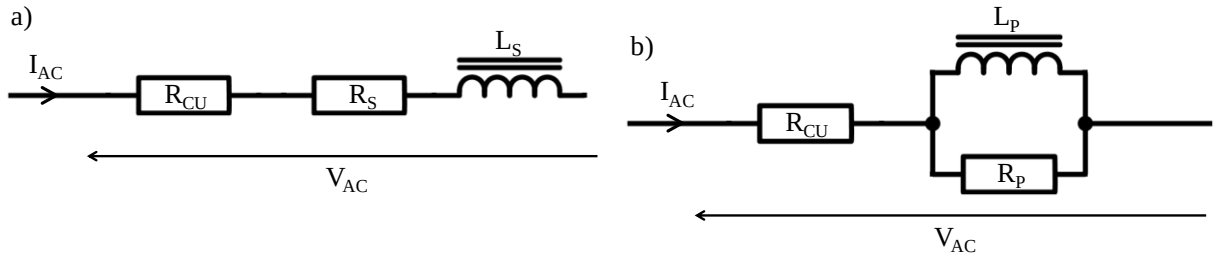

Figure 3-10: a) Serial model of the inductor and b) Parallel model of the inductor

The second step of the method is to measure the complex impedance of the air-core inductor with identical dimension of the ferrite-core inductor. We measure the resistance of the copper R_{CU} and we can define the copper losses of our inductor. We call the real part of the impedance for air-core inductor as *Re(Z)_Cu* and the imaginary part as *Im(Z)_Cu*. The complex impedance of ferrite-core inductor is measured at the same condition with the real part as *Re(Z)_ferrite* and the imaginary part as *Im(Z)_ferrite*. We subtract the impedance of the air-core inductor from the one of the ferrite-core inductor to obtain *Re(Z)_final* and *Im(Z)_final*.

$$Re(Z)\_final = Re(Z)\_ferrite - Re(Z)\_Cu$$

$$Im(Z)\_final = Im(Z)\_ferrite - Im(Z)\_Cu$$

We can extract the resistance R_S and inductance L_S from the serial model

$$Rs = Re(Z)\_final$$

$$Ls = Im(Z)\_final/(2\pi f)$$

The volumetric core losses P_v is expressed as

$$P_V = \frac{R_S * I_{ACrms}^2}{A_e * l_e} \qquad (Eq.\ 3.2)$$

With A_e is the magnetic cross-section (m^2), l_e is the magnetic length (m).

It is sometimes necessary to interpret the losses as function of magnetic field *B*. We can extract the induction B_{AC} from the current I_{AC} as followed:

$$B_{AC} = \frac{L_S I_{AC}}{N A_e}$$

We will use these calculations to observe core losses with different parameters varying (f, I_{AC}, I_{DC}).

5.3.2. Analytical model of core losses

From the experimental curves of core losses, the curve fitting is done with the Steinmetz equation to identify the coefficients α, β and K for core loss model at different conditions (f, I_{AC}, I_{DC}).

$$P_v = K f^{\alpha} {B_{ACrms}}^{\beta}$$

The least mean square method is used for fitting. The principle of least mean square method is to give α, β and K initial values and then, use the solver in Excel to find the combination of (K, α, β) that gives the minimum value to $Minerr(k, \alpha, \beta)$

$$Minerr(k, \alpha, \beta) = sum(\left(P_v - P_{v_{model}}\right)^2, f) \qquad \textit{(Eq. 3.3)}$$

5.3.3. Measurement terminal

This method is carried out with an impedance analyzer that provides the excitation terminals (f, current) for measurement and calculation. It measures complex impedance of the inductor as function of frequency, with different levels of sinusoidal current I_{AC} and allows to add a bias current I_{DC} during measurement. The impedance analyzer is connected with a computer to obtain data files. Two impedance analyzers are in fact used.

- Agilent 4284A for measuring losses without continuous component I_{DC}. The frequency range is 100 Hz to 1 MHz. Sinusoidal current can be as high as 200 mA (rms).
- Agilent 4294A for measuring losses with continuous component I_{DC}. DC current adapter Agilent 16200B is used with an external current generator. RF probe is used for measurement in the frequency range 1 MHz – 110 MHz. The alternating current I_{ACrms} cannot be higher than 20 mA.

5.4. Electrical measurements and results

In this part, for the sake of simplicity, we use two expressions to describe two electric measurement set-ups. It is called "I_{AC} losses" for the losses measured with I_{AC} and frequency as parameters by Agilent 4284A and Agilent 4294 and "I_{DC} losses" for the losses measured by Agilent 4294A (I_{DC} and frequency as parameters). The details of electric measurement set-up for I_{AC} and I_{DC} losses are given in the Annex. Test inductors with triple bonding, are measured. Their shape and dimension are described in 5.1.1.

5.4.1. Core losses versus I_{AC} sinusoidal oscillation

5.4.1.1. Complex permeability

Three parameters are interesting to understand core losses of the inductor: imaginary part of complex permeability $\mu_r''(f)$, the real part of complex permeability $\mu_r'(f)$, and the loss factor $\tan\delta(f)$ which is

the ratio of the imaginary part and the real part of the complex permeability. The results of four test inductors are presented Figure 3-11 and Figure 3-12. Generally, it is shown that $\mu_r''(f)$ increases with the rms value of I_{AC} oscillation. This represents the losses of magnetic material, hence, it is expected that the losses increase as a function of I_{AC}. This hypothesis is confirmed by the increasing of loss tangent $\tan\delta(f)$. This characteristic is quite pronounced for 40010. For 40011, the increase of μ_r'' with I_{AC} is smaller. The increase of μ_r'' is due to the coercive field and residual losses ; as it is shown in the *B-H* curve, although at low frequency, 40010 has a larger coercivity than 40011 which could explain this difference. However, with I_{AC} of 100 mA, 150 mA and 200 mA the complex permeability stays at the same level.

For real part of permeability, as I_{AC} increases from 10 mA to 200 mA, μ_r' of 40010 increases from 90 to 200 respectively. When we compare these values of μ_r' with the value measured by the Agilent magnetic test fixture we can see differences. That can be explained by the dependence of permeability on the current excitation and the magnetic core shape. For 40011, when I_{AC} increases from 10 mA to 50 mA, μ' increases from 250 to 300. An explanation for this could be that the increase of μ_r' is due to the increase of the slope of *B-H* curve with higher excitation currents.

U70 and U200 have the same characteristics as 40010 and 40011 respectively when I_{AC} increases from 10 mA to 50 mA. There is a difference with I_{AC} equal to 100mA, 150 mA and 200 mA: μ_r' increases slightly for U70 and it almost stays at the same level for U200. A peculiar phenomenon is observed for μ_r'' and $\tan(\delta)$: their value are lower for I_{AC} equal to 150mA and 200mA, than for I_{AC} equal to 100mA. Although we don't have an explanation for this particularity, Wesseling et al [14] also reported a local peak in the I_{AC} range of 0-50 mA when measuring the AC current dependence of the on-chip inductor.

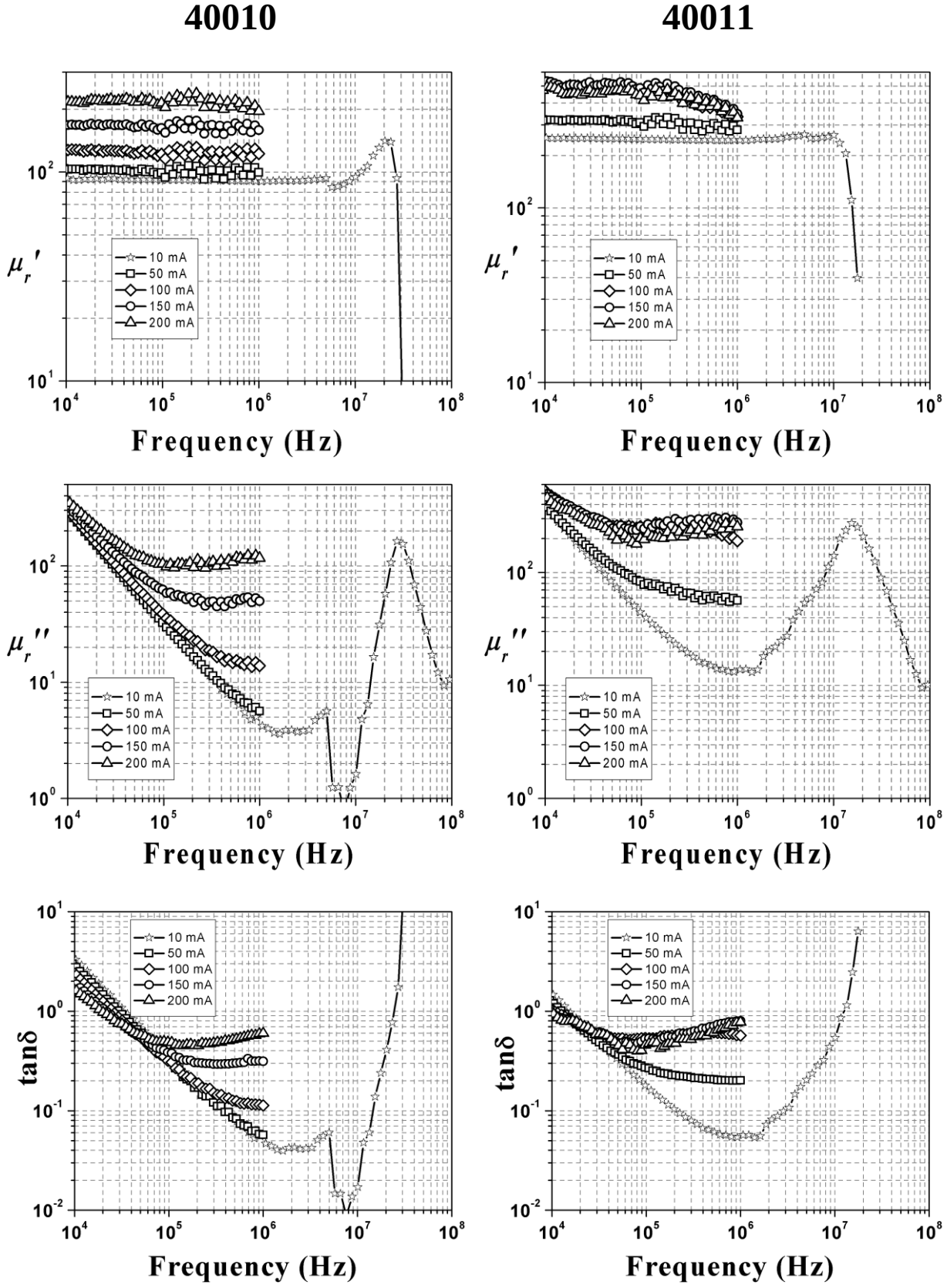

Figure 3-11: Magnetic characteristics for different value of I_{ACrms} for commercial ferrites

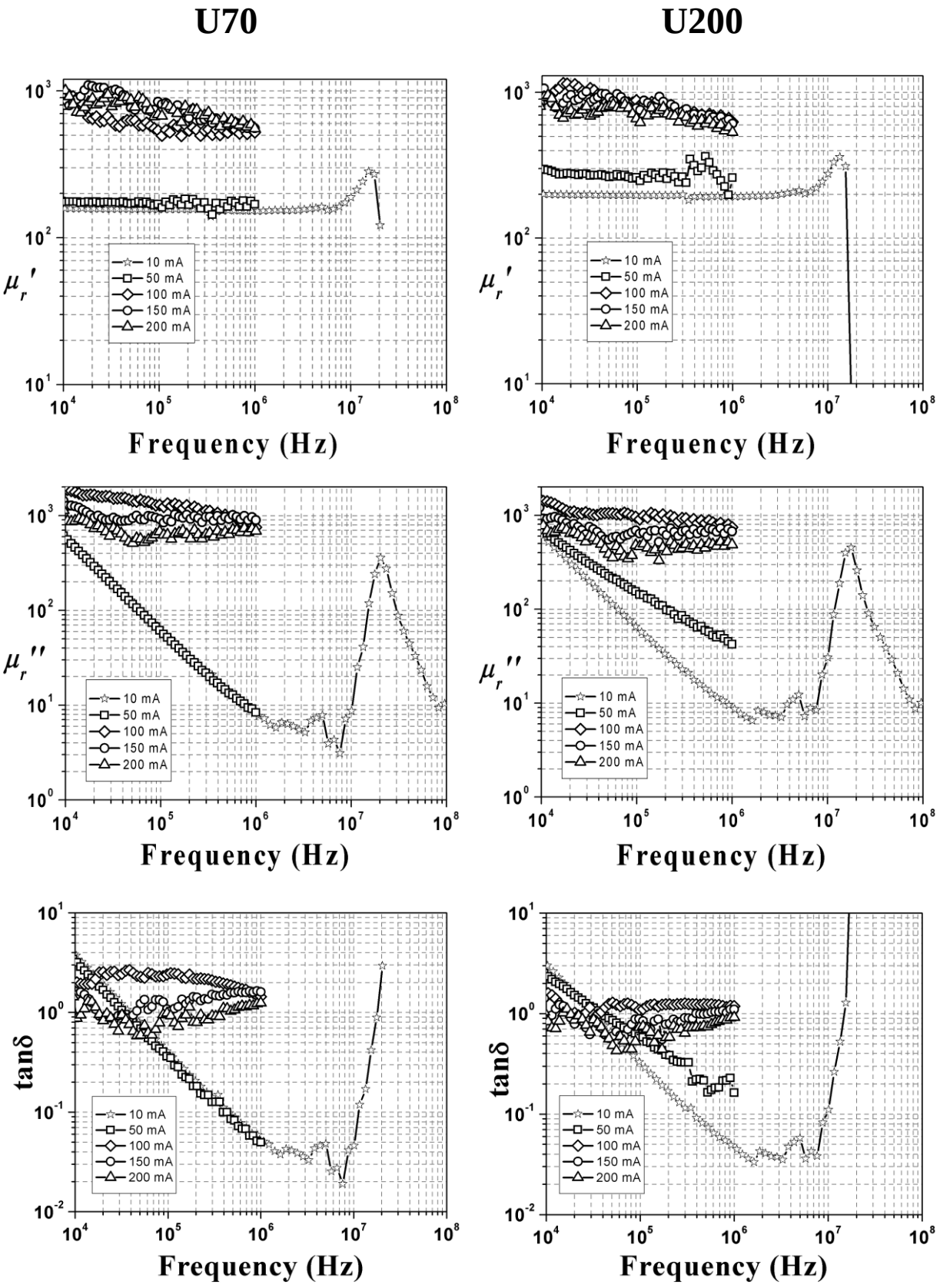

Figure 3-12: Magnetic characteristics for different value of I_{ACrms} for in-house made ferrite

5.4.1.2. Core losses as a function of frequency

5.4.1.2.1. Core losses in 100 Hz - 1 MHz range

Magnetic losses were extracted versus frequency for four ferrites as given in Figure 3-13.Measurements were carried out at different levels of sinewave signal I_{ACrms} from 10mA to 200mA with apparatus Agilent 4284A. The induction variation is referred from AC current. For 40010 and U70, the losses increase slightly with frequency for I_{ACrms} smaller than 50mA. For alternating current higher than 100mA, the losses of all ferrites increase rapidly with frequency. From the above results, it is confirmed that the magnetic losses increase with AC signal and, of course, magnetic induction B_{AC}. Losses for 40010 are smaller than 40011: for instance, at 1 MHz and magnetic induction of 11-15mT, losses for 40010 are about 100-150 mW.cm^{-3} while losses for 40011 at 12 mT are about 200 mW.cm^{-3}. The higher Ni/Zn ratio and Cu rate in 40010 compositions can explain its lower losses compared to 40011. The higher amount of Ni and Cu increase the magneto-crystalline anisotropy or magnetic anisotropy energy in the ferrite. That will block the rotation movement of the domain walls and hence, reduce the losses associated with this phenomenon.

Regarding to U70 and U200, at 1 MHz and magnetic induction of 15 mT, losses for U70 are about 150 mW.cm^{-3} while losses for U200 at 23 mT are about 300 mW.cm^{-3}. It is not easy to compare losses of U70 and U200 in these graphs. As considering the chemical compositions of these two ferrites, the Ni/Zn ratio is higher for U70, however, the Cu rate is higher for U200. Hence, the effect of magnetic anisotropy on the losses is a compromise in this case. A full comparison of losses will be given in the following section.

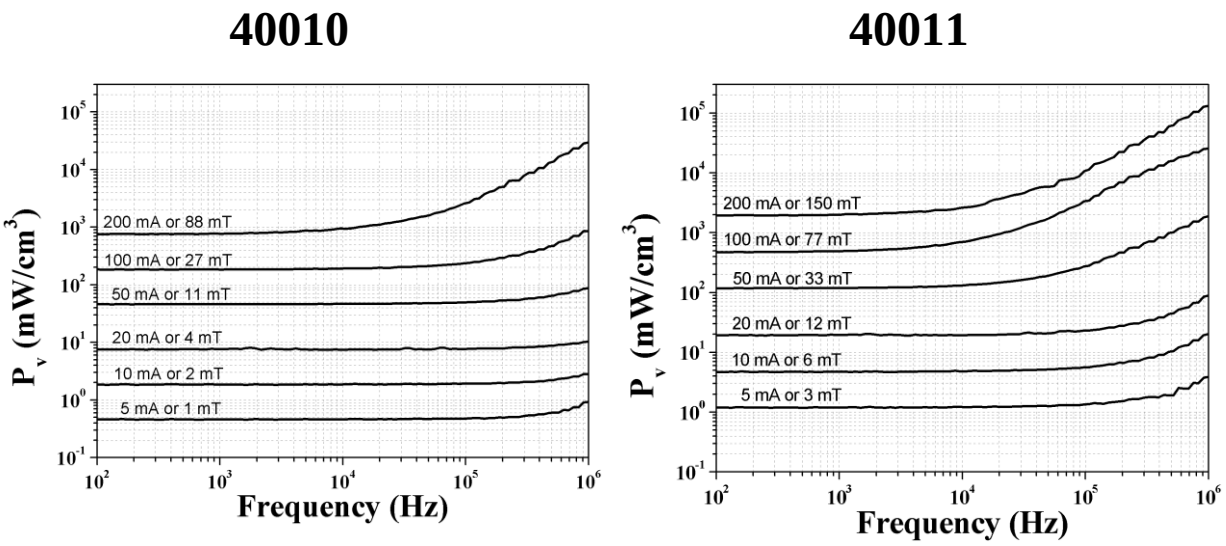

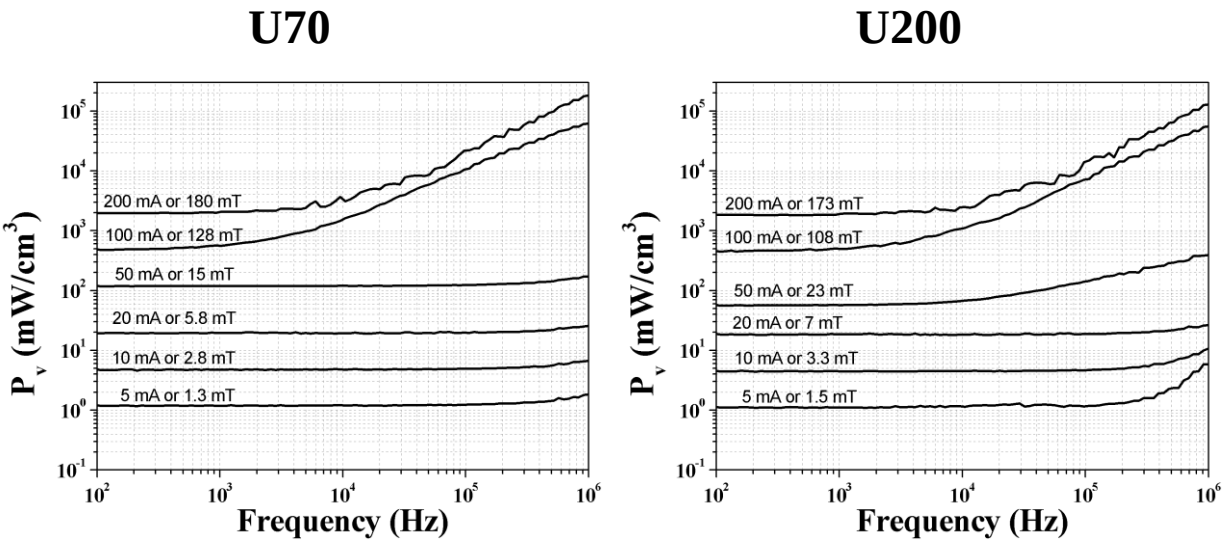

Figure 3-13: Core losses versus frequency up to 1 MHz with different values of I_{ACrms}

5.4.1.2.2. Core losses in 1-10 MHz range and model

Figure 3-14 shows extracted core losses versus frequency for four ferrites. Measurements were carried out at zero bias condition with different levels of sinewave signal I_{ACrms}: from 1 mA to 20 mA. Actually, the measurement station can't always excite this value of I_{ACrms} strictly. The actual value of excitation is recorded and used to calculate magnetic induction and losses. The induction variation is referred from AC current. As expected, losses increase with frequency and with sine wave level. Analytical models of core losses were generated by fitting the datasheet curve P_v in the range of 1-10MHz using Steinmetz equation with least squares method. Steinmetz equation works well for ferrite losses with sine-wave signal (see fitting in Figure 3-14). Table 3-3 summarizes the parameters K, α and β of the four materials for the frequency range of 1-10 MHz with zero DC bias.

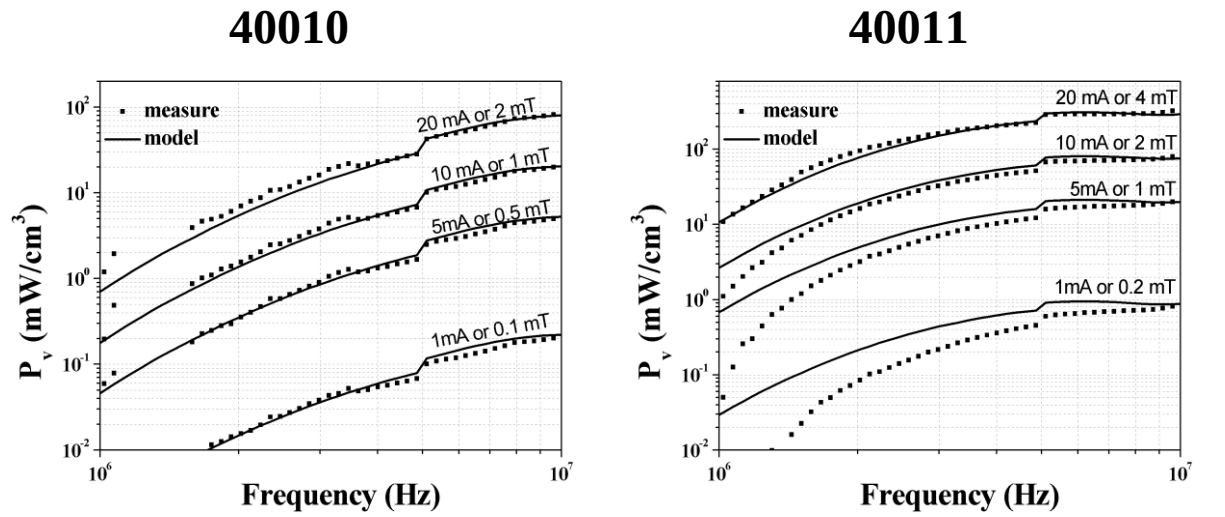

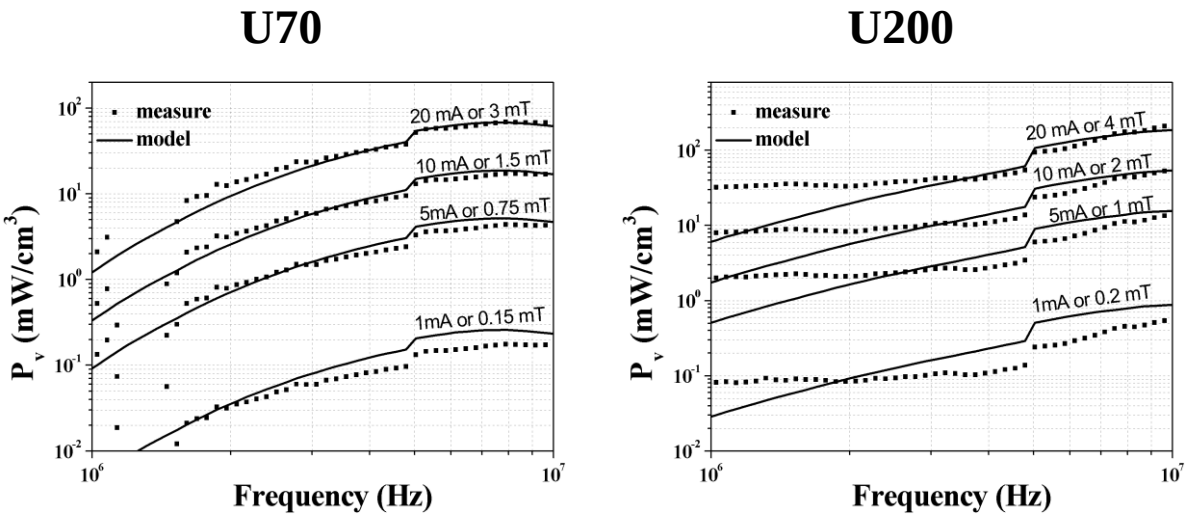

Figure 3-14: Measured and analytical core losses versus frequency

As shown in Figure 3-14, 40011 core exhibits losses about 300 mW.cm^{-3} at 4 mT and 5 MHz, comparable with the reported value of 400 mW.cm^{-3} for the same conditions by Mu et al. [8]. At 6 MHz and 2 mT, losses of 40010 are small: about 40 mW.cm^{-3}. For printed ferrites, at 6 MHz, losses for U200 at 4 mT are about 120 mW.cm^{-3} and losses for U70 at 3 mT are about 60 mW.cm^{-3}.

Table 3-3: Values of parameters K, α and β obtained for four materials at zero DC bias, apply for frequency 1-10 MHz (*) and B_{AC} = 0.1-10mT

Ferrites	***K***	α	β
40011	5.84E-09	2.263	1.879
40010	1.199E-09	2.356	1.969
U200	2.457E-08	2.071	1.790
U70	6.049E-10	2.345	1.869

(*) Except for U200 for which the fitting is only applicable at frequencies between 2.5 and 10 MHz because of instabilities in measurement below 2.5 MHz with B_{AC} = 0.1-10mT.

5.4.1.3. Core losses as a function of AC oscillation

5.4.1.3.1. Core losses with high AC oscillation level

In order to compare our value of losses with other publication, it is essential to observe core losses as function of magnetic flux inside the inductor. Figure 3.14 shows the losses for induction varying from 1 to 200 mT at 1 MHz. Losses of four ferrites seem very different at the same level of I_{AC} (see Figure 3-13). However, as comparing with reference of B_{AC}, the difference of losses for four ferrites at 1 MHz is not obvious for high induction level, as shown in Figure 3-15.

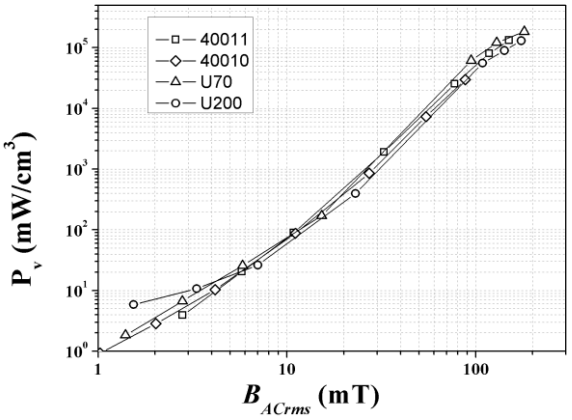

Figure 3-15: Core losses of four ferrites as a function of induction variation at 1 MHz

5.4.1.3.2. Core losses with low AC oscillation level

We observe the losses as function of B_{AC} oscillation, from 0.1 to 10 mT, at three frequencies: 1 MHz, 3 MHz and 6 MHz. Losses increase with B_{AC} and frequency. The results are presented in Figure 3-16. The solid lines are extrapolated from the loss models of four ferrites as given in Table 3-3.

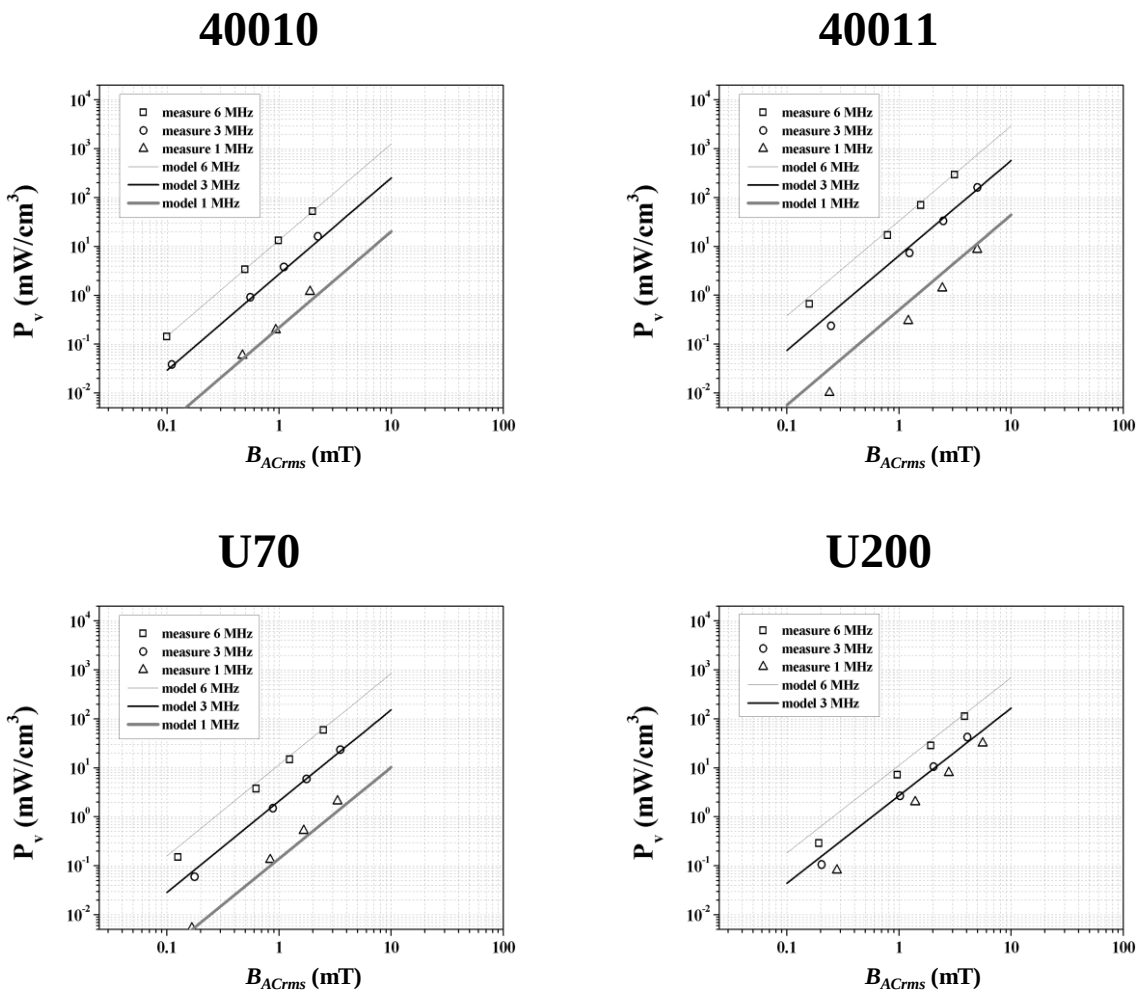

Figure 3-16: Core losses as a function of induction variation at 1 MHz, 3MHz and 6 MHz, at zero DC bias

5.4.2. Core losses versus DC current

At the working condition in our application, there's a continuous current imposed on the component. Therefore, it is interesting to observe the properties of ferrite cores under DC bias condition. Magnetic properties and losses of four ferrites are measured with bias current I_{DC} (from 0A to 1.4A) and frequency as parameters.

5.4.2.1. Complex permeability

The complex permeability of test inductors as function of frequency and amplitude of continuous current I_{DC} are shown in Figure 3-17 and Figure 3-18. As opposed to the case of I_{AC}, the continuous bias current I_{DC} causes μ_r' to decrease quite drastically. It can be seen that the higher the amplitude of continuous component I_{DC} the lower the complex permeability. The ferrite cores of test inductors gradually saturate with DC bias currents as we can see in Figure 3-8. μ_r' of 40010 is more stable with DC bias current than that of 40011. From 0 to 0.2 A of bias current, the value of μ_r' for 40010 decreases just a little; but for 40011 it decreases from 260 to 130. μ_r'' also decreases when increasing I_{DC}. However, $\tan\delta$ increases with frequencies up to 10 MHz for 40010 and 40011. Indeed, the big decrease in μ_r' reflects on the $\tan\delta$ and it only happens at low frequencies (< 10 MHz). Above 10 MHz, $\tan\delta$ has the same behavior as μ_r'', i.e it decreases with I_{DC}. For U70 and U200, the phenomenon is similar. The $\tan\delta$ increases with frequencies up to about 15 MHz with the increase of DC bias. μ_r' decreases considerably with DC bias current. With 1.4A of bias current, μ' of U70 is almost close to that value of U200, about 10.

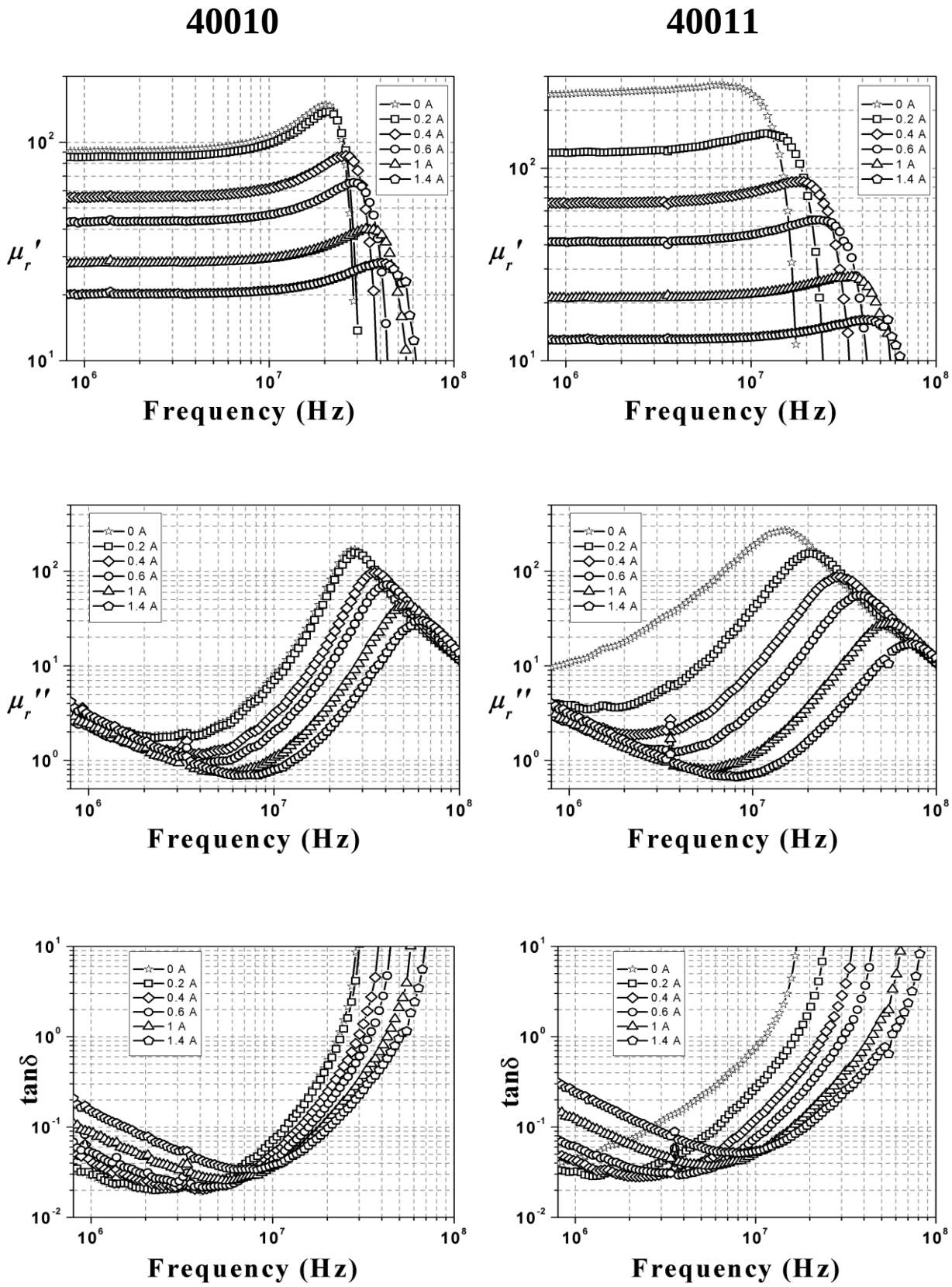

Figure 3-17: Magnetic characteristic for different amplitude of I_{DC} for commercial ferrites, I_{ACrms} =10mA

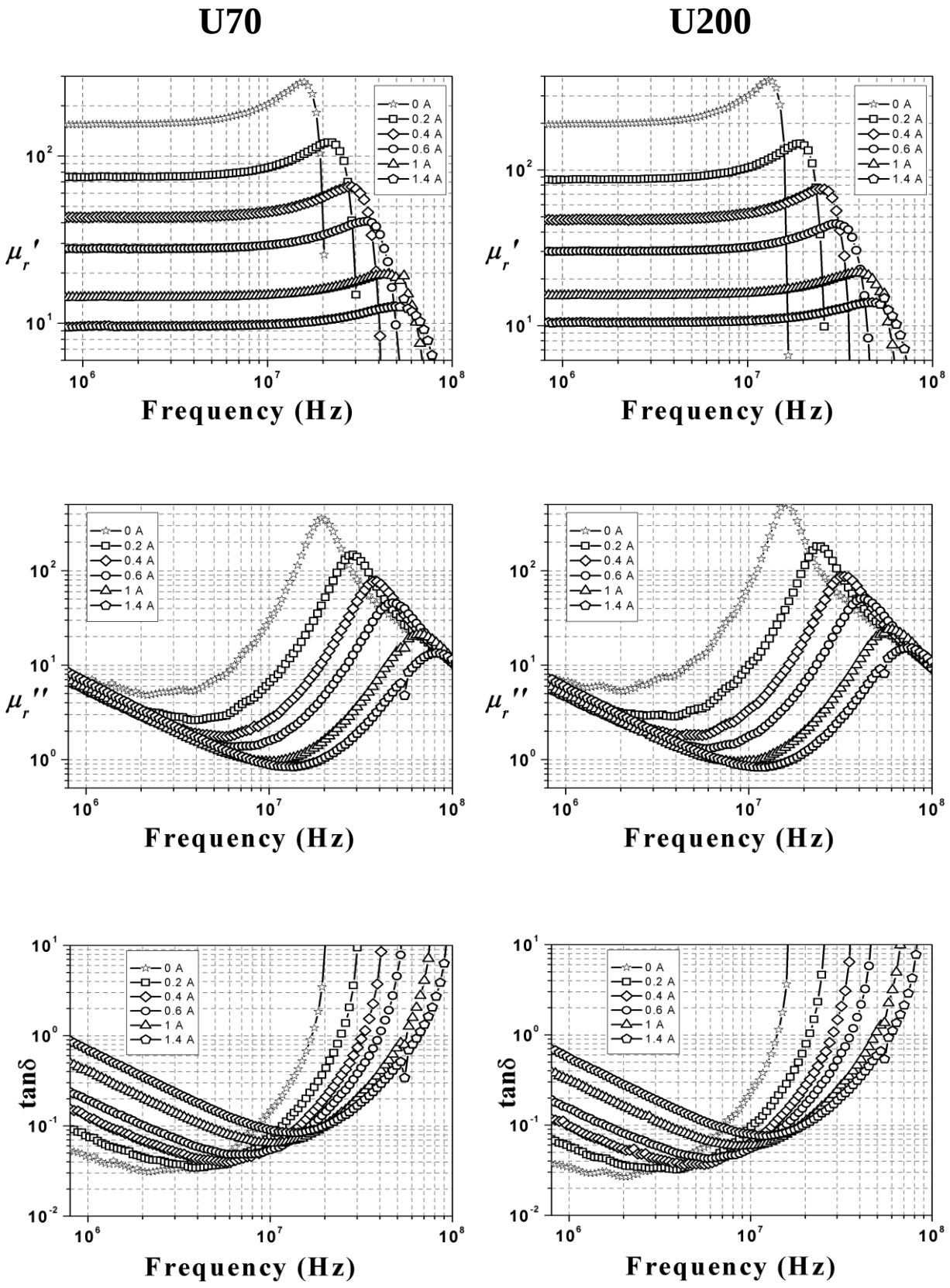

Figure 3-18: Magnetic characteristic for different amplitude of I_{DC} for in-house made ferrite, I_{ACrms} =10mA

5.4.2.2. Core losses as a function of pre-magnetized field H_{DC}

Continuous current I_{DC} causes a DC pre-magnetized field in the core, which shifts the minor alternating *B-H* loop on the *B-H* curve. This DC field may have an effect on the magnetic losses.

The losses are extracted for four ferrites at different DC bias current (from 0.2 A to 1.4 A). At certain I_{DC}, losses are characterized for different I_{AC} (from 1 mA to 20 mA). Similar curves and fitting like the ones in Figure 3-14 were produced. The losses models are given in Table 3-4. To express the magnetic losses versus pre-magnetized field, the DC magnetic field is referred from DC bias current. The extracted losses from measurement are given in Figure 3-19 together with the extrapolated losses curves from the losses models in Table 3-4.

Table 3-4: Values of parameters K, α and β obtained for four materials at different pre-magnetization DC field, apply for frequency 1-10 MHz and B_{AC} = 0.1-10mT

40011				**40010**			
H_{DC} **(A/m)**	***K***	α	β	H_{DC} **(A/m)**	***K***	α	β
0	5.84E-09	2.263	1.879	0	1.199E-09	2.356	1.969
260	2.159E-10	2.506	1.973	268	2.633E-09	2.324	1.985
518	1.301E-9	2.417	2.021	535	2.553E-09	2.339	1.991
777	1.272E-8	2.282	2	802	2.493E-08	2.206	1.984
1037	6.223E-08	2.205	2.014	1336	1.031E-08	2.302	2.006
1555	4.58E-06	2.023	2.068	1871	1.112E-08	2.326	1.999
2074	681.4E-06	1.825	2.12				

U200				**U70**			
H_{DC} **(A/m)**	***K***	α	β	H_{DC} **(A/m)**	***K***	α	β
0	2.457E-08	2.071	1.79	0	6.049E-10	2.345	1.869
244	4.936E-10	2.384	1.917	240	6.162E-10	2.361	1.88
488	9.72E-9	2.227	1.95	478	2.01E-08	2.19	1.939
732	4.913E-8	2.161	1.989	718	5.134E-08	2.16	1.96
1212	7.801E-7	2.015	1.972	1196	1.407E-3	1.608	2.024
1708	1.81E-6	1.984	1.959	1674	1.854	1.387	2.338

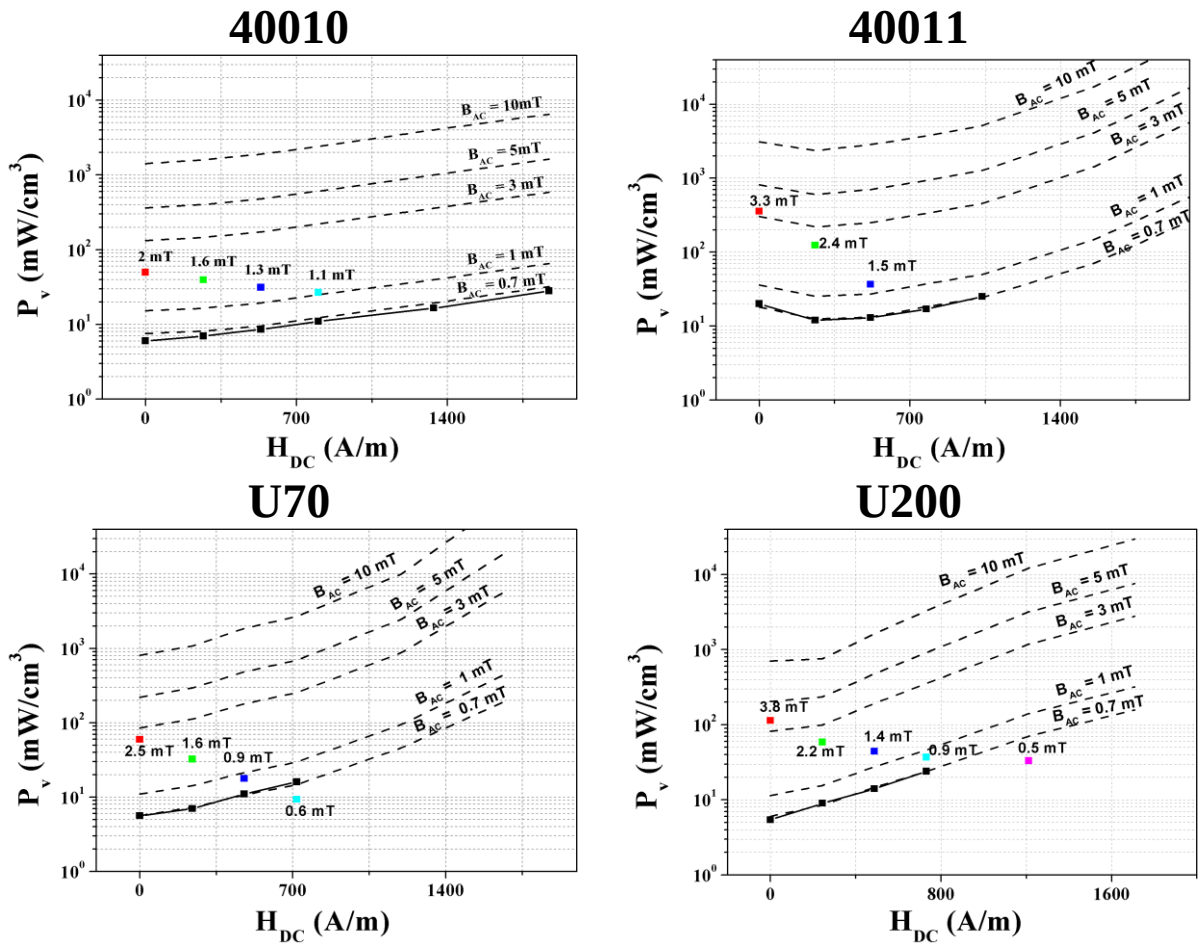

Figure 3-19: Core losses versus DC pre-magnetized field at 6 MHz; the curves are extrapolated from the loss models, the dots are extracted from measurements.

In Figure 3-19, the graphs show that the losses of ferrites increase with H_{DC} in general. At low value, however, for 40011, there is a drop of losses from 0 to 300 A/m. This phenomenon has been seen by Mu et al [8]. To give an example, at 0.6 A, corresponding to 700 – 800 A/m and 10 mT, expected losses for 40010, 40011, U70 and U200 are 2400, 3800, 2700 and 3100 mW.cm^{-3}.

5.4.3. Losses comparison and material selection

In order to compare performance of different magnetic materials, losses of four ferrites at three frequencies 1 MHz, 3 MHz and 6 MHz are given in the same graphs, see Figure 3-20. For the purpose of comparison, losses of commercial magnetic materials [15, 16] and losses from literature [17, 18] are also given. Losses of the four ferrites 40010, 40011, U70 and U200 are small at 1 MHz. At 1mT-10mT, losses are below 100mW.cm^{-3}. Losses shift to higher level for higher frequencies of 3 MHz and 6 MHz. At 6 MHz and 10mT, U200 has the lowest losses of 0.7W.cm^{-3} while 40011 has the highest losses of 2.5W.cm^{-3}. At 10 mT, U200 core presents the lowest losses from 4 MHz. U200 was chosen for the fabrication of final inductors thanks to its high permeability and low losses at the frequency of interest.

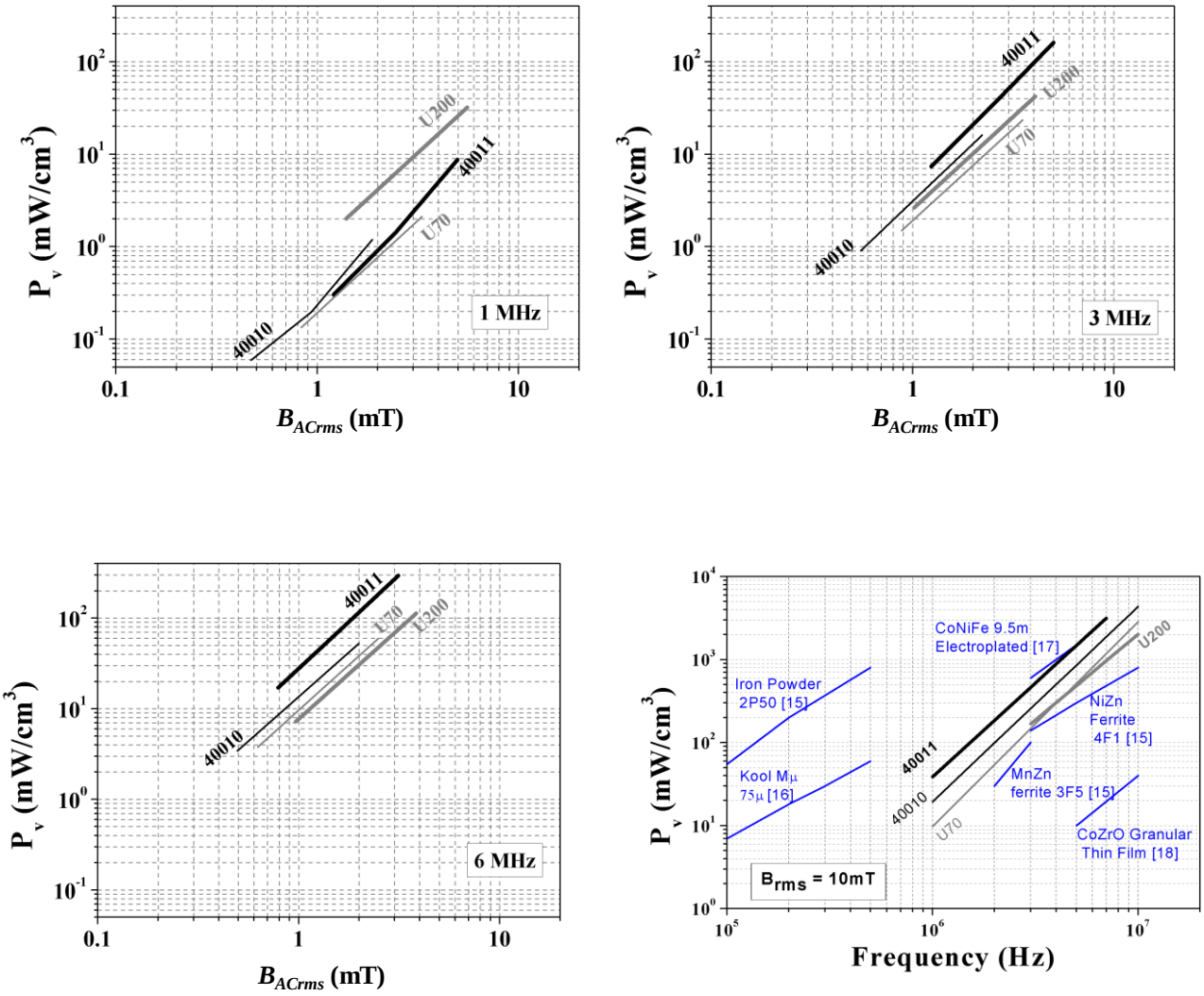

Figure 3-20: Losses comparison for different ferrites

Conclusions

To wrap up, magnetic properties of different ferrites were measured by magnetic material test fixture Agilent and impedance analyzer at different AC excitation current and different DC bias current. Permeability, inductance density and losses of the material were characterized under DC bias 0-1.4 A and different AC excitation current from 0 to 200 mA. However, the characterization is only performed at small sinusoidal AC signal when the DC bias current is applied. U200 with permeability of about 200 under zero DC bias and small AC current (10mA) with small losses (120 mW.cm^{-3} at 6 MHz and 4 mT) was chosen for the fabrication of final inductors. The measured values of permeability and losses, and losses model will be used for the next step of modeling and design optimization in FEMM and Matlab. At the moment, the core losses were characterized for the test inductor of tripled dimension (version x3). That takes the advantages of small winding resistance with triple bond-wire so that the influence of winding resistance on the measured core losses is limited i.e. the measured core losses are more precise. At the end, when the winding is fully realized with electroplated copper, the losses should be measured directly on the original x1 version of test inductors. For perspective, the

characterization of magnetic properties should be carried out at large AC excitation signal under DC bias current and with the real current wave-form i.e. triangular signal.

References

1. A. Globus, "Some physical considerations about domain-wall size theory of magnetization mechanisms", *Journal De Physique*, 38 1-15, 1977
2. A. Lucas, "Etude et mise au point de transformateurs large bande radiofréquence", *L'Ecole normale superieure de Cachan*, PhD thesis, 234, 2012.
3. O. F. Caltun, L. Spinu, and A. Stancu, "Magnetic properties of high frequency Ni-Zn ferrites doped with CuO", *IEEE Transactions on Magnetics*, 37 (4), 2353-2355, 2001
4. K. Emori, T. Shimizu, Y. Bizen, "Discussion on Design Optimization of Inductor Loss Focused on Copper Loss and Iron Loss", *2013 1st International Future Energy Electronics Conference (IFEEC 2013)*, 241-245, 2013
5. Y. Fukuda, T. Inoue, T. Mizoguchi, S. Yatabe, and Y. Tachi, "Planar inductor with ferrite layers for DC-DC converter", *IEEE Transactions on Magnetics*, 39 (4), 2003
6. D. H. Bang and J. Y. Park, "Ni-Zn Ferrite Screen Printed Power Inductors for Compact DC-DC Power Converter Applications", *IEEE Transactions on Magnetics*, 45 (6), 2762-2765, 2009
7. M. L. Wang, J. P. Li, K. D. T. Ngo, and H. K. Xie, "A Surface-Mountable Microfabricated Power Inductor in Silicon for Ultracompact Power Supplies", *IEEE Transactions on Power Electronics*, 26 (5), 1310-1315, 2011
8. M. Mu, Y. Su, Q. Li, F. C. Lee, "Magnetic Characterization of Low Temperature Co-fired Ceramic (LTCC) Ferrite Materials for High Frequency Power Converters", *2011 IEEE Energy Conversion Congress and Exposition (ECCE)*, 2011
9. W. Zhang, Y. Su, M. Mu, D. J. Gilham, Q. Li, and F. C. Lee, "High Density Integration of High Frequency High Current Point-of-Load (POL) Modules with Planar Inductors", *IEEE Transaction on Power Electronics*, PP (99), 2014
10. C. Xiao, G. Chen, and W. G. H. Odendaal, "Overview of power loss measurement techniques in power electronics systems", *IEEE Transactions on Industry Applications*, 43 (3), 657-664, 2007
11. R. Linkous, A. W. Kelley, and K. C. Armstrong, "An improved calorimeter for measuring the core loss of magnetic materials", *Applied Power Electronics Conference and Exposition, (APEC 2000)*, 2 633 - 639, 2000
12. M. Mu, Q. Li, D. Gilham, and F. C. Lee, "New core loss measurement method for high frequency magnetic materials", *Energy Conversion Congress and Exposition (ECCE 2010)*, 4384 - 4389, 2010
13. Y. Han, G. Cheung, A. Li, C. R. Sullivan, D. J. Perreault, "Evaluation of Magnetic Materials for Very High Frequency Power Applications", in *Power Electronics Specialists Conference (PESC 2008)*, Rhodes, Greece, 2008, 4270-4276
14. E. Wesseling, E. Brandon, and U. Lieneweg, "AC and DC Current Dependence of On-Chip Inductors", *IEEE Trans. Magn.*, 35 (3679), 1999
15. Online, "www.ferroxcube.com"
16. Online, "www.mag-inc.com"
17. S. Kelly, C. Collins, M. Duffy, F. M. F. Rhen, S. Roy, "Core materials for high frequency VRM inductors", in *38th IEEE Power Electronic Specialists Conference*, Orlando, FL, 2007, 1767-1772
18. W. D. Li, Y. Q. Sun, and C. R. Sullivan, "High-frequency resistivity of soft magnetic granular films", *IEEE Transactions on Magnetics*, 41 (10), 3283-3285, 2005

Chapter 4 Design optimization for integrated inductors

Introduction

Design optimization for integrated inductors has been the subject of numerous studies for last decades. Computer aided design and optimization for integrated on-chip inductors present a great interest for RF circuits and power converters designers. It allows the improvement in the fabrication of passive components in which inductors are the most critical. According to the application, the expected characteristics for micro-inductors results in a trade-off: high inductance or energy density, low losses, high current capability and high resonance frequency. The properties of inductor are determined by its geometrical and technological parameters. Basically, there are three major losses mechanisms: losses due to the winding resistance, core losses and losses due to the induced eddy current flowing in the substrate. Magnetic coupling to the substrate is practically eliminated by technically solutions with the substrate beneath the inductor [1], for example by inserting a patterned ground shield between the inductor and the substrate [2]. Losses due to the series resistance of the inductor can only be reduced by optimizing the geometrical parameters of the conductors.

The optimization technique searches for the optimal point by calculating an objective function repeatedly, moving from one candidate design point to the other. In power electronics design optimization, modeling usually comes down to one or a set of algebric, differential or integral equations. Designer should choose the accurate model for the optimization of their designs. The criteria for choosing models may be based on the nature of the objective function or the complexity of the models.

In this chapter, after reviewing the state-of-the-art on modeling and design optimization, we will present our approach to optimize the inductor's geometry. Results of the optimization are shown in the last part of the chapter.

1. State-of-the-art of inductor optimization

1.1. Problem definition of design optimization

The inductor optimization problem can be defined mathematically in a general form as:

Minimize $f_{(x)}$, $f_{(x)} \subseteq \Omega$

Subject to $g_{i(x)} \leq 0$, $i = 1 \ldots n$

Where $f_{(x)}$ is the objective function defined in the space Ω and $g_{i(x)}$ $i = 1 \ldots n$ are number of constraints. Objective function $f_{(x)}$ creates a mapping between design variables and design objective.

This mapping is created using models of inductors. The optimization problem is then solved using either a deterministic or stochastic method: deterministic methods like enumeration method [3], geometry programming method [4], space-mapping [5, 6] or sequential quadratic programming [7, 8]; stochastic methods like evolutionary algorithm [9, 10], particle swarm optimization [11, 12] and genetic algorithm [13-16]. These methods search for an optimal point by means of an iterative approach, involving calculation of the objective function one or more times for each iteration. There is usually a tradeoff between the accuracy of the model and the number of variables considered. Dynamics of the system are usually simplified in order to develop a reduced-order and faster way of modeling. A wide variety of techniques might be used in order to find a reduced-order model for the optimization. For example, the Steinmetz equation is derived from curve fitting to a data series given by test measurements of core losses. Dowell equation is derived from solving diffusion equation in one dimensional used for estimating winding losses. Some authors use physical model of an inductor like lumped physical model or equivalent circuit model [11]. Some others use two port model/inductor modeling for parameter extraction method [17].

A typical inductor design problem involves two steps: (i) to provide a model to compute the objectives as functions of optimization variables and the system parameters and (ii) the optimization phase: identify the combination that results in the highest quality factor at desired functional condition including frequency and/or current.

1.2. Literature review of inductor optimization

Various methods have been proposed for inductor design and optimization. They can be classified in two groups, deterministic methods and stochastic methods. In this section, each method will be reviewed basically with their pros and cons.

1.2.1. Deterministic methods

For deterministic type, there are several methodologies as follows:

- **Response surface methodology**

In 2004, Kenichi Okada described the inductor characteristics by response surface functions of scattering parameters (S-parameter) [18]. The response surface function is an equation involving physical layer-out parameters. It is usually polynomial of the structural parameter. The proposed model is constructed entirely in the S-parameter domain and independent of equivalent circuit models and geometry. Hence, this method can be applied to any type of inductor geometry. The value of each component in the equivalent circuit can be calculated from S-parameters. The analytical model expresses the quality factor Q in terms of component values L, R of the equivalent circuit. The inductor structure is optimized using the derived polynomial functions of S-parameters.

- **Enumeration method**

In 2007, Genemala used enumeration method for inductor optimization [3]. The boundaries on the design parameter with maximum and minimum values were decided for a design space of interest. Then, it discretizes the geometrical parameters within this area. The quality factor was computed for each combination of design parameters. The maximum quality factor is the optimum solution and its corresponding layout parameters are the optimum layout parameters and recommended for fabrication. This method is simple but inefficient, especially when the number of adjustable parameters becomes large because the time complexity of the enumeration method is exponential to the number of optimization variables. Such an approach can be viewed as a "trial-and-error" approach. Electromagnetic effects are neglected for simplifying inductor optimization. As a consequent, the resulting design can miss the critical high- frequency effects.

❖ **Geometric programming**

Geometric programming is another method to solve the inductor optimization problem [4]. It is a powerful mathematical programming method based on the assumption that both the objective function and the constraints are polynomial functions by extracting with approximate formula. The limitation of this method is that several high frequency effects like proximity effect, skin effect cannot be taken into account by the simple closed form formulas or polynomial functions. Electromagnetic effects are neglected for simplifying inductor optimization; consequently, the resulting design can miss the critical high- frequency effects. Another limitation is that this technique demands the coarse model in a specific format e.g. polynomial functions but the inductor may not always follow polynomial input-output relationships.

❖ **Sequential quadratic programming**

Sequential quadratic programming (SQP) is a method for optimizing the quality factor of integrated inductor [7] [8]. It is an iterative mathematical programming technique based on the observation that almost any smooth continuous function can be locally approximated by a quadratic function. SQP algorithm is at least an order of magnitude speedup compared to enumeration. SQP can be used with any physical model to optimize the device operating at any frequency, which makes it suitable to a broader range of applications.

❖ **Pareto optimization**

In 2011, 2013, Toke Andersen used finite element method (FEM) simulator to calculate the inductor parameter L, R_{DC}, R_{AC} from geometrical models and/or analytical model of racetrack inductor to predict the inductance, copper losses and core losses [19, 20]. Optimization procedure maps the calculated performances of a large number of different racetrack inductor designs to the η-α plane, where η is the efficiency and α the power density. The envelop resulting from the highest efficiency at each power density value in the η-α Pareto front is the outcome of the optimization procedure.

1.2.2. Stochastic methods

Stochastic methods for optimization are connected with random probability. There are several methodologies in this group as follows:

❖ **Evolutionary algorithm**

Evolutionary algorithm is a stochastic global optimization method. It operates through a simple cycle with four stages: (i) initialize population: The initial population is generated randomly over the search space, (ii) evaluate fitness: the fitness functions correlate with the constrained conditions, (iii) keep the best individual found: if one feasible solution is better than the best solution found, the best solution should be replaced with the new feasible solution, (iv) the procedure of evolutionary algorithm: according to the stochastic ranking scheme, the evaluated fitness and penalty functions for each individual are used to rank the individuals in a population, and the best individuals are selected for the next generation. Then, crossover and mutation are performed [9].

In 2010, Kota Watanabe used evolutionary algorithm for parameter and topology optimization of inductor [10]. The goal of optimization is to reduce the size of inductors satisfying the specifications on inductance values under weak and strong bias-current conditions. The inductance values are computed from the finite-element FE method. Immune algorithm and micro-genetic algorithm are used for optimization in which very small populations are used comparing to the conventional genetic algorithm.

❖ **Particle swarm optimization**

Particle swarm optimization (PSO) is a stochastic algorithm. In PSO method, the potential solutions are called particles and are flown through the design space by learning from the current best particle and its own experience. Particle swarm uses the implicit rules of bird flocks. The bird flocks move in a synchronized way without colliding each other. PSO uses the swarm intelligence method to solve the global optimization problem. PSO algorithm uses swarm of particles and each particle represents a potential solution. Each particle is represented by a position and a velocity vector. Like other evolutionary algorithm, PSO uses a fitness function to search for the best position. The fitness function is defined by the parameters to be optimized. At each run of simulation, the fitness function is evaluated by taking the position of the particle in the solution space. Each particle keeps track of its obtained highest value and the position of this value which is termed as the personal best. The location of the highest fitness value in a whole swarm is called global best. At each run there is only one global best and all the particles are attracted towards it. After each iteration the position and velocity of every particle is updated [11, 12].

In 2012, Daniel V. Harburg used particle swarm multi-object and Pareto front method for inductor optimization [21]. He presented two-dimensional AC winding loss model. The model considers skin effects, eddy currents and the unequal balance of the magnetic field within windings to determine over all AC losses in the conductor. The loss model is implemented in a multi-object optimization routine

to discover geometry and parameters that minimize losses and volume of inductor within a DC-DC converter. A particle swarm multi-objective optimization algorithm is employed to find designs that maximize inductor power density while minimizing losses of inductor in the converter. The Pareto front illustrates the overall best optimized designs.

❖ **Genetic algorithm**

Genetic algorithm (GA) is an evolutionary based global optimization technique which is efficiently used for inductor optimization. GA is a stochastic search method that mimics the natural biological evolution, operating on a population of potential solutions, applying the principle of survival of the fittest to produce better approximations to the optimized solution. Genetic algorithm is based on natural genetics, and is a particular class of evolutionary algorithm that uses technique inspired by evolution biology. Genetic operations including reproduction, crossover and mutation are used to guide a global search of a space for the solution. A genetic algorithm can search a complex space to explore a set of layer-out parameters for desired electrical performance. GA can be applied to any problem that can be formulated as an optimization function. As a result, they are applicable to non-linear problems, defined on discrete, continuous or mixed search spaces, constrained or unconstrained. The main advantage of GA is that they search a population of points in parallel instead of a single point; hence, making results less sensitive to the initial point chosen. GA is resistant to becoming trapped in local optima [13]. GA operates through a simple cycle: (i) the creation of a population of strings (ii) the evaluation of each string (iii) the selection of "most-fit" string and (iv) genetic manipulation to create a new population [14-16].

In 2004, Rana J Pratap combined neural network and genetic algorithm [14]. He presented a neural network based modeling scheme for inductor. A genetic algorithm based optimizer is coupled with the neural network model obtained for design and optimization of inductor. The basic components of the network are processing elements (neurons) and weights (connections). Genetic algorithm becomes efficient tools for non linear search and optimization. The neuro-genetic optimization approach has two stages. First, an accurate neural network model is developed. The neural network is coupled with genetic optimization in the next stage. The desired electrical characteristics are provided to the genetic optimizer, which starts with an initial population of layout parameters. It will compute the response of this population using the neural network model and selects the best samples and performs genetic manipulations to obtain results from the best samples.

In 2013, T Sato used strength Pareto evolutionary algorithm [22]. It can effectively find the Pareto solution sets without transforming multi-objective to single-objective problems. The real-coded genetic algorithm is employed [23]. In this optimization, the model is generated from the chromosome of each individual. In his work, the population size is set to 150. The optimization is performed over 200 generations. It takes about one week for an optimization with 200 generations when using a Xeon

processor (2.8 GHz). The resultant Pareto solutions show the optimized solutions. It is confirmed that all solutions satisfy the constraint conditions.

2. Introduction of inductor optimization in this work

In the previous part, we have reviewed the methodologies for inductor optimization proposed in the literature. In this section, the inductor optimization in our project will be introduced. This work was done in collaboration with Pierre Lefranc from G2Elab Grenoble [24]. So as to optimize the device, the first question is to choose a local or a global optimization method. As mentioned above, the deterministic methodologies are local optimization while the stochastic methodologies are global optimization. Global optimization gives the optimized solution in the whole range of interest. Depending on the complexity of the inductor that we want to design, global optimization often requires huge data calculation and need longer time to get the optimized solution. Our inductor has quite simple geometric design; so, to model the electromagnetic properties, we decided to choose the global optimization by genetic algorithm.

In our design optimization problem, with the selected ferrite from the previous part, the objective is to design the inductor geometrical shapes with the highest inductance and minimum losses including winding losses and core losses. Several constraints as inductance higher than 100 nH at frequency of 6 MHz and DC current of 0.6 A, the footprint being limited in the 3-6 mm^2 range must be considered. The constraint of dimension may be downgraded to 6 mm^2 in order to obtain the target specification of inductance. The inductor has a rectangular shape with windings in the two sides.

To compute losses and the inductance value from simulation, we use the Finite Element Method Magnetics (FEMM) tool. FEMM is a 2D finite element simulator, with fast computation, and can easily run with Matlab software (http://www.femm.info). From the material properties and geometric dimensions, we can compute the values of induction B and magnetic field H in the structure. The computation of core losses, R_{DC}, R_{AC} and inductance are deduced from B and H. The procedure for design optimization is summarized in Figure 4-1.

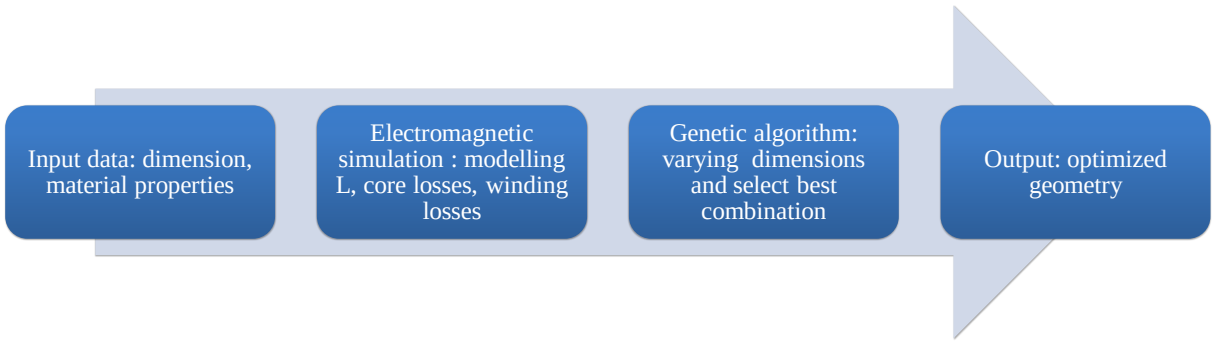

Figure 4-1 : Procedure for inductor design optimization

3. Input data for optimization

The design optimization tool needs the material properties of magnetic core and conductor, and also their dimension to evaluate the fitness functions like inductance *L*, and losses due to DC and AC resistance. The properties of copper conductor are taken from the material library while the magnetic properties of ferrite are obtained from the real characterizations as fully presented in chapter 3. Regarding the magnetic core, the design optimization tool takes the permeability and volumetric losses as input data. In the case of non-linear permeability, the non-linear dynamic *B-H* curve is required. This *B-H* curve is not the static one measured by vibrating sample magnetometer VSM as presented in chapter 3. Actually, the dynamic *B-H* curve can be obtained from the measurement curve of *L* vs. I_{DC}. The procedure for extraction is described in the following section.

3.1. Extrapolated dynamic B-H curve

The first design inductor was simulated by Maxwell Ansoft 3D with magneto-static solver. The magneto-static solver computes static (DC) magnetic field (*H*) generated by the DC current in conductors. The current density and magnetic flux density (*B*) are automatically calculated from the magnetic field. Derived quantities such as energy and inductances can be calculated from these basic field quantities. For magneto-static solver, material permeability can be non-linear or anisotropic. The applied boundary condition is default i.e. the magnetic field is tangential to the boundary and flux cannot cross it. The mesh operation is done with adaptive mesh solution.

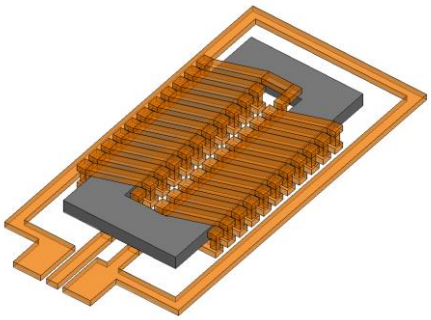

Figure 4-2: Model of micro-inductor simulated in Maxwell Ansoft 3D

Based on the experimental curve of *L* as a function of I_{DC}, the simulation was done at each measured point i.e each point of (L_i, I_{DCi}) i=1…n. The permeability of the magnetic core is μ_i corresponding to the point (L_i, I_{DCi}) and the combination (B_i, H_i) is recorded for each measured point. The combination of all the points (B_i, H_i) i=1…n can be considered as raw non-linear *B-H* curve (see Figure 4-3).

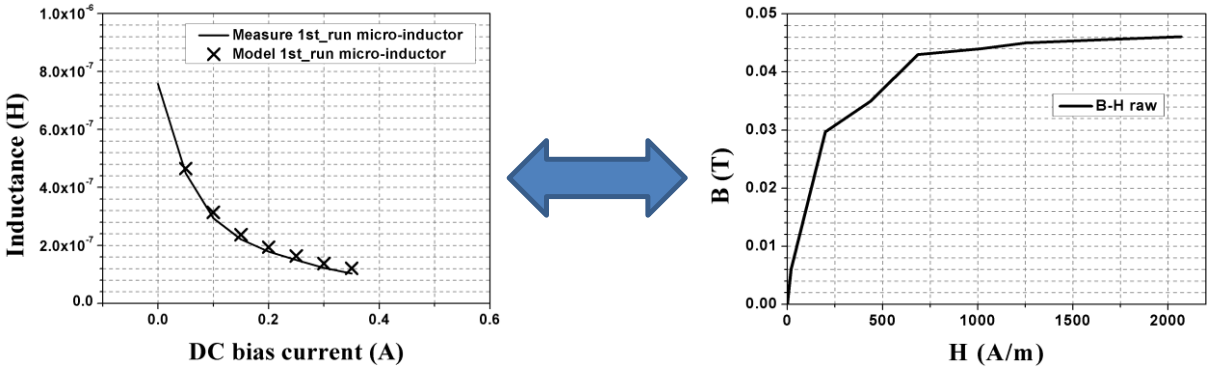

Figure 4-3 : Raw non-linear B-H curve extracted from the measured curve of L vs. I_{DC}

In order to get a fine non-linear *B-H* curve for a better modeling in the next step, another simulation was carried out. The raw non-linear *B-H* curve is fed in for the non-linear permeability. After the run of Maxwell magneto-static solver, the extrapolated non-linear *B-H* curve is exported and we save this *B-H* curve for the upcoming modeling and simulation in the design optimization (see Figure 4-4). The simulation of electromagnetic behaviors will be more accurate with this new *B-H* curve.

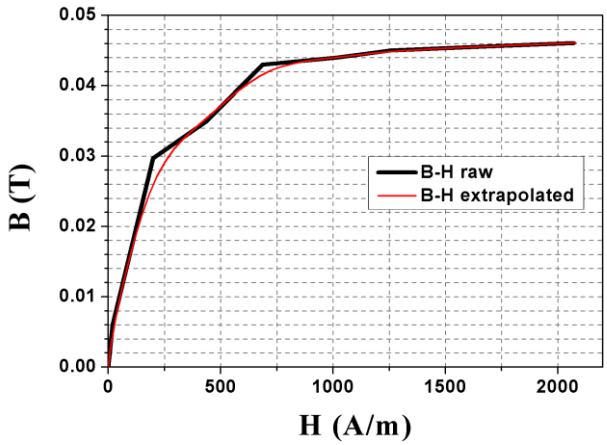

Figure 4-4 : Extrapolated non-linear B-H curve extracted from Maxwell Ansoft 3D solution

3.2. Analytical losses model

As presented in chapter 3, the losses of ferrite core were extracted from impedance measurements of the ferrite-based micro-inductor. The Steinmetz formula was used to fit the core losses with analytical models which will be used straight away in the simulation tool. The losses models were generated for different DC pre-magnetized field as listed in the table. For the present, the inductor model doesn't include the contribution of H_{DC}.

Table 4-1 : Analytical loss models of ferrite core

H_{DC} (A/m)	K	α	β
H_{DC}<244	2.457E-8	2.071	1.79
244< H_{DC}<488	4.936E-10	2.384	1.917
488< H_{DC}<732	9.72E-9	2.227	1.95
732< H_{DC}<1212	4.913E-8	2.161	1.989
1212< H_{DC}<1708	7.801E-7	2.015	1.972
H_{DC} >1708	1.81E-6	1.984	1.959

4. Electromagnetic model of micro-inductor

In this part, we will present the model to simulate the electromagnetic behavior of inductor in FEMM: we will begin with the geometry construction and assign the material properties and then specify the mesh generation to finally simulate by finite elements.

4.1. Geometric construction

With some known variables like number of turns N, geometrical dimensions, material properties and the excitation current, the electromagnetic model in FEMM is built as shown in Figure 4-5. The electromagnetic model in FEMM is 2D, the 3D essence of inductor will be compensated by the depth of the model; the thickness of the core was considered as the profound of the model. Different materials are assigned for corresponding blocks of the model. All this construction was coded in Matlab. With specified materials of coil and core, we calculated the skin depth of the core and conductor. The skin depth of copper is about 27 µm at frequency of 6 MHz. Based on the length and width of core, we created the mesh with the mesh element dimension smaller than the skin depth of copper conductor. One can note that we only simulate the winding losses in FEMM, the core losses are calculated from simulated result with the help of a post-processing step.

We have to simulate DC and AC behaviors. In the DC simulation, the current excitation is DC. Non-linear *B-H* curve is used. This simulation gives the value of inductance L according to I_{DC} to insure the constraint of inductance >= 100nH at the specified condition I_{DC} = 0.6 A. To estimate AC losses in the winding and in the core, we perform an AC simulation running at 6 MHz with a 20 mA AC current. That is the objective of the function of optimization.

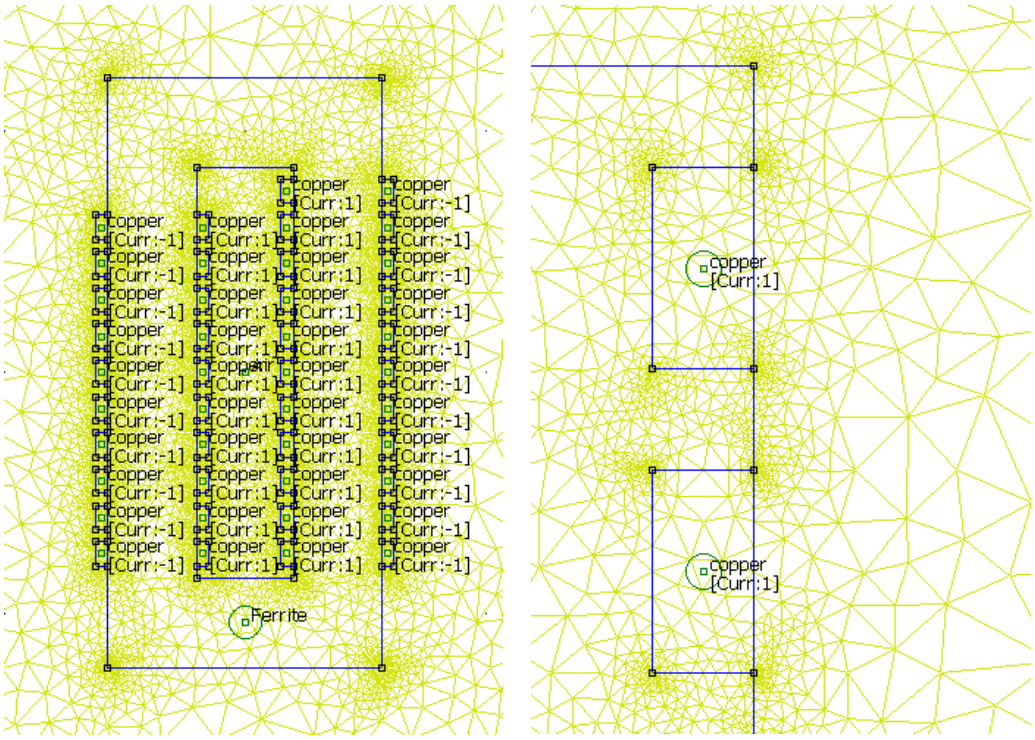

Figure 4-5: FEMM inductor model with mesh a) full view, b) zoom on copper tracks

4.2. Post-simulation data processing

The FEMM simulation calculates the *B-H* values of all mesh points and parameters like magnetic energy, winding losses. The others parameters like inductance value and core losses have to be calculated from values of *B-H* obtained by simulation for each mesh point. Figure 4-6 shows the magnetic field distribution inside the magnetic core with the excitation of 0.6 A (DC). The magnetic induction is in the range 0.002 – 0.04 T.

To calculate the value of inductance as a function of DC current, we set to zero the frequency of the solution in the DC simulation. As FEMM gives the magnetic flux in the inductor, the inductance can be calculated from the following expression:

$$L_{flux} = \frac{\phi_{total}}{I_{DC}} = \frac{N\phi_{core}}{I_{DC}} \qquad \textit{(Eq. 4.1)}$$

The inductance can be calculated by other method based on the magnetic energy by the following equation:

$$L_{energy} = \frac{2W_{magnetic}}{I_{DC}^2} \qquad \textit{(Eq. 4.2)}$$

In order to verify the two methods, we have simulated a real inductor (the 1st run inductor with U200). The inductance calculated by two above methods are compared with the measured values. That gives a relatively good accuracy (see Figure 4-7). At the moment, the different results obtained from two

methods can't be explained clearly. The result is better with flux method than energy method. Therefore, flux method is selected for optimization.

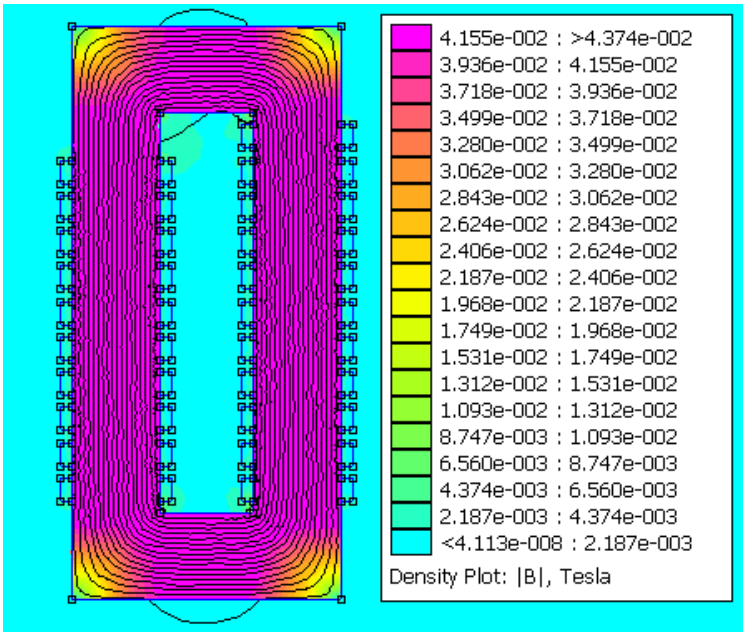

Figure 4-6: Magnetic field (DC simulation, I_{DC}=0.6A, 1st run inductor with U200)

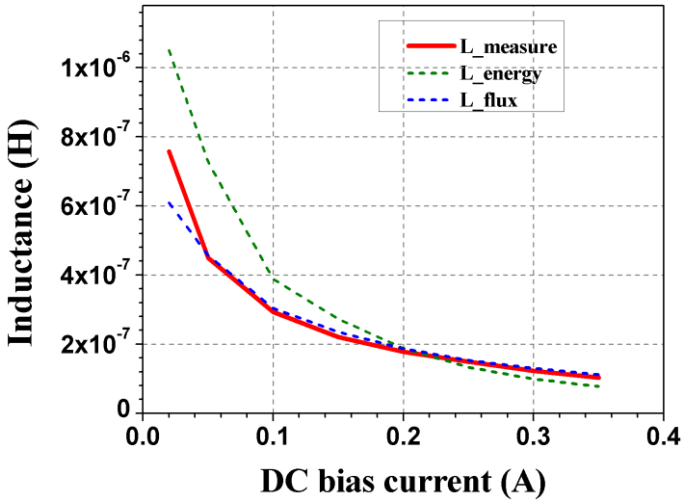

Figure 4-7: Inductance as function of DC current simulated by two methods vs. measurements

In our AC simulation model, there are no losses in the core and the total simulated losses are corresponding to winding losses. We can represent them by an AC resistance using the following expression:

$$R_{AC} = \frac{P_{winding}}{I_{AC\_rms}^2} \qquad \textit{(Eq. 4.3)}$$

The current density in the conductor and the magnetic field distribution in the magnetic core are shown in Figure 4-8 and Figure 4-9 for the excitation of 20 mA (AC) at 6 MHz. The skin and proximity effect may be observed in Figure 4-8. The magnetic induction is in the range 0.001–0.012 T.

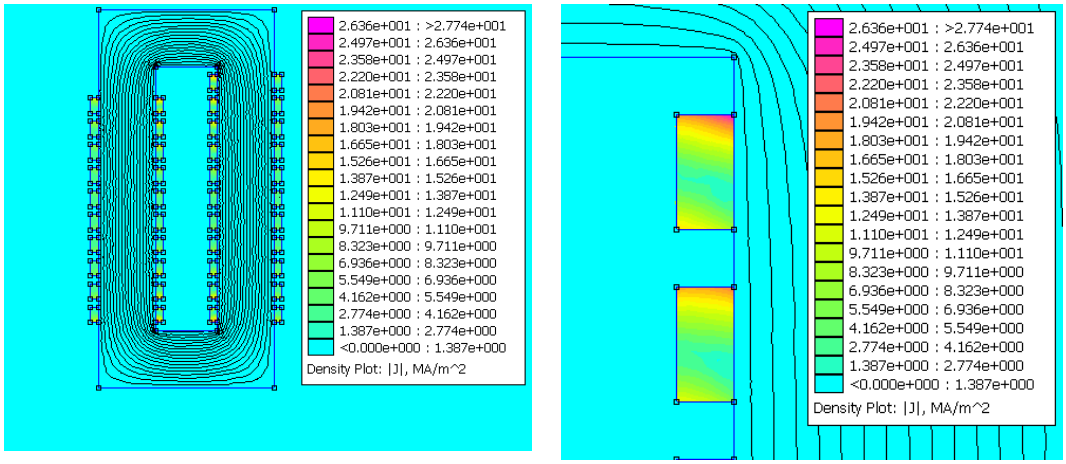

Figure 4-8: Current density in the winding (AC simulation, 6 MHz, I_{AC} = 20mA)

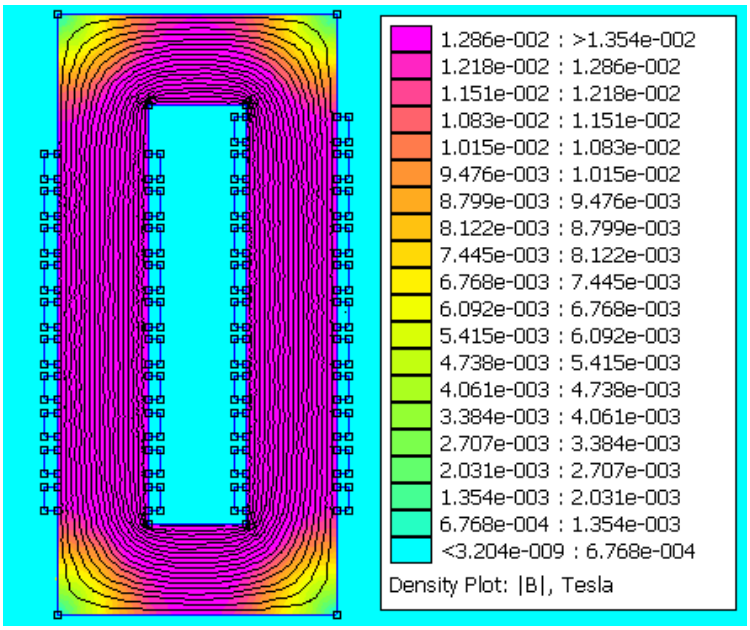

Figure 4-9: Magnetic field (AC simulation, 6 MHz, I_{AC} = 20mA)

The next step is to evaluate the core loss. It can be calculated by analytical loss model that we obtained in the previous parts with Steinmetz equation.

The following expression is used to calculate the core losses, in which f is frequency, B_{ACrms} is the induction inside the core, V is the volume of the core, K, α and β are coefficients of the Steinmetz equation.

$$P_{core} = K f^{\alpha} \int_{core} {B_{ACrms}}^{\beta} dV \qquad \textit{(Eq. 4.4)}$$

5. Optimization by genetic algorithm and results

The genetic algorithm is used to solve the optimization problem in this work. At the first stage, an initial population is randomly generated. Each element of the population, called individual, is encoded into string to be manipulated by genetic operator. In the next stage, the performance or fitness of each individual of the population is evaluated. A selection mechanism chooses "mates" for the genetic manipulation. The selection policy is to assure the survival of the most "fit" individual. Genetic operators including reproduction, crossover and mutation are respectively used to create a new population of "offspring" by manipulating the genetic code of members of the current population. Reproduction is the process by which string with high fitness values are selected to have large number of copies in the new population. After reproduction, the survived elements are stored for mutation and crossover operations. The crossover operation takes two parents and interchange part of their genetic code to produce new elements. The mutation operation is implemented by randomly changing a fixed number of bits every generation based on a specific mutation probability. The mutation operation is needed to account for the possibility that initial population may not contain all the genetic information needed to solve the problem. The genetic algorithm in steps is presented Figure 4-10.

In this inductor optimization, the genetic algorithm parameters are as followed:

- Number of individuals in population: *nb_ind = 30*
- Mutation coefficient: *nb_mut = 10*
- Number of iterations: *imax = 30*

The objective function in this optimization problem is the losses minimization including core and copper losses, with the main constraint $L \geq 100$nH and others like core width 0.9 mm $\leq X \leq$ 2 mm, number of turns $10 \leq N \leq 30$, conductor thickness 30 µm $\leq t_c \leq$ 80 µm and conductor width 50 µm $\leq W_c \leq$ 120 µm . The total time of the optimization process is 48 hours. The evolution of the total losses is obvious through twenty generations of offspring (see Figure 4-11). Results are given in

Table ***4-2***. It is not possible to reach the target specification in the footprint of 3 mm^2 (an inductance higher than 100 nH at 0.6 A DC bias and 6 MHz). To obtain these specifications, the optimized solution of 6 mm^2 was determined.

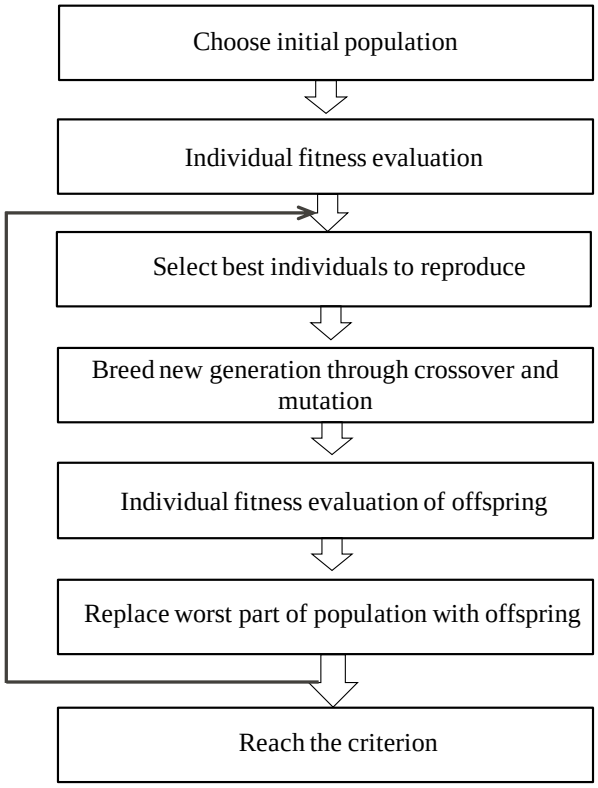

Figure 4-10 : Flow chart of genetic algorithm [15]

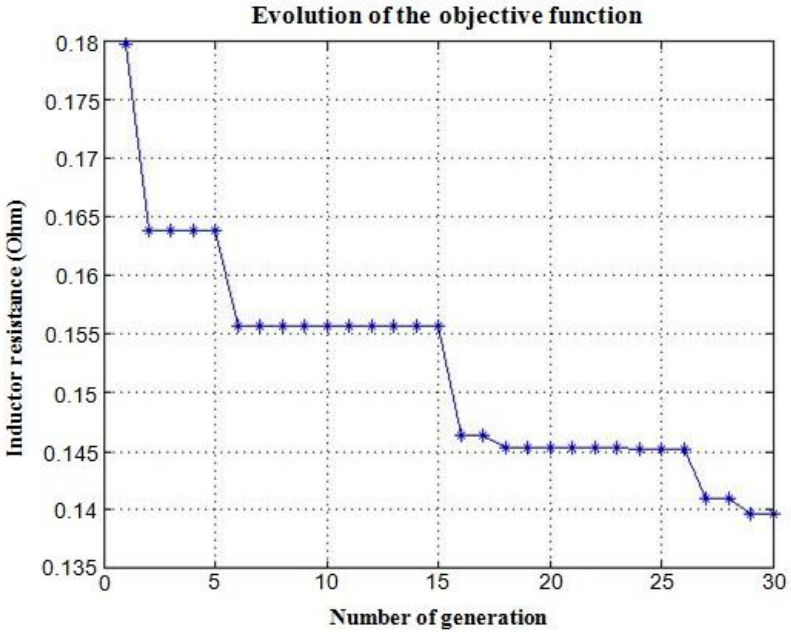

Figure 4-11 : Evolution of the objective function as a function of number of generation

Table 4-2 : Optimization result for our micro-inductor

Parameter	First run (not optimized)	Second run (optimized)
Number of turns *N*	21	27
Length *Y* (mm)	2.6	3.6
Width *X* (mm)	1.14	1.7
Depth *H* (mm)	0.11	0.11
Footprint (mm^2)	3	6
Magnetic core width *Wmag* (mm)	0.43	0.65
Conductor thickness t_c (µm)	50	55
Conductor width W_c (µm)	100	105

Parameter	First run (not optimized)		Second run (optimized)	
	Measure	Calculation	Measure	Calculation
Inductance at 0.6A DC (nH) (6MHz, 20mA AC)	38	35	107	105
DC resistance (mΩ)	-	93	-	140
AC resistance at 6MHz (mΩ)	-	128	-	180
Core losses (mW) at zero DC bias, 20 mA AC, 6 MHz	0.033(101 $mW.cm^{-3}$)	0.012 (37 $mW.cm^{-3}$)	0.067 (99 $mW.cm^{-3}$)	0.033 (49 $mW.cm^{-3}$)
Energy density ($nJ.mm^{-3}$)	-	21.0	-	28.6
Quality factor ($2\pi f L/R_{AC}$)	-	11	-	22

The test inductors of the 1st and 2nd design were realized with the electroplated bottom copper tracks and the top windings as gold bond-wire (see Figure 4-12). Both test inductors were characterized for inductance values and losses. The inductances as a function of DC bias current and frequency are shown in Figure 4-13 and Figure 4-14.

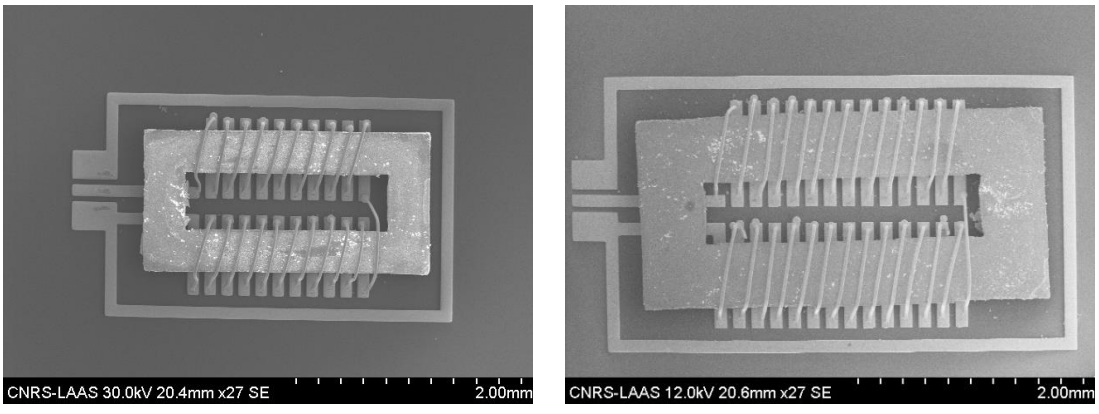

Figure 4-12 : SEM images of the 1st run and 2nd run test micro-inductor

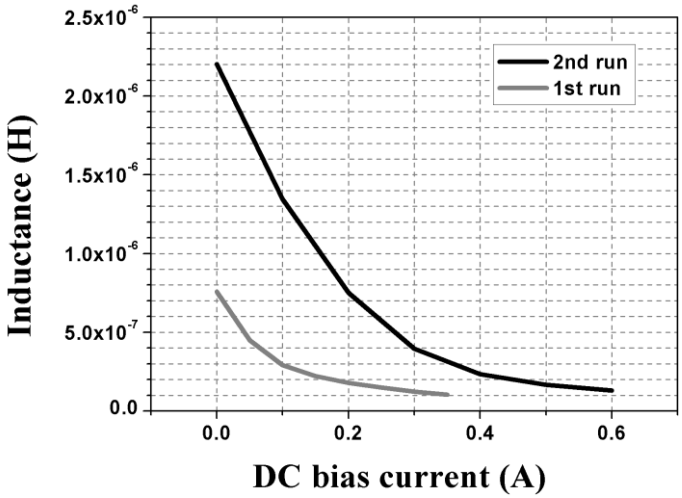

Figure 4-13 : Measured inductance versus DC bias current for the 1st and 2nd run

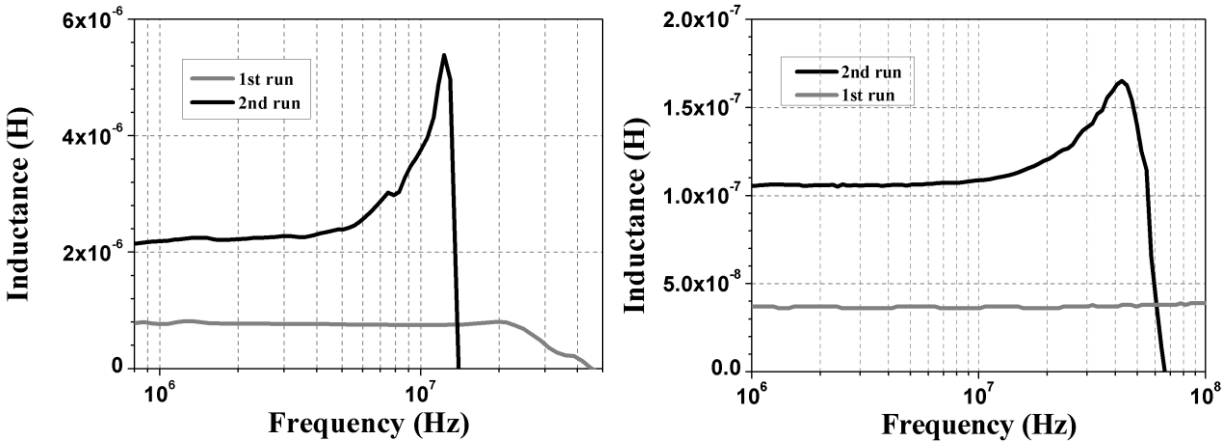

Figure 4-14 : Measured inductance versus frequency at zero DC bias (left) and 0.6 A DC bias (right), with I_{AC} = 20 mA, for the 1st and 2nd run

The curves in Figure 4-14 show an improvement of the inductance value for the 2nd run. At 0.6 DC bias, the value of inductance for the 2nd run test inductor is about 107 nH stable up to 10 MHz and satisfies the optimization criteria. The optimization has proved better performance and leads to an increase of the energy density (×1.4) and of the quality factor (×2). However, the decrease of the resonance frequency is probably due to higher parasitic capacitance for the 2nd run because of thicker, wider and longer copper tracks. This point is a key issue for future designs and optimization tool. The measured core losses at 6 MHz with zero DC current bias and 20 mA AC current (see Table 4-2) are much higher than the core losses calculated by the design optimization tool at the same condition. The measurement method of core losses is not fully accurate because the differences between air-core inductors and magnetic core inductors may result in errors in the analytical losses model fit with Steinmetz equation. We may need a better analytical losses model in order to have an accurate simulation tool for core losses. The air-core inductors are maybe not the best way to remove the contribution of copper: finite elements (FE) simulation with an infinite resistivity for the core material could give more accurate results. However, in this particular case, the AC winding losses are much higher than the core losses, so that it doesn't affect the result of the optimization process. The AC

winding losses are more important in optimization calculation. The DC and AC resistance couldn't be measured for comparison because the final top copper and via haven't been accomplished yet.

Conclusion

The inductor design optimization problem was studied and we have proposed a design methodology based on genetic algorithm. The micro-inductor was simulated with finite element methods using FEMM to compute its electromagnetic properties and the optimization process runs on a Matlab software. The design optimization tool was successful to offer a solution which satisfied all the constraints of inductance value and dimensions. The overall method needs to be improved to reduce errors in calculation of core losses. In perspective, the top copper tracks and via need to be finished with electro-deposition so that DC and AC resistances can be measured for the final micro-inductor. The issue of final micro-inductor realization with electroplated copper winding will be presented in the next chapter.

References

1. J. Y. C. Chang, A. A. Abidi, and M. Gaitan, "Large suspended inductors on silicon and their use in a 2-mu-m cmos rf amplifier", *IEEE Electron Device Letters*, 14 (5), 246-248, 1993
2. C. P. Yue and S. S. Wong, "On-chip spiral inductors with patterned ground shields for Si-based RF ICs", *IEEE Journal of Solid-State Circuits*, 33 (5), 743 - 752, 1998
3. G. Haobijam and R. Paily, "Efficient optimization of integrated spiral inductor with bounding of layout design parameters", *Analog Integrated Circuits and Signal Processing*, 51 (3), 131-140, 2007
4. M. Del Mar Hershenson, S. S. Mohan, S. P. Boyd, and T. H. Lee, "Optimization of inductor circuits via geometric programming", *IEEE Design Automation Conference*, New Orleans, 994 - 998, 21-25 June 1999
5. J. W. Bandler, R. M. Biernacki, S. H. Chen, P. A. Grobelny, and R. H. Hemmers, "Space mapping technique for electromagnetic optimization", *IEEE Transactions on Microwave Theory and Techniques*, 42 (12), 2536-2544, 1994
6. W. Yu, J. W. Bandler, "Optimization of spiral inductor on silicon using space mapping", *2006 IEEE Mtt-S International Microwave Symposium Digest, Vols 1-5*, 1085-1088, 2006
7. Y. Zhan and S. S. Sapatnekar, "Optimization of integrated spiral inductors using sequential quadratic programming", *Design, Automation and Test in Europe Conference and Exhibition, Vols 1 and 2, Proceedings*, 622-627, 2004
8. T. B. Chan, H.-C. Lu, J.-K. Zeng, C. C.-P. Chen, "LTCC spiral inductor modeling, synthesis, and optimization", in *Asia and South Pacific Design Automation Conference*, Seoul, South Korea, 2008, 744-747
9. D. He, L. Sun, and J. Liu, "Application of domain decomposition method and improved evolutionary algorithm in optimization of spiral inductors on silicon", *Wireless, Mobile and Multimedia Networks Conference (IET 2006)*, 1 - 3, 6-9 Nov. 2006
10. K. Watanabe, F. Campelo, Y. Iijima, K. Kawano, T. Matsuo, T. Mifune, and H. Igarashi, "Optimization of Inductors Using Evolutionary Algorithms and Its Experimental Validation", *IEEE Transactions on Magnetics*, 46 (8), 3393-3396, 2010
11. Y. Guo and Q. Cao, "Analysis and design of spiral inductor based on the particle swarm optimization algorithm", *Microwave and Millimeter Wave Technology Conference (ICMMT 2010)*, 734 - 736, 8-11 May 2010

12. S. K. Mandal, A. Goyel, A. Gupta, "Swarm Optimization Based On-Chip Inductor Optimization", *2009 4th International Conference on Computers and Devices for Communication (CODEC 2009)*, 152-155, 2009
13. E. D. Gadjeva, V. P. Durev, M. H. Hristov, and D. I. Pukneva, "Optimization of geometric parameters of spiral inductors using genetic algorithms", *Proceedings of the International Conference Mixed Design of Integrated Circuits and Systems*, 514-517, 2006
14. R. J. Pratap, S. Sarkar, S. Pinel, J. Laskar, G. S. May, "Modeling and optimization of multilayer LTCC inductors for RF/wireless applications using neural network and genetic algorithms", in *Electronic Components and Technology Conference 2004*, Las Vegas, NV, 2004, 248-254
15. T. Fan, X. Wen, and P. Ning, "Genetic algorithm based high inductance density low-profile inductor optimization", *Energy Conversion Congress and Exposition (ECCE)*, 3687 - 3692, 15-19 Sept. 2013
16. P. Pereira, M. H. Fino, F. Coito, and M. Ventim-Neves, "RF integrated inductor modeling and its application to optimization-based design", *Analog Integrated Circuits and Signal Processing*, 73 (1), 47-55, 2012
17. N. Arbabi, M. Najmabadi, V. Devabhaktuni, M. Yagoub, "A new SQP based space-mapping algorithm for on-chip spiral inductor optimization", in *20th Annual Canadian Conference on Electrical and Computer Engineering*, Vancouver, Canada, 2007, 99-102
18. K. Okada, H. Hoshino, H. Onodera, "Modeling and optimization of on-chip spiral inductor in S-parameter domain", *2004 IEEE International Symposium on Circuits and Systems, Vol 5, Proceedings*, 153-156, 2004
19. T. M. Andersen, C. M. Zingerli, F. Krismer, J. W. Kolar, C. O'mathuna, "Inductor Optimization Procedure for Power Supply in Package and Power Supply on Chip", *2011 IEEE Energy Conversion Congress and Exposition (ECCE)*, 1320-1327, 2011
20. T. M. Andersen, C. M. Zingerli, F. Krismer, J. W. Kolar, N. Wang, and C. O. Mathuna, "Modeling and Pareto Optimization of Microfabricated Inductors for Power Supply on Chip", *IEEE Transactions on Power Electronics*, 28 (9), 4422-4430, 2013
21. D. V. Harburg, J. Qiu, and C. R. Sullivan, "An improved AC loss model for the optimization of planar-coil inductors", *Control and Modeling for Power Electronics Workshop (COMPEL 2012)*, 1 - 7, 10-13 June 2012
22. T. Sato, K. Watanabe, H. Igarashi, T. Matsuo, T. Mifune, K. Kawano, M. Suzuki, Y. Uehara, and A. Furuya, "3-D Optimization of Ferrite Inductor Considering Hysteresis Loss", *IEEE Transactions on Magnetics*, 49 (5), 2129-2132, 2013
23. F. Herrera, M. Lozano, and J. L. Verdegay, "Tackling real-coded genetic algorithms: Operators and tools for behavioural analysis", *Artificial Intelligence Review*, 12 (4), 265-319, 1998
24. P. Lefranc, X. Jannot, and P. Dessante, "Virtual prototyping and pre-sizing methodology for buck DC-DC converters using genetic algorithms", *IET Power Electronics*, 5 (1), 41-52, 2012

Chapter 5 Integrated inductor realization

In the previous chapters, the test inductors were realized and characterized to extract the magnetic properties of soft ferrite cores, and then the design of the micro-inductor was optimized. This chapter will present the experimental approaches and technological process in order to realize the final micro-inductor.

1. Proposed experimental approaches

The objective of experiments is to develop a technology for fabricating integrated micro-inductors on/in silicon based on ferrite as magnetic cores. Two experimental approaches are proposed: monolithic integration and hybrid integration. In both cases, copper is chosen for the winding as top tracks, bottom tracks and vias. Electro-deposition technology is used for copper deposition. Copper via is also electroplated to connect different levels of Cu wires to form close windings (see the schematic in Figure 2-5).

The first strategy for fabrication is screen printing the ferrite paste inside cavities in silicon wafer and sintering them with Cu tracks underneath: this is monolithic integration. The second strategy is pick-and-place technique in which, the ferrite core is fabricated and sintered individually and then placed on Cu wires. That is hybrid integration. The feasibility of each proposed methods will be evaluated by testing and developing critical process steps. In final micro-devices, it is envisaged either to bond the two levels of windings by flip chip with the core in between or to finish copper windings with photo-resist mold technology. These technologies and possible alternative solutions are discussed in this chapter. At the end, the most feasible technology will be used for final fabrication of the micro-inductor.

1.1. Monolithic integration

In this approach, the micro-inductor will be embedded into silicon wafer via a cavity. The envisaged steps of fabrication are shown in Figure 5-1. The cavity is created by KOH etching. Then, the bottom copper is deposited and the ferrite paste will be printed into the cavity to create cores by screen-printing technique. The top Cu tracks are either electroplated in a different wafer and joined by flip-chip technique, as shown in the schematics, or directly electroplated onto planarized ferrite cores. The advantage is that all steps are done with micro-fabrication which allows large-scale fabrication. Moreover, this integration saves the space by integrating the micro-inductor into the silicon substrate. The disadvantage is that high sintering temperature may be a problem of inter-diffusion and not CMOS compatible. In the case of the two wafers assembled by flip-chip bonding, through silicon vias (TSV) might be needed in order to reach the inductor's connection pads and these TSVs are sometimes already fabricated for other components on the board.

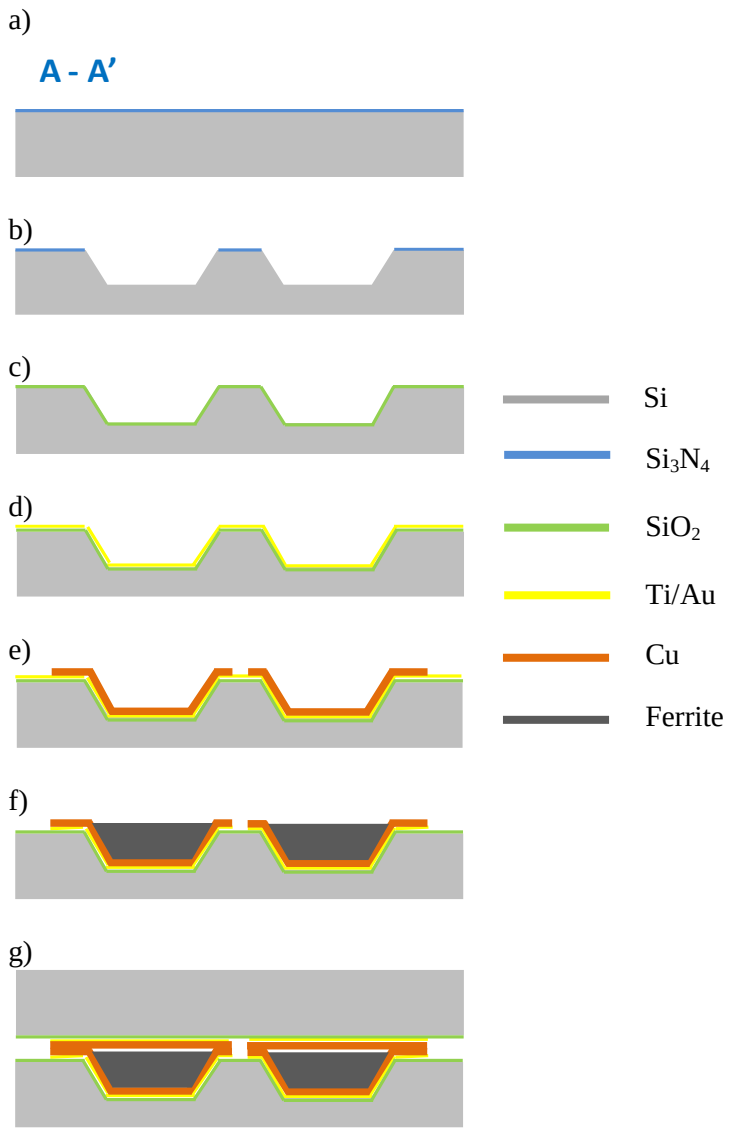

Figure 5-1 : Schematic of inductor fabrication steps in monolithic integration approach a) Deposition of Si_3N_4 on Si wafer b) Photolithography and KOH etching to create cavities c) Remove Si_3N_4 and deposit an insulation layer of SiO_2 d) Sputtering of a seed layer Ti/Au on the wafer e) Deposition of bottom copper tracks by electro-deposition and photolithography f) Screen printing of ferrite paste inside the mold and co-sintering g) Flip-chip to bond the top copper track wafer to the bottom one.

1.2. Hybrid integration

For hybrid integration, the ferrite cores are made separately by cutting from commercial ferrite film or printed by screen printing, then fully sintered. The bottom copper tracks are electroplated in silicon wafer and then planarized by a layer of SU8 photoresist. Then, the core is stuck on bottom copper tracks. The conductor windings can be completed by flip-chip bonding of two wafers with copper tracks or can be completed by the vias and top copper tracks electro-deposited by thick photoresist mold technology with BPN® photoresist [1]. The estimated fabrication steps are given in Figure 5-2 for the case using thick photo-resist mold technology to complete windings.

The advantage of this approach is that the number of fabrication steps is minimized. The disadvantage is that it is necessary to stick the cores by pick-and-place method. At the moment, in this work, this step can only be done manually. For an efficient transfer into an industrial manufacturing process, it requires efforts to make it automatic, fast and reliable (with high yield).

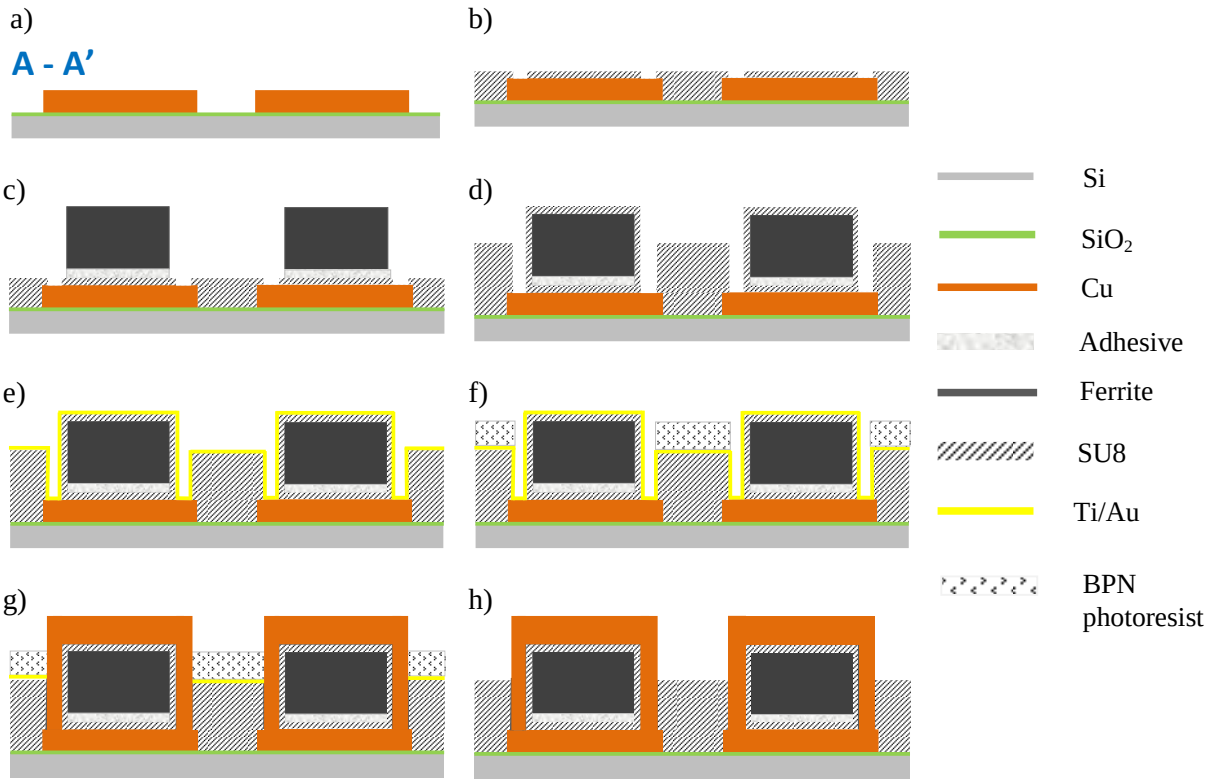

Figure 5-2 : Schematic of inductor fabrication steps in hybrid integration approach a) Electroplating of bottom Cu tracks on Si/SiO_2 wafer b) Planarization of Cu tracks and open vias c) Adjunction of thin film ferrite core on Cu tracks with photo-sensitive glue d) Covering of ferrite cores with SU8 and open vias e) Sputtering of a seed layer Ti/Au on the wafer f) Photolithography of BPN molds for vias and top Cu tracks g) Electroplating of top Cu tracks and vias h) Removal of BPN residues and Ti/Au seed layer

The tests and developed processes for realizing the monolithic and hybrid integration will be fully presented in the next section.

2. Process development for monolithic approach

Processes and technology were developed in the clean room at LAAS to realize the monolithic integration including the process of etching cavity in silicon wafer and the tests of co-sintering printed ferrites with the silicon wafer.

2.1. KOH etching and compensation for rectangular cavity

The idea to fabricate magnetic core in the first strategy is to print ferrite slurry inside the cavity in the silicon wafer where copper tracks are preliminary deposited and then sinter them. Regarding the

design, the shape of ferrite core is rectangular with a hole in the middle and hence, the rectangular cavities need to be created in the silicon wafer. Heated potassium hydroxide (KOH) solutions can be used for preferential crystallographic etching of silicon. The etch rate depends on crystallographic orientation of the silicon and the concentration of KOH solution used; the temperature of KOH solution is 90°C. Normal etch rates are about 1µm/minute. However, due to the different etch rates of silicon on different crystal direction, with the normal mask of Si_3N_4 (see Figure 5-3 a) the cavities after etching are not exactly rectangular; the inner corners are over etched (see Figure 5-3 b). This is not a good shape for the rectangular core. By applying the compensation method proposed by Yu [2], the suitable compensation was made to avoid the over etching; the well-shaped rectangular cavities are formed on silicon wafer, see Figure 5-4. To note in Figure 5-4, *D* is the depth of etching which is 200 µm in our cases (150 µm for the core and 50 µm for the bottom copper tracks). This compensation also helps avoiding a problem arising during copper tracks electroplating which is the diffraction of UV light at the over-etched corners during the process of photolithography. The angle slope is 54.7° between the surface and the plane <111> which is similar for the length direction and the width direction.

The 50 µm -thick bottom copper tracks were successfully electro-deposited on the rectangular cavities in silicon wafer, see Figure 5-5. The next step is to test co-sintering of silicon and printed ferrites.

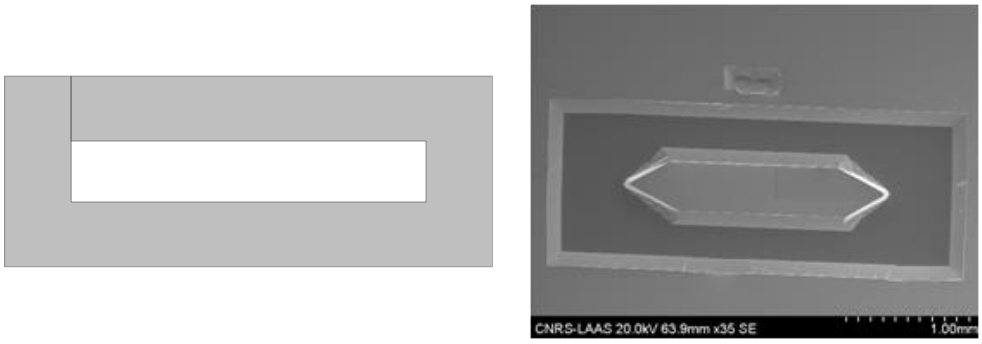

Figure 5-3 : a) Rectangular mask of Si_3N_4 on silicon wafer b)KOH over-etched cavity in silicon wafer

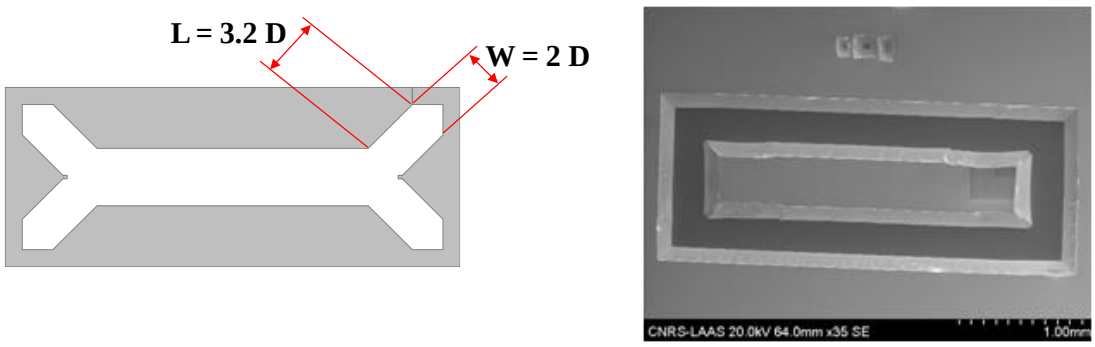

Figure 5-4 : a) Compensated mask of Si_3N_4 on silicon wafer and b) KOH-etched rectangular cavity in silicon wafer

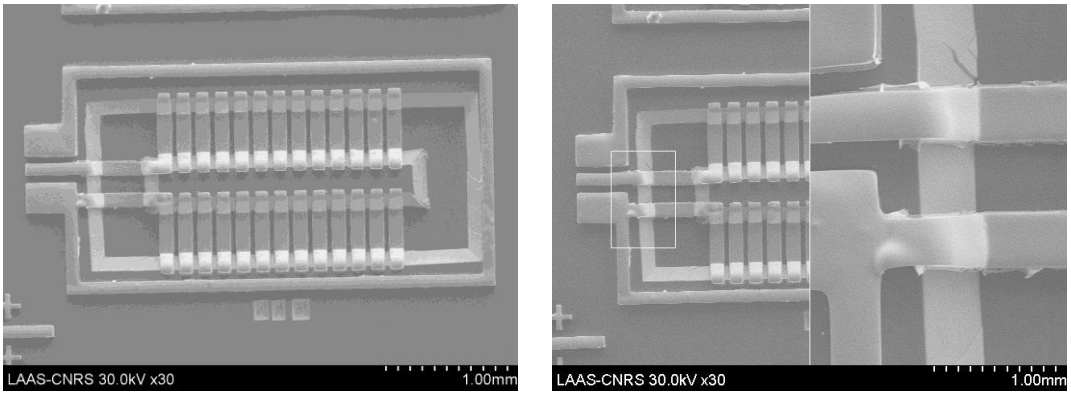

Figure 5-5 : Electro-deposited bottom copper tracks on rectangular KOH-etched cavity in silicon

2.2. Co-sintering Si/Si_3N_4 wafer with printed ferrites

In order to obtain the magnetic phase of ferrite, the printed ferrite needs to be sintered at high temperature (about 900°C). In the monolithic approach, printed ferrites inside the rectangular cavities need to be sintered in the presence of silicon wafer underneath. Hence, the test was carried out to sinter the printed in-house ferrites inside the rectangular cavities in silicon wafer at 980°C during 2 hours under oxygen. After sintering, the cracks appeared at the corners and on the sides of the cores. The shrinkage is roughly 27%. However, grain size is 100 - 500 nm, no big grain is formed, and this means that the ferrite is not fully sintered at 980°C like the free-standing printed in-house ferrite. In order to estimate the temperature at which ferrite is fully densified inside the cavity, we carried out TMA analysis, and the result showed a densification peak at 1030°C i.e the ferrite should be sintered at temperature about 1030°C .

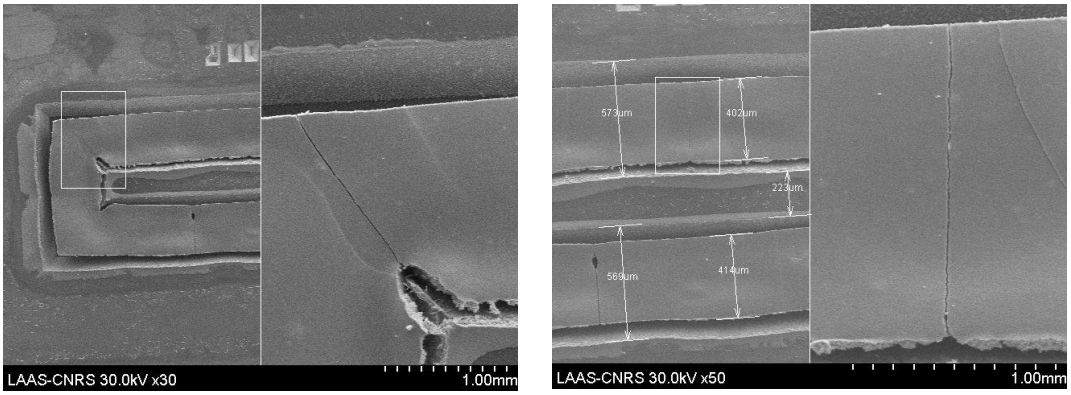

Figure 5-6 : SEM images of in-house printed ferrite in rectangular cavities after sintering at 980° during 2 hours

As the sintering step involves high temperature, the issue that could arise is inter-diffusion of elements between the ferrite layer and the substrate. A barrier layer (silicon nitride Si_3N_4) was grown by low pressure chemical vapor deposition method (LPCVD) on the substrate to avoid metal elements to diffuse into the silicon. The final stack is Si/SiO_xN_y (150 nm) / Si_3N_4 (40 nm)/ferrite U70 (24-66 µm). Interfaces were observed and analyzed with EDS SEM at LAAS and TEMSCAN service at Toulouse

Paul Sabatier University, see Figure 5-7. It can be seen that there is no silicon diffusing into the ferrite part and there is neither metal atom diffusing into the silicon substrate. No diffusion was observed for two times of examining. However, the oxidation and diffusion problems appeared when we co-sintered the copper tracks with silicon substrate underneath at 980°C during 2 hours under air condition. The copper tracks were oxidized and diffused over the surface of silicon wafer (see Figure 5-8).

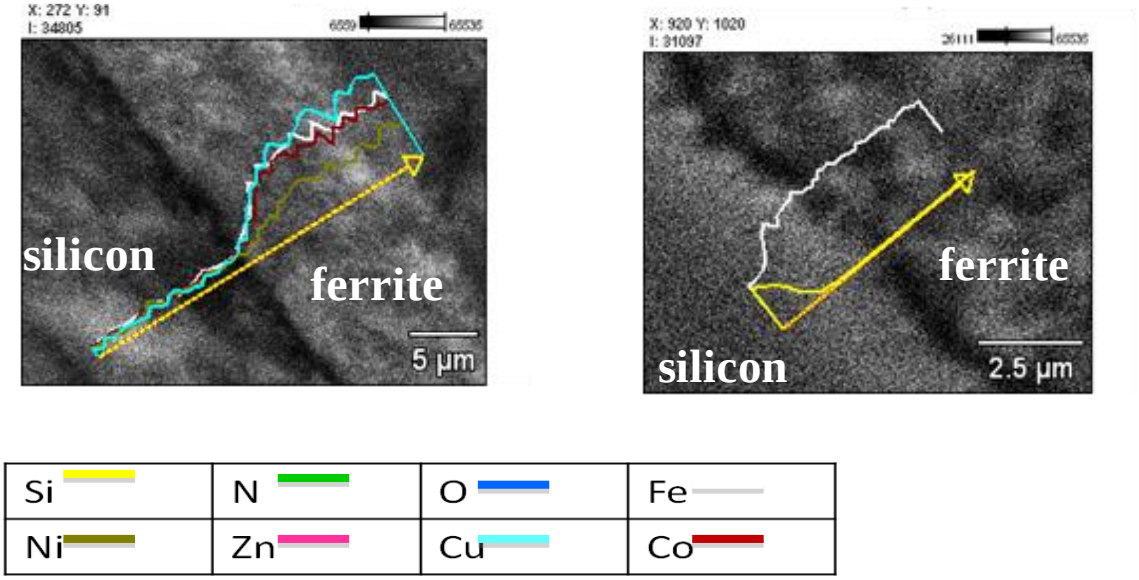

Figure 5-7 : EDS SEM image at the interface between silicon and ferrite after sintering. (Note: The vertical axis is the number of counted atoms)

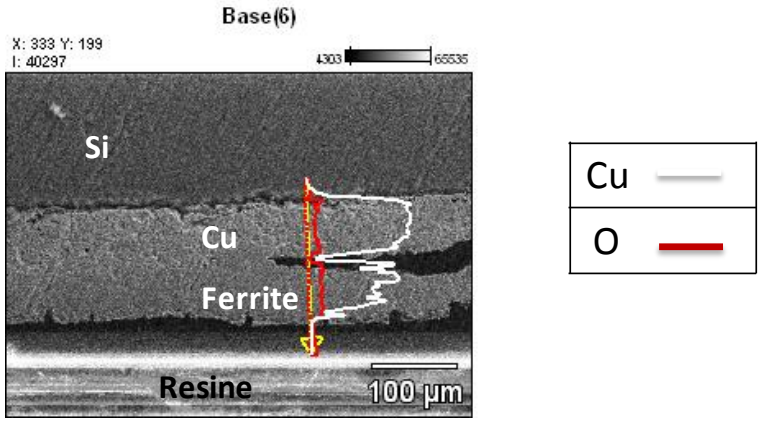

Figure 5-8 : EDS SEM image at the interface of silicon, copper and ferrite after sintering

From these experiments, we see that it is unfeasible to sinter ferrite directly on silicon, with the presence of copper windings, at that high temperature due to the problems of delamination and cracking and the problem of oxidation and diffusion. The monolithic approach confronted with these problems, it was put aside. The hybrid approach was then considered.

3. Process development for hybrid approach

In hybrid approach, the free-standing core is made from commercial thin-film ferrite tapes as cut cores and from in-house ferrites as printed cores (details as given in chapter 2). The conductor windings can be completed by either flip-chip technology or photoresist mold technology.

3.1. Flip-chip bonding

Two silicon wafers with electroplated copper tracks and copper vias were prepared for bonding by flip-chip bonding machine. The results showed that it is difficult to form a close winding circuit for the micro-inductor. It is due to the in-homogeneity of the electrodeposited copper vias. The thickness of all vias on each silicon wafer is not perfectly similar; hence, the copper connection through via is not established at some places. In order to solve this problem, carefully polishing is required. It is not possible for us to do a long-time polishing process at this stage in my thesis; hence, we left the solution with flip-chip bonding aside.

At the end, the thick photoresist mold technology was developed to complete the electro-deposited copper windings. This approach was proposed with SU8 and Bump Plating Negative (BPN) photo-resist [1] which will be presented in the next section.

3.2. Micro-inductor realization with photo-resist mold technology

The final micro-inductor was realized with U200 ferrite according to the hybrid approach. The schematic of process is presented in Figure 5-2.

- Step 1: Deposit 50µm-thick bottom copper tracks on Si/SiO_2 (500nm) wafer.

The layer of SiO_2 helps insulating the integrated inductor electrically from the silicon wafer substrate. In order to deposit bottom copper tracks, seed layers of Ti (500Å)/Au (1000Å) are deposited on the Si/SiO_2 wafer by physical vapor deposition technique. Then, 50µm-thick photo-resist patterned layer is created on the wafer by photolithography technology. Copper tracks are electro-deposited with thickness of about 50 µm and the seed layer of Au is removed by KI + I_2 solution, the seed layer of Ti is removed by HF solution.

- Step 2: Planarization of bottom copper tracks and open vias

A layer of SU8 was sprayed to cover the 50 µm-thick copper tracks with the spray machine AltaSpray. The thickness of the SU8 layer is kept just small enough; this thickness will be characterized with the cross-section of the final micro-inductor. Then, the vias openings are created with photolithography, see Figure 5-9.

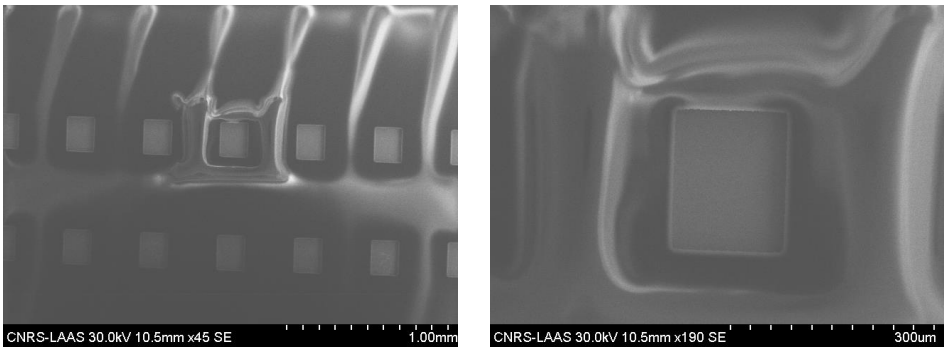

Figure 5-9 : Opened vias on the bottom copper tracks planarized by SU8 photo-resist

- Step 3: Stick ferrite cores on the planarized bottom copper tracks with Epoteck® 353NDT glue by the bonder machine Tresky 3000.

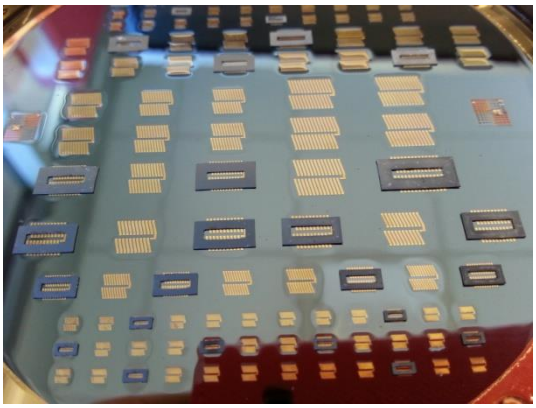

Figure 5-10 : Fixed ferrite cores (both printed and cut) on bottom copper tracks

- Step 4: Cover ferrite cores with SU8 and open vias

A thin layer of SU8 is sprayed over the stuck ferrite cores; the thickness of this layer will be characterized with the cross section of the final micro-inductor. And then, the position of vias is opened with the photolithography technology.

- Step 5: Deposit a seed layer of Ti/Au and photoresist mold formed by photolithography

A seed layer of Ti (500Å)/Au (1000Å) is then deposited. A problem of bubbles arose at this step, Figure 5-11 and Figure 5-12. We can see the residue of photoresist after the bubble was broken. This problem is due to the air present under the layer of stuck ferrite cores, during the process of metallization, the heat generated in the wafer, the air expanded and was evacuated to the surface in the vacuum deposition chamber, creating bubbles in the photoresist. This problem happened at some places and more likely near the stuck cores. The BPN photo-resist is then used with photolithography technology to create photo-resist mold layer upon the seed layer of Ti/Au;the details of lithographic processes can be found in the article [1]. The wafer is ready for the step of electro-deposition.

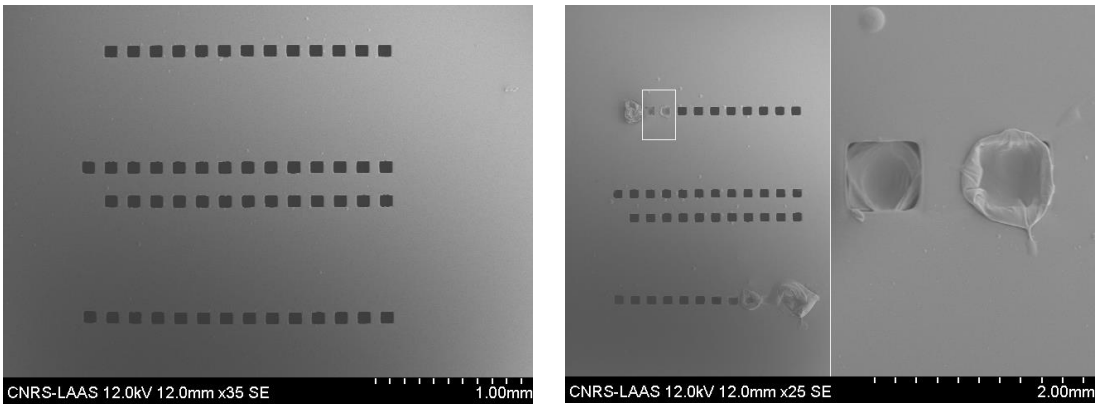

Figure 5-11 : Air-core inductor before the top copper tracks deposition (a) without problem of bubbles and (b) with problem of bubbles

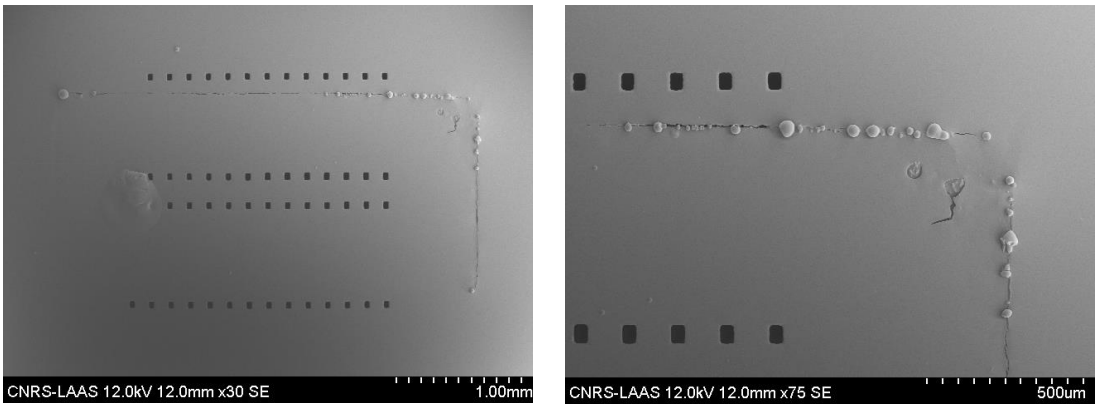

Figure 5-12 : Ferrite-core inductor before the top copper tracks deposition with problem of bubbles

- Step 6: Deposit top copper tracks and vias

Simultaneously, the top copper tracks and vias are electro-deposited in the photoresist mold. Then, the residue of BPN photoresist is removed. The seed layer of Ti/Au is removed. The final micro-inductor is completed as shown in Figure 5-13.

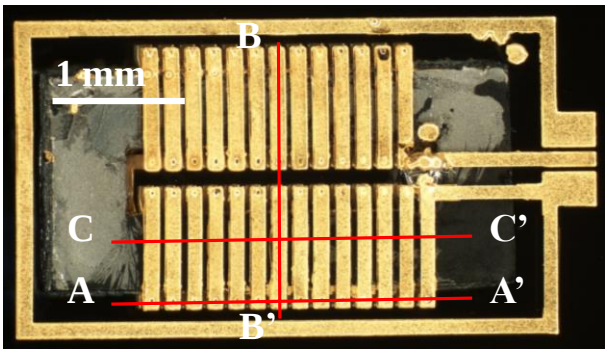

Figure 5-13 : Optical image of final micro-inductor

In order to characterize the layers of electro-deposited copper tracks, copper vias and also the ferrite layers with the SU8 layers, the final micro-inductor was cut with the guide lines A-A', B-B' and C-C'. The cross sections corresponding to the A-A', B-B' and C-C' cut lines were observed by SEM. The

electro-deposited copper vias can be observed in the Figure 5-14. In this figure, we see some good established Cu-via-Cu connections and some bad ones. This can cause the problem of open circuit for the inductor device. The topology of the ferrite core is shown clearly in Figure 5-15. The printed core is thicker at the border and thinner at the center. The thickness of electroplated bottom copper track is about 60 µm and the top copper track is about 50 µm thick. The thickness of ferrite core is about 156 µm at this position. The thickness of the first SU8 layer is about 70 µm and the second layer is about 35 µm (see Figure 5-16). The total thickness of the final inductor is about 370 µm which is higher than 250 µm. This is due to the additional thickness of SU8 photoresist for planarization.

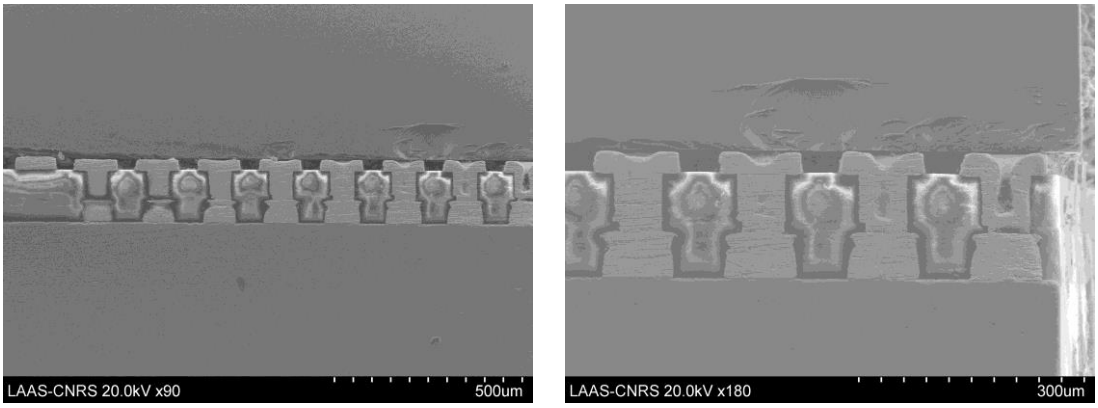

Figure 5-14 : SEM image of inductor's cross section corresponding to A-A' cut line

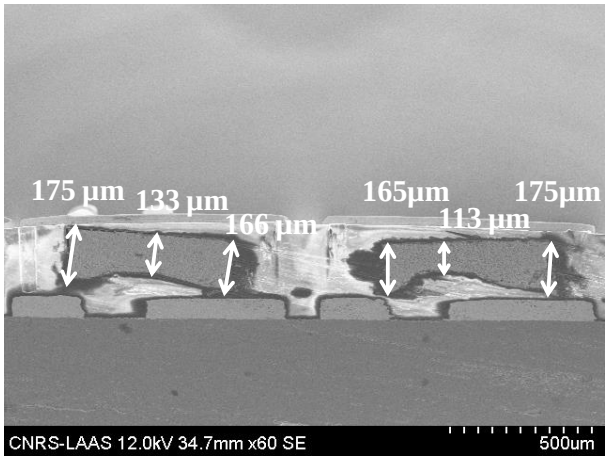

Figure 5-15 : SEM image of inductor's cross section corresponding to B-B' cut line

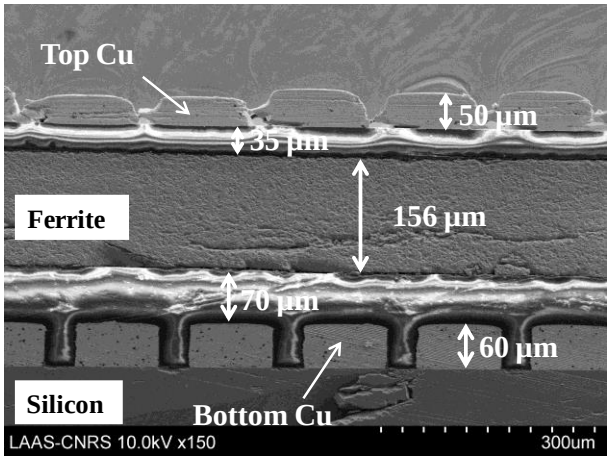

Figure 5-16 : SEM image of inductor's cross section corresponding to C-C' cut line

The electrical characterization was carried out for all air-core and ferrite core inductors. Almost all of them have open circuit; only one air-core has close circuit with resistance of 125 mΩ up to 90 MHz and inductance of 1 nH. The curve of inductance and resistance versus frequency are presented in Figure 5-17.

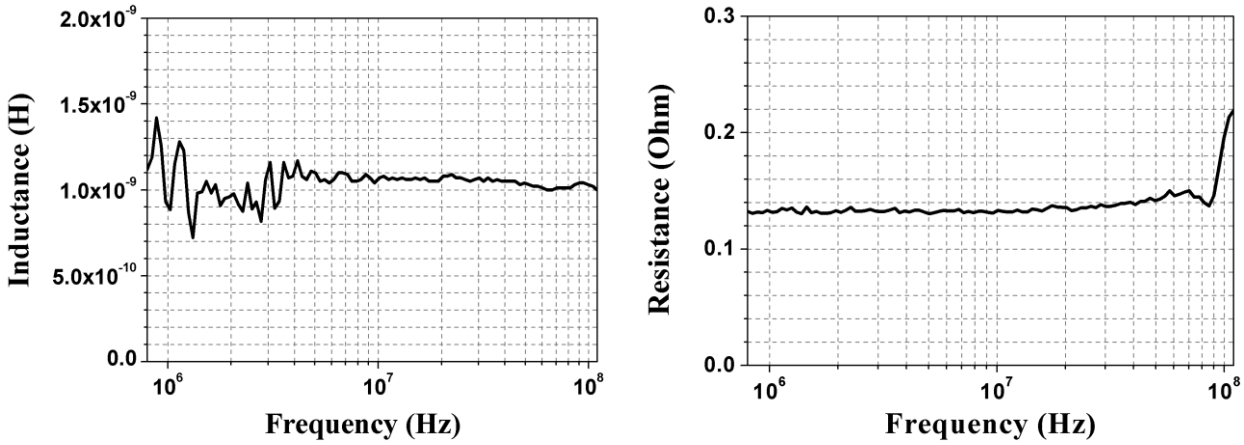

Figure 5-17 : Inductance and resistance of final air-core micro-inductor

Conclusion

Final air-core and ferrite-core inductors were realized with photoresist mold method in the hybrid approach. The DC resistance obtained for an air-core inductor was 125 mΩ up to 90 MHz and this is well in the range of 0.1-0.2 Ω defined in our specifications. However, ferrite inductors were not showing similar range of resistance due to poor electrical contacts. The problem of bubbles degrading the process is to be solved by developing the process of core adhesion with suitable glue and procedure. Fine polishing of copper tracks will certainly improve the process. We believe that it can also be the key to make flip-chip bonding a successful alternative process.

References

1. D. Bourrier, M. Dilhan, A. Ghannam, and H. Granier, "Comparisons of the new thick negative resist to Su8 resist", in *Conference on Micromachining and Microfabrication Process Technology XIII*, San Jose, CA, 2011, 7972
2. J.-C. Yu, "Convex corner compensation for a compact seismic mass with high aspect ratio using anisotropic wet etching of (100) silicon", *Design, Test, Integration and Packaging of MEMS/MOEMS Symposium (DTIP 2011) IEEE*, 197 - 199, 2011

General conclusions and perspectives

In this thesis, we presented the development of integrated inductors based on soft ferrite materials dedicated to low power (1 W) DC/DC converters with high power densities, high efficiencies and medium frequencies.

In the first chapter, we gave the overall context of the work, i.e. DC/DC converter or POL converters and reviewed existing technologies and materials developed for small size and integrated inductors in commercial products and in research laboratories over the world. From this literature study and from constraints defined by the project: maximum size of 3 - 6 mm^2, inductance range of 200-2000 nH, frequency range of 5 – 10 MHz, DC current of 0.6 A and the ease and cost of fabrication, we chose to develop the micro-inductors of toroidal type and based on soft ferrite materials for the core.

The overall methodology was as following: (i) firstly, develop the magnetic cores with feasible dimensions, (ii) extract the magnetic properties of the core especially losses, (iii) implement the properties in a design optimization program to obtain an optimized inductor design and (iv) finally, realize the micro-inductor with the simple and inexpensive processes.

In chapter 2, we selected ferrites in two forms: ferrite tapes and ferrite powders. We chose two permeabilities for each form of materials. The ferrite powders were synthesized. The associated technology with each type of material was developed, including screen printing with different pastes i.e. different viscosity. Fully sintered ferrite cores were successfully realized from commercial thin film ferrite tapes and in-house made ferrite powders. Both cut cores and printed cores are reproducible in size (3 mm^2) and thickness (110 μm) and composition. The cut cores from commercial thin film ferrite have a more homogenous topology in the surface than screen printed ferrite cores. It was shown that the inhomogeneity of the printed cores was a problem during the inductor's fabrication in chapter 5. However, the dimension of cut cores is less precise than the printed ones due to the error deviation of cutting machine. Further development is needed to improve the surface topology of printed cores, for example by using the stencil mask for the process of printing or applying a pressure on the printed core surface before the heat treatment process. However, those tests and developments will take a considerable period of time and effort and at that stage of my thesis I couldn't accomplish them.

In chapter 3, magnetic properties of different selected ferrites were measured by magnetic material test fixture Agilent and impedance analyzer at different AC excitation current and different DC bias current. Permeability and losses of the material were characterized under DC bias 0-1.4 A and different AC excitation current from 0 to 200 mA. At zero DC bias and small induction (< 0.4 mT), the permeabilities of selected commercial ferrites are 200 and 60 stably up to 30 and > 100 MHz while that of in-house made ferrites are 190 and 86 stably up to 30 and > 100 MHz. The dynamic permeability of ferrites changes considerably according to the excitation: DC and AC level. In general,

it decreases with the DC bias current and increases with AC sinusoidal excitation. The inductance densities of 187 $nH.mm^{-2}$ and 138 $nH.mm^{-2}$ could be possibly reached with U200 and U70 ferrites respectively. For commercial ferrites, 215 $nH.mm^{-2}$ and 72 $nH.mm^{-2}$ coud be reached for inductance densities with 40011 and 40010 ferrite cores respectively. Losses of the four ferrites 40010, 40011, U70 and U200 are small at 1 MHz. At 1 – 10 mT, losses are below 100 $mW.cm^{-3}$. Losses shift to higher level for higher frequencies. At 6 MHz and 10 mT, U200 has the lowest losses of 0.7 $W.cm^{-3}$ while 40011 has the highest losses of 2.5 $W.cm^{-3}$. At 10 mT, U200 core presents the lowest losses from 4 MHz. However, the characterization is only performed at small sinusoidal AC signal when the DC bias current is applied due to the limitation of the measurement apparatus. U200 with permeability of about 200 under zero DC bias and small AC current (10mA) with small losses (120 $mW.cm^{-3}$ at 6 MHz and 4 mT) was chosen for the fabrication of final inductors. Losses of U200 are still higher than that of commercial ferrite 4F1 at 10 mT, 3 – 10 MHz. The measured values of permeability and losses, and losses model will be used for the modeling and design optimization in FEMM and Matlab. For perspectives, the characterization of magnetic properties should be carried out at large AC excitation signal under DC bias current and with the real current waveform i.e. triangular signal.

In chapter 4, the inductor design optimization was studied and we have proposed a design methodology based on genetic algorithm. The micro-inductor was simulated with the finite element method using FEMM to compute its electromagnetic properties and the optimization process runs on Matlab software. The design optimization tool was successful to offer a solution which satisfied all the constraints of inductance value and dimensions. The overall method needs to be improved for the accuracy in core losses calculation i.e the analytical losses models and the inductor modeling. The modeling tool should implement the simulation with AC and DC excitation at once.

Two experimental approaches, monolithic and hybrid were considered for the micro-inductor fabrication. But the monolithic method is not possible at the moment due to the problem of cracking, oxidation and diffusion. Final air-core and ferrite-core inductors were realized with photoresist mold method in the hybrid approach. The DC resistance obtained for an air-core inductor was 125 mΩ up to 90 MHz and this is well in the range of 0.1-0.2 Ω defined in our specifications. However, ferrite inductors were not showing similar range of resistance due to poor electrical contacts. The optimized test micro-inductor has an inductance of 107 nH at 0.6 A DC and 20 mA AC with the cut-off frequency of 40 MHz. The problem of bubbles degrading the process is to be solved by developing the process of core adhesion with suitable glue and procedure. Fine polishing of copper tracks will certainly improve the process.

We believe that improving the topology of cores and copper vias can also be the key to make flip-chip bonding a successful alternative process.

For long-term perspectives, the magnetic materials should be improved further for lower losses and higher DC current. The developed processes (screen printing and milling) are ready to apply for other types of magnetic materials. An important perspective is to implement the final micro-inductor in a circuit (DC/DC converter) and measure losses (under real triangular waveform signal) to compare with the actual losses measurement method (under sinusoidal waveform signal). The flip chip bonding technology is to be developed and tested with better topology of copper vias and cores.

Annexes

A.1. Table of state-of-the-art of integrated inductor

Table A1-1: Examples of commercial inductors for DC-DC converters

Year	-	-	-	2013	-	-	-
Institution/company	TDK	TDK	TDK	Coilcraft	Murata	Murata	FDK
Product	VLS201612ET series	MHQ 0402P series	MHQ 1005P series	LPS3010 series	LQH32P series	LQH44P series	MIPSZ2012 series
Structure	Wire wound	SMD	SMD	-	Wire wound	-	-
Size (mm^3)	2x1.6x1.2	0.44x0.24x0.24	1x0.6x0.6	3x3x1	3.2x2.7x1.55	4x4x1.65	2x1.2x1
Inductance	0.47uH-10uH at 1MHz	0.2nH-33nH at 500MHz	0.7nH-150nH at 500MHz	0.47µH-330µH	0.47uH-120uH	1uH-22uH at 1MHz	0.5-4.7µH at 1MHz
Self-resonance frequency	-	10GHz-1.5GHz	15GHz-0.8 GHz	370MHz-7MHz	100MHz-8MHz	90MHz-17MHz	100MHz-35MHz
Rated current	1.9A-0.47A	0.32A-0.13A	1.2A-0.11A	2.3A-0.11A	2.55A-0.2A	2.45A-0.79A	1.3A-0.7A
DC resistance	0.063Ω-1.026Ω	0.2Ω-3.5Ω	0.03Ω-3Ω	0.07Ω-18.5Ω	0.03Ω-4.38Ω	0.03Ω-0.37Ω	0.06Ω-0.23Ω
Technology	Ferrite Multi-layer ceramic	Multi-layer ceramic	Ferrite	-	-	-	Multi-layer CAE

Table A1-2a: Proposed integrated inductors with spiral structure

Year		2009	2009	2011	2011
Institution		Dong H. Bang, Kwangwoon Univ. [1]	Seok Bae, Alabama Uni. [2]	Jaejin Lee, Alabama Uni. [3]	Mingliang Wang, Qualcomm Inc. [4]
Structure		Spiral	Sprial	Spiral	Spiral pot core
Size (mm^3)		5.2x4.7x0.5	5x5	5x5	3x3x0.6
Number of turns		9	4.5	4.5	10
Inductance		0.81µH at 10MHz	48.5nH at 10MHz	50nH at 10MHz	390nH at 6MHz
Max frequency		-	30MHz	-	6 MHz
DC current		0.47A	-	2.5A 5% inductance drop at 10MHz	I_{sat} > 7A
DC resistance		-	-	-	0.12Ω and 1.15Ω at 6MHz
Material	Magnetic	NiZn ferrite composite screen printed	NiZnCu ferrite 2x1µm sputter and heat treatment 800°C	Ferrite film 2.5µm thick sputtering	NiZn ferrite composite 200 µm µ=6

	Conductor	Cu 85µm wide 150µm thick metal foil	Cu 90µm electroplated	Cu 65µm thick	Cu electroplated 200µm heightx60µm wide
	Isolator	-		-	-
Technology		PCB substrate	On silicon	On silicon	In silicon

Table A1-2b: Proposed integrated inductors with spiral structure

Year		2012	2013	2013	2014
Institution		Christopher D. Meyer, US army lab [5]	Yuichiro Sugawa, Shinshu Uni. [6]	S. Bharadwaj, Osmania Uni. [7]	Elias Haddad Ampere lab, France [8]
Structure		Spiral	Spiral	Spiral	Spiral
Size (mm^3)		1x1x0.09	1x1	5x5 >1mm thick	9 mm^2 >2.6mm thick
Number of turns		10	2	3	6
Inductance		109nH up to 100 MHz	5.5nH at 100 MHz	75nH at 1MHz	500nH
Max frequency		$Q=Q_{max}$ at 28MHz	Resonance frequency 600MHz	100 MHz	100MHz
DC current		-	I_{sat} = 5.5A	-	-
DC resistance		0.85Ω DC and 50Ω at 100MHz	18mΩ	0.16Ω	140mΩ at < 0.5MHz 100Ω at 100MHz
Material	Magnetic	Air	Carbonyl-iron composite 97.8%Fe 1%C screen printed 2x30µm µ=7.5	NiZnCu ferrite microwave sinter and screen printing co-firing	Yittrium Iron Garnet YIG µ=25 at 100MHz
	Conductor	Cu electroplated	Cu electroplated 35µm thickx140 µm wide	Cu screen printed 1µm thickx 80µm wide	Cu 50µm electroplated
	Isolator	-	-	-	Bismaleimide
Technology		On silicon	Glass substrate	Microwave sintering 900°C/30min	Thick film YIG

Table A1-3: Proposed integrated inductors with solenoid structure

Year	2006	2008	2011	2013
Institution	Xiao-Yu Gao, Micro_nao Tech Inst. China [9]	Dok Won Lee, Stanford Uni. [10]	Hongwei Jia, Florida Uni. [11]	Ryan P. Davies, Columbia Uni. USA [12]
Structure	Solenoid	Solenoid	Solenoid	Solenoid
Size (mm^3)	-	0.88mm^2	20mm^2	
Number of turns	-	17.5	3	4
Inductance	5.4µH at 1 MHz and 2µH at 10 MHz	70nH at 10MHz	450nH	7.4nH at 100 MHz
Max frequency	7 MHz $Q = Q_{max}$	< 30MHz	>5MHz	-
DC current	-	-	-	-

DC resistance		-	0.67Ω	20mΩ	0.48Ω and 1.7Ω at 100MHz
Material	Magnetic	NiFe magnetic film electroplated	Amorphous CoTaZr 2.2µm sputter and wet-etched μ_r=300 for processed core and μ_r=600 for blanket film	Ferrite epoxy glob core	Ta 5nm/ CoZrTa 200nm/ SiO_2 7nm 20 laminations
	Conductor	Cu electroplated	Cu electroplate 6.6µm thick top and 4.4µm thick bottom	Wire bonding	Cu 5µm electroplated
	Isolator	Polyimide	Polyimide	-	SU8
Technology		On glass	On silicon	Bond wire inductors	On silicon

Table A1-4: Proposed integrated inductors with racetrack structure

Year		2007	2011		2012	2013
Institution		Ningning Wang, Tyndall Inst. Ireland [13]	Ronan Meere, Athlone Ints. and Tyndall Inst. [14]		Naigang Wang, IBM research USA [15]	Daniel V. H., Darthmouth USA [16]
Structure		Racetrack A1	Racetrack	Spiral	Racetrack	Racetrack
Size (mm^3)		-	4.62x1.6x0.16	2.7x2.7x0.09	1mm long	25-50mm^2 0.17mm
Number of turns		3	5	12	6	7
Inductance		220nH up to 3 MHz	230nH	220nH	125nH at <10 MHz	1.1-1.2µH
Max frequency		3 MHz	<10 MHz	50 MHz	200 MHz	8.3-11.8MHz
DC current		I_{sat} = 0.6A	-	-	-	-
DC resistance		0.21Ω	0.32Ω	0.54Ω	0.16Ω (2 turns) DC	0.84-1.1Ω
Material	Magnetic	$Ni_{45}Fe_{55}$ electroplated 10µm bottom, 5µm top, 4mm long	$Ni_{45}Fe_{55}$ alloy electroplated with resistivity 45µΩ.cm	Air	$Ni_{45}Fe_{55}$ 1.5 µm electroplated	CoZrO sputtered 35µm
	Conductor	Cu 64 µm wide x 46µm thickness electroplated	50µm thick x50µm wide	50 µm thick x50µm wide	Cu 40µm wide electroplated	Cu 40µm electroplated
	Isolator	SU8 photoresit	-	-	-	SU-8 25µm
Technology		On silicon	On silicon	On silicon	On silicon	In silicon

Table A1-5a: Proposed integrated inductors with toroidal structure

Year	2006		2006	2009	2012
Institution	Hahn R., Fraunhofer, Germany [17]		Orlando, Limoges, ST Microelectronic, France [18]	Flynn D., Herriot Watt, UK [19]	Peter Kamby, Technical Uni. Denmark [20]
Structure	Toroidal RK1	Spiral SP5	Toroidal	Toroidal	Toroidal
Size (mm^3)	3.2x3.2x0.4	5.2x5.2X0.4	5.6x5.6x0.2	2x5x0.25	8.4x8.4x1.6

Number of turns		15	5	12	33	8
Inductance		1 µH	4.7µH	0.5µH	0.3-1.7µH	52nH
Max frequency		< 1 MHz	< 1 MHz	10MHz	<1 MHz	200 MHz
DC current		0.1 A 30% inductance decrease	0.1 A 20% inductance decrease	I_{sat} = 0.18A	I_{sat}< 0.14A	-
DC resistance		40mΩ	260mΩ	95mΩ	100mΩ	0.22Ω
Material	Magnetic	Ferromagnetic	Ferromagnetic	laminated $SiO_2/Ni_{80}Fe_{20}$ physical vapor deposition 16 x 1 µm µ=900	$Ni_{80}Fe_{20}$ permalloy 10-20µm electroplated	-
	Conductor	Au or Ag	Au or Ag	Cu electro-deposited 20µm	Cu or Ni 90µmx200µm	Cu 10µm
	Isolator	-	-	-	Photoresist 5µm	-
Technology		Ferromagnetic LTCC	Ferromagnetic LTCC	In silicon	Electro-deposition Flip chip	Printed circuit board toroid

Table A1-5b: Proposed integrated inductors with toroidal structure

Year		2012	2012	2013	2013	2014
Institution		Jiping Li, Uni Florida USA [21]	Jizheng Qiu, Darthmouth USA [22]	Jooncheol Kim, Georgia Inst. [23]	X. Fang, Hong Kong Uni. [24]	Xuehong Yu Georgia Inst. [25]
Structure		Toroidal	Toroidal	Toroidal	Toroidal	Toroidal
Size (mm^3)		13x13x0.32	5.6x5.6 -	10x10x1	1.4x2.1x0.4	6x6x0.3
Number of turns		36	3	36	11	25
Inductance		0.16µH	8.9nH	1.6µH at 10 MHz	43.6nH	0.14-0.17µH
Max frequency		>14MHz	50MHz	-	65MHz	>10 MHz
DC current		-	-	-	I_{sat} = 10A	-
DC resistance		0.27Ω DC and 1.38Ω at 14MHz	-	-	280mΩ and 1.09Ω at 65MHz	0.58-0.75Ω at 10 MHz
Material	Magnetic	NiZn magnetic composite 200µm µ=6-25	CoZrO 40µm Sputtering 4 times	CoNiFe 40x1µm laminated electrodeposited	MnZn ferrite composite µ=5	Iron powder 0.25mm lapping
	Conductor	Cu 40-60µm electroplated	Cu 50µm	Cu electroplated	Cu electroplated	Cu 30µm electroplated
	Isolator	-	-	-	-	Parylene and SU8
Technology		Embedded in silicon	-	Electro-deposition	In silicon	Embedded in silicon

A.2. Process of realizing cut cores from commercial thin film ferrite

Procedure to realize cut cores from commercial thin film ferrite:

- Stack two layers of thin film ferrite upon each other.
- Start: open N_2 and O_2 valves, turn on computer and AML machine (see Figure A), turn on alignment sensor.
- Place two layers of ESL film in between 5" silicon wafer and 1x1 cm^2 silicon plate (see Figure) and between the two load plates of AML machine. Then, close the load cover.
- Start AML interface in the computer, choose the manual option and start the process.
- Open valve, start pump, wait until the vacuum reach 10^{-3} mbar, during that time turn on heating 90°C for upper and lower plate. When pressure reached 10^{-3}, apply pressure 800N on the plate by screw the wheel, in 10 minutes.
- Turn off heating, release the pressure between two plate to 0, turn off pump, close valve. Open N_2 valve to cool down system.
- Collect the bonded sample.
- Load new sample or close the system. Turn off machine and computer, close all the valves.
- Bring sample for cutting by micro-milling machine Réalméca RV2 SP (Figure A2-). Collecting the cut core by dipping the ferrite sample inside the acetone (**Error! Reference source not found.**). Then, measure the dimension of cut cores.

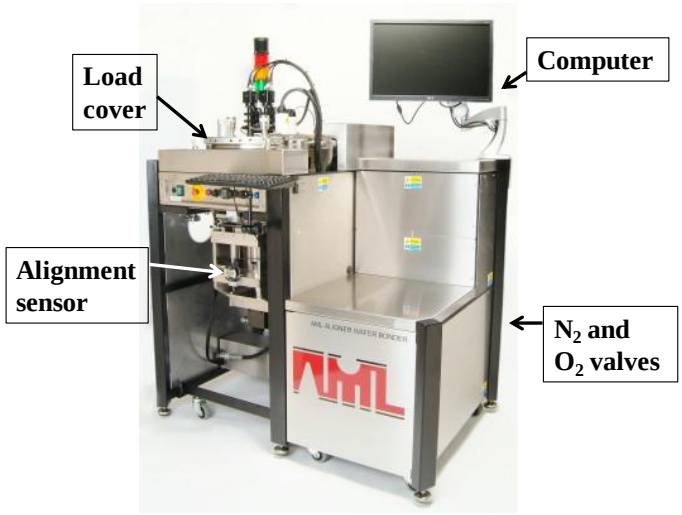

Figure A2-1: Aligner wafer bonder AML AWB04

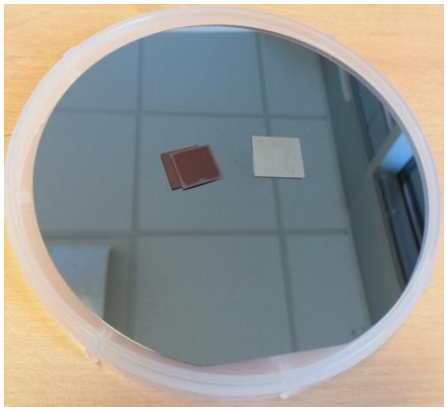

Figure A2-2: Two layers 1cmx1cm of thin film commercial ferrite and 1cmx1cm silicon plate on the silicon wafer

Figure A2-3: Micro-milling machine Réalméca RV2 SP (left) and 200 µm end mill (right)

A.3. Equipments for fabricating in-house made ferrite and realizing printed cores

Figure A3-1: The attritor mixer

Figure A3-2: The zirconia balls (left) and the slurry after mixing

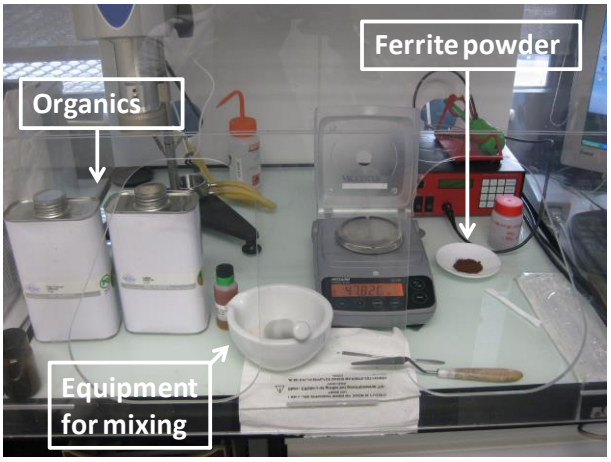

Figure A3-3: Ferrite paste preparation

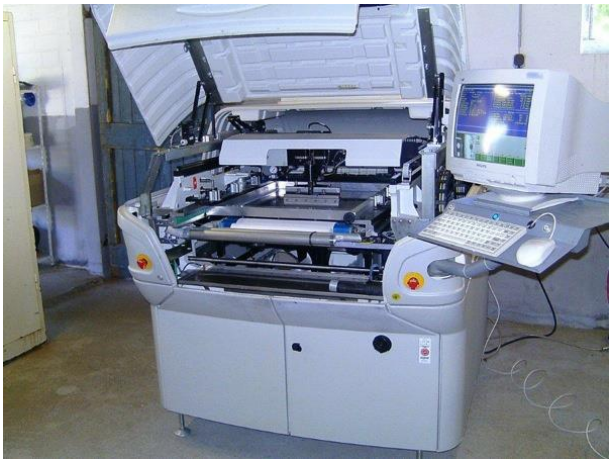

Figure A3-4: Screen printing machine DEK Horizon 01i

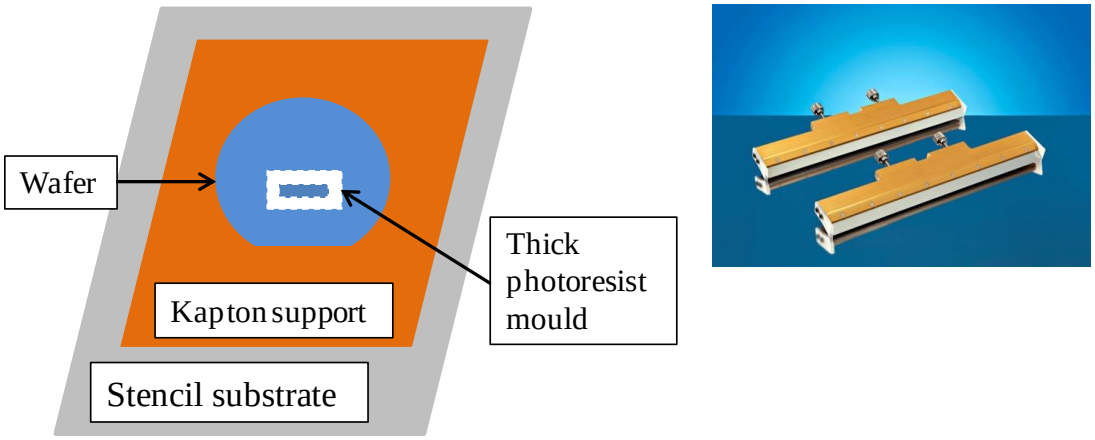

Figure A3-5 : Kapton® polyimide support and the wafer on the stencil substrate (left) and metal squeegees for screen printing (right)

A.4. Principle of thermomechanical analysis

Thermomechanical analysis (TMA) can measure the sample displacement, e.g. growth or shrinkage, as a function of temperature, time, and applied force. TMA analysis can help to understand sintering behavior and phase change position. A schematic diagram of TMA analysis apparatus is given in Figure A4-. A probe rests on the sample on a stage with minimal downward pressure. The probe is integrated with an inductive position sensor. The easily accessible chamber is located in the center of the furnace. Both temperature and atmosphere can be controlled. In addition, an optional mass flow controller is available for purge gas regulation. The gas can be evacuated and allows to measure under a defined atmosphere. In our analysis for ferrites, the measurement is carried out under air. The system is heated at a slow rate. If the specimen expands or contracts, it moves the probe. The inductive position sensor records this movement. A thermocouple close to the specimen measures the temperature. The TMA analysis helps us determining the temperature and duration for sintering ferrites.

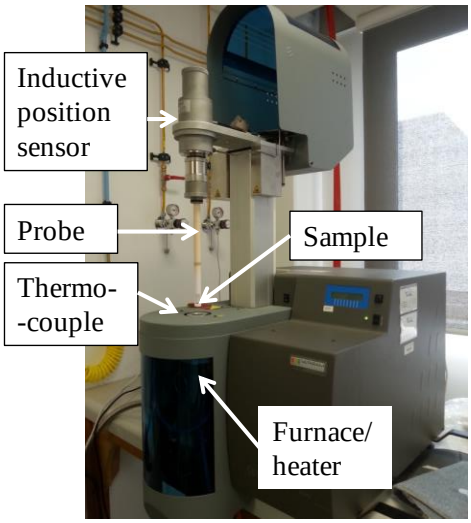

Figure A4-1: SERATAM SETSYS evolution apparatus for TMA analysis

A.5. Principle of scanning electron microscopy and energy dispersive spectroscopy

Scanning electron microscopy (SEM) allows us to observe the microstructure of the ferrites. Samples must have a nearly perfect flat surface for observation. The principle of observation by electron microscopy is to bombard the sample with an electron beam. Different responses are emitted according to the nature of the collision between the electrons and the incident surface of the sample, see Figure A5-. Different signals are received by the appropriate detectors, synchronized with the scanning of the imaging surface, and then, to reconstitute a two-dimensional electronic image of the surface. The secondary electrons and backscattered electrons are used for topographical characterization. The secondary electrons are the result of inelastic collisions in which the incident electron beam transfers part of their energy to the atoms of the specimen by exciting the ejection of another electron in the specimen, called secondary electrons; they have low energy of a few hundred eV. The backscattered electrons are the result of the elastic collisions in which the electrons of the incident beam have the direction changed and their kinetic energy remained due to the large difference between the mass of electron and nuclear. These two species, backscattered electrons and secondary electrons are collected by scintillation detectors which absorb the emitted light and reemit it in the form of electrons via the photoelectric effect. The signal is then amplified by a photomultiplier for the image.

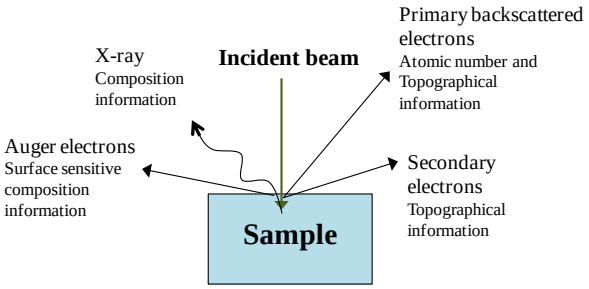

Figure A5-1: Interaction of incident electron beam with the sample specimen

Figure A5-2: Scanning electron microscope Hitachi 4800 for microstructure observation

Energy dispersive spectrometry (EDS) uses the emitted X-ray spectrum, and/or Auger spectrum to obtain a localized chemical analysis. In principle, all elements from atomic number 4 (Be) to 92 (U) can be detected. This analytical technique equipped with SEM determines the chemicals present and their concentrations in the sample specimen. Following the ejection of a secondary electron, a hole is created in the shell of the atom. This hole is subsequently filled by an electron from an outer shell and the superfluous energy is emitted as a characteristic X-ray photon or the superfluous energy is transferred to another electron which is subsequently ejected as Auger electron. These X-ray or Auger photons correspond to the transition energy between the outer layer and inner layer and are characteristic to the atoms and help identify the chemical of atoms at the surface. Detection and analysis of X-ray and/or Auger photons allow the identification and the quantification of chemical elements in the surface of sample.

A.6. Principle of vibrating sample magnetometer measurement

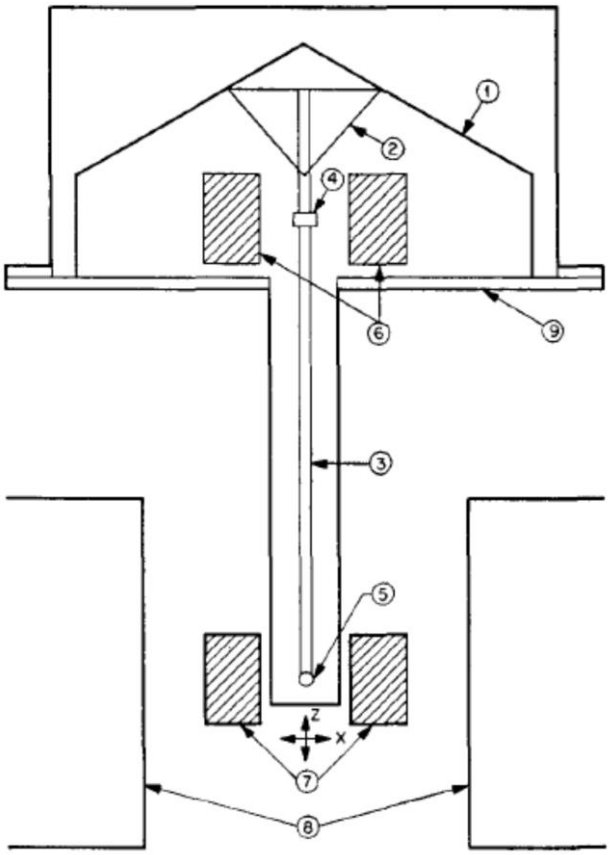

Figure A6-1: Simplified form of vibrating sample magnetometer (Simon Foner). (1) loud-speaker transducer, (2) conical paper cup support, (3) Rod, (4) reference sample, (5) sample, (6) reference coils, (7) sample coils, (8) magnet poles, (9) metal container.

A vibrating sample magnetometer or VSM is a scientific instrument that measures magnetic properties, invented in 1955 by Simon Foner at Lincoln Laboratory MIT. The magnetic induction measurement involves observation of the voltage induced in a detection coil by a flux change when the sample position is changed. A sample is placed inside a uniform magnetic field to magnetize the

sample. The sample is then physically vibrated sinusoidally, typically through the use of a piezoelectric material. In vibrating sample magnetometer, the sample motion is perpendicular to the applied field. The basic instrument is briefly described in figure 1. The sample (5) is vibrated perpendicularly to the applied field. The oscillating magnetic field of the vibrating sample induces a voltage in the stationary detection coils or pickup coil (7), and from measurements of this voltage the magnetic properties of the sample are deduced. A second voltage is induced in a similar stationary set of reference coils (6) by a reference sample (4), which may be a small permanent magnet or an electromagnet. Since the sample and the reference are driven synchronously by a common member, the phase and amplitude of the resulting voltages are directly related. The known portion of the voltage from (6), phased to balance the voltage from (7), is then proportional to the magnetic moment of the sample. In a typical setup, the induced voltage is measured through the use of a lock-in amplifier using the piezoelectric signal as its reference signal. By measuring in the field of an external electromagnet, it is possible to obtain the hysteresis curve of the material.

A.7. Principle of complex permeability measurement by magnetic test fixture Agilent 16454A

In this method, a toroidal core is coiled with a wire and relative permeability is calculated from the measured inductance values. This value is measured by impedance analyzer Agilent 4294A. The principle of complex permeability measurement using the test fixture 16451A is explained in this part.

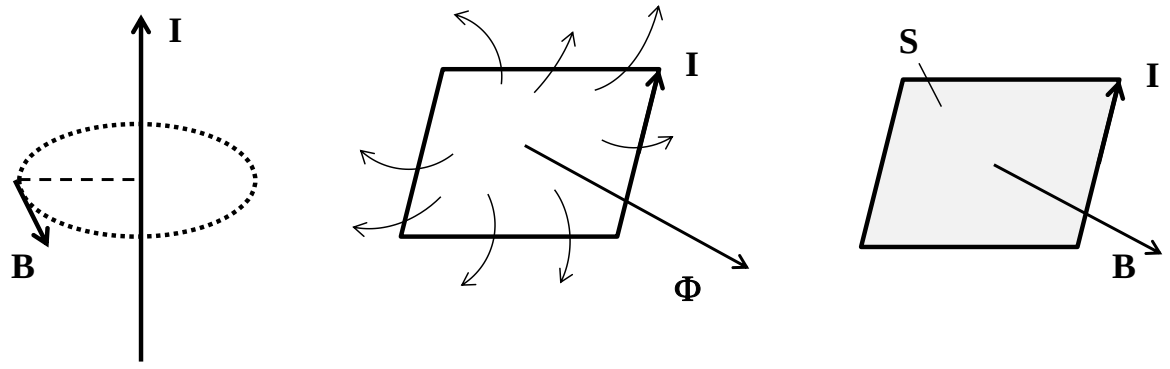

Figure A7-1: Relationship among current I, magnetic flux Φ and magnetic flux density B

Magnetic flux density induced by current flowing in an infinitely long straight wire is expressed by the followed equation

$$B = \frac{\mu I}{2\pi r} \qquad \textit{(Eq. A7.1)}$$

Magnetic flux induced by current in closed loop is

$$\phi = LI \qquad \textit{(Eq. A7.2)}$$

in which L is self-inductance of the closed loop.

Furthermore, this magnetic flux can be expressed by integrating the magnetic flux density B throughout the enclosed surface

$$\phi = \int Bds$$

When the toroidal coil is mounted in 16454A, an ideal one turn inductor is formed as shown in the followed figure

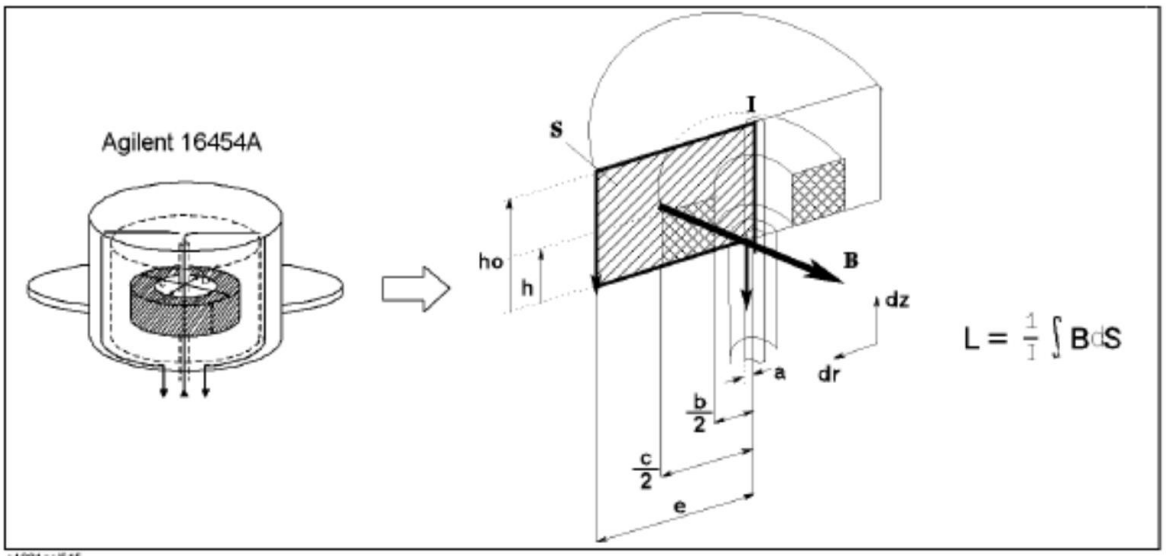

Figure A7-2: Measurement principle using test fixture 16454A (Agilent document)

We have,

$$L = \frac{1}{I}\int Bds = \int_a^e \int_0^{ho} \frac{\mu}{2\pi r} drdz$$

By several mathematical transformations we get,

$$L = \frac{\mu_0}{2\pi}\left((\mu_r - 1)h \ln\frac{c}{b} + h_0 \ln\frac{e}{a}\right) \qquad \textit{(Eq. A7.3)}$$

When the toroidal magnetic core is not mounted, the self inductance is

$$L_{SS} = \frac{\mu_0}{2\pi} h_0 \ln\frac{e}{a}$$

Then,

$$\mu_r = \frac{2\pi(L - L_{SS})}{\mu_0 h \ln\frac{c}{b}} + 1 \qquad \textit{(Eq. A7.4)}$$

As alternating current causes inductance loss, the self-inductance L of the measurement circuit is expressed as complex impedance

$$L = \frac{Z^*}{j\omega}$$

Denoted Z^*_{sm} as the impedance of the 16454A test fixture with no magnetic core mounted and Z^*_m as the impedance of the test fixture with the magnetic core mounted, we get the complex permeability of the magnetic material

$$\mu^*_r = \frac{2\pi(Z^*_m - Z^*_{sm})}{j\omega\mu_0 h \ln\frac{c}{b}} + 1 \qquad \textit{(Eq. A7.5)}$$

A.8. Description of electric set-up for losses measurement

For the sake of simplicity, two expressions were used to describe two electric measurement set-ups. It is called "I_{AC} losses" for the losses measured by Agilent 4284A (I_{AC} and frequency as parameters) and "I_{DC} losses" for the losses measured by Agilent 4294A (I_{DC} and frequency as parameters).

A.8.1. Electric set-up for I_{AC} losses measurement

A.8.1.1. Measurement set-up

The measurement set-up for measuring I_{AC} losses is depicted in Figure A8-. A SIGNATOR station is used for electrical characterization of integrated components, and the Kelvin probes are connected. These four points are connected to the impedance analyzer by four coaxial cables.

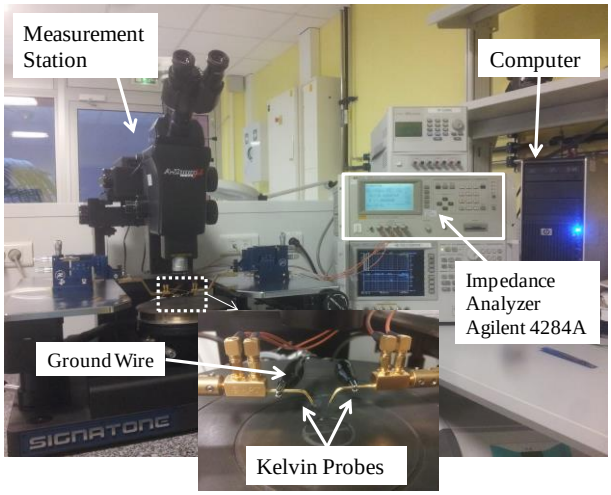

Figure A8-1: Measurement set-up to measure I_{AC} losses

A.8.1.2. Kelvin probes

To minimize the influence of electrical resistance of the inductor on the magnetic losses, we used Kelvin probe.

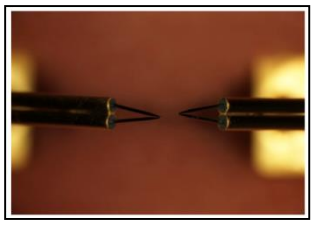

Figure A8-2: Kelvin probe

The principle of Kelvin probe is “four point method” which separates the injection of current (H_c and L_c of impedance analyzer) and the measurement of potential (H_p and L_p of impedance analyzer). The electrical resistance of cables and the metallic contact of inductor is not included in the voltage drop of the terminal of inductor.

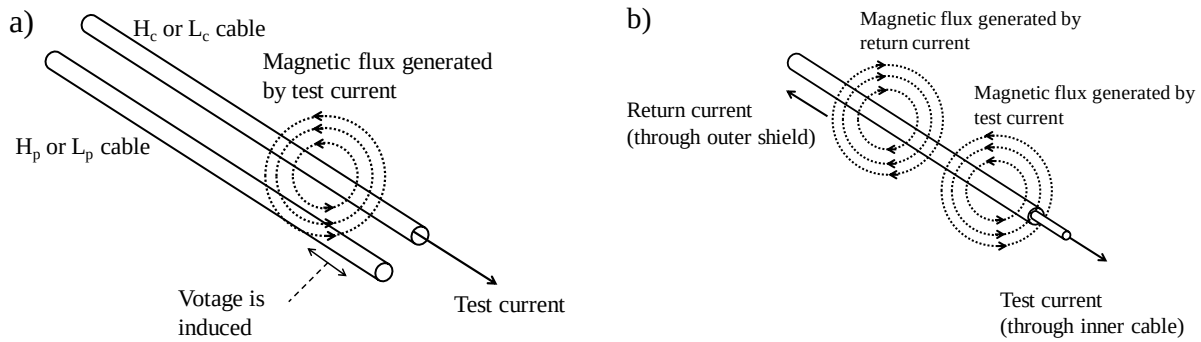

Figure A8-3: a) Phenomenon of coupling inducing a voltage and b) Cancel the voltage by the ground wire

The phenomenon of magnetic coupling between two cables (for example H_p and H_c) will result in an induced voltage and introduce errors of measurements. The solution is to connect the ground wire to create a current in the reverse direction to allow another magnetic coupling to cancel each other [26].

A.8.1.3. Impedance analyzer Agilent 4284A

The length of four coaxial cables, about 1m, influences the measurement under the form of parasitic inductance. To eliminate this error, three calibrations are done on the impedance analyzer before each series of measurement: (i) “phase compensation” to compensate the phase discrepancy between voltage and current, (ii) “fixture compensation SHORT” to compensate the parasitic inductance and (iii) “fixture compensation OPEN” to compensate the parasitic capacitance.

A.8.2. Electric set-up for losses measurement with I_{DC} bias

A.8.2.1. Measurement set-up

The measurement set-up for measuring losses with I_{DC} bias is depicted in Figure A8-. In this set-up, the measurement station is equipped with RF probe which is connected to the impedance analyzer

with a RF coaxial cable. To inject a continuous current during measurement, adapter Agilent 16200B is connected to Agilent 4294A station.

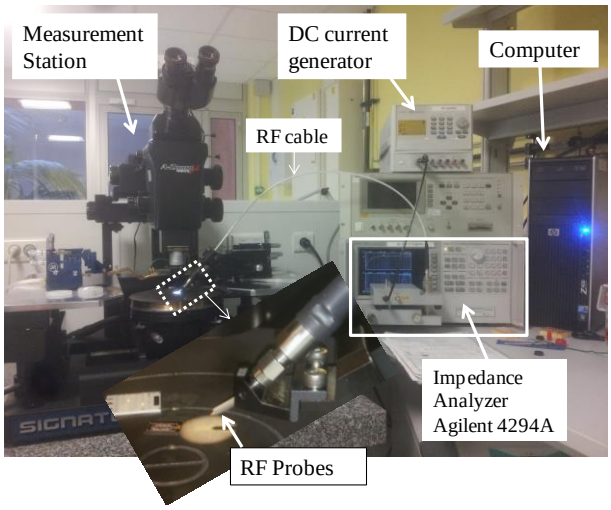

Figure A8-4: measurement set-up to measure I_{DC} losses

A.8.2.2. RF probe

Above 1 MHz, the phenomenon of electric wave reflection can appear and introduce large error to the measurement. Due to that, the RF probe made of ceramic is necessarily used in this frequency range: two points are connected to the ground of the circuit and the central point injects excitation signal.

Figure A8-5: RF probe and 'ground-signal-ground' configuration (on top left)

A.8.2.3. Impedance analyzer Agilent 4294A

For the same reason of eliminating the problem of parasitic inductance, capacitance, the calibrations are necessary as "phase compensation", "fixture compensation: OPEN", "fixture compensation: SHORT". However, the measurement at high frequency needs another calibration which is "Fixture compensation: LOAD". All steps of calibration are done when the adapter and current generator are connected to the measurement set-up (with I_{DC} = 0A). When the calibration is done and saved, the measurement can be carried out and the results of the measurement are analyzed.

References

1. D. H. Bang and J. Y. Park, "Ni-Zn Ferrite Screen Printed Power Inductors for Compact DC-DC Power Converter Applications", *IEEE Transactions on Magnetics*, 45 (6), 2762-2765, 2009
2. S. Bae, Y.-K. Hong, J.-J. Lee, J. Jalli, G. S. Abo, A. Lyle, B. C. Choi, and G. W. Donohoe, "High Q Ni-Zn-Cu Ferrite Inductor for On-Chip Power Module", *IEEE Transactions on Magnetics*, 45 (10), 4773-4776, 2009
3. J. Lee, Y.-K. Hong, S. Bae, J. Jalli, J. Park, G. S. Abo, G. W. Donohoe, and B.-C. Choi, "Integrated Ferrite Film Inductor for Power System-on-Chip (PowerSoC) Smart Phone Applications", *IEEE Transactions on Magnetics*, 47 (2), 2011
4. M. L. Wang, J. P. Li, K. D. T. Ngo, and H. K. Xie, "A Surface-Mountable Microfabricated Power Inductor in Silicon for Ultracompact Power Supplies", *IEEE Transactions on Power Electronics*, 26 (5), 1310-1315, 2011
5. C. D. Meyer, S. S. Bedair, B. C. Morgan, and D. P. Arnold, "Influence of Layer Thickness on the Performance of Stacked Thick-Film Copper Air-Core Power Inductors", *IEEE Transactions on Magnetics*, 48 (11), 4436-4439, 2012
6. Y. Sugawa, K. Ishidate, M. Sonehara, and T. Sato, "Carbonyl-Iron/Epoxy Composite Magnetic Core for Planar Power Inductor Used in Package-Level Power Grid", *IEEE Transactions on Magnetics*, 49 (7), 4172-4175, 2013
7. S. Bharadwaj, T. Ramesh, and S. R. Murthy, "Fabrication of microinductor using Nanocrystalline NiCuZn ferrites", *Journal of Electroceramics*, 31 (1-2), 81-87, 2013
8. E. Haddad, C. Martin, C. Joubert, B. Allard, C. Buttay, T. A. Tannous, and P. Bevilacqua, "Planar, double-layer magnetic inductors for low power, high frequency DC-DC converters", *VDE*, 1-5, 2014.
9. X.-Y. Gao, W. Ding, Y. Zhou, C. Lei, Y. Cao, and H. Choi, "An integrated solenoid-type inductor with electroplated Ni-Fe magnetic core", *Electromagnetic Field Computation Conference*, 138, 2006
10. D. W. Lee, K.-P. Hwang, and S. X. Wang, "Fabrication and Analysis of High-Performance Integrated Solenoid Inductor With Magnetic Core", *IEEE Transactions on Magnetics*, 44 (11), 2008
11. H. Jia, J. Lu, X. Wang, K. Padmanabhan, and Z. J. Shen, "Integration of a Monolithic Buck Converter Power IC and Bondwire Inductors With Ferrite Epoxy Glob Cores", *IEEE Transactions on Power Electronics*, 26 (6), 1627-1630, 2011
12. R. P. Davies, C. Cheng, N. Sturcken, W. E. Bailey, and K. L. Shepard, "Coupled Inductors With Crossed Anisotropy CoZrTa/SiO2 Multilayer Cores", *IEEE Transactions on Magnetics*, 49 (7), 4009-4012, 2013
13. N. Wang, T. O'donnell, S. Roy, P. Mccloskey, and C. O'mathuna, "Micro-inductors integrated on silicon for power supply on chip", *Journal of Magnetism and Magnetic Materials*, 316 (2), E233-E237, 2007
14. R. Meere, N. Wang, T. O'donnell, S. Kulkarni, S. Roy, and S. C. O'mathuna, "Magnetic-Core and Air-Core Inductors on Silicon: A Performance Comparison up to 100 MHz", *IEEE Transactions on Magnetics*, 47 (10), 2011
15. N. Wang, E. J. O'sullivan, P. Herget, B. Rajendran, L. E. Krupp, L. T. Romankiw, B. C. Webb, R. Fontana, E. A. Duch, E. A. Joseph, S. L. Brown, X. Hu, G. M. Decad, N. Sturcken, K. L. Shepard, and W. J. Gallagher, "Integrated on-chip inductors with electroplated magnetic yokes (invited)", *Journal of Applied Physics*, 111 (7), 2012
16. D. V. Harburg, G. R. Khan, F. Herrault, J. Kim, C. G. Levey, and C. R. Sullivan, "On-chip RF power inductors with nanogranular magnetic cores using prism-assisted UV-LED lithography", *17th transducers & Eurosensors conference*, 701 - 704, 2013
17. R. Hahn, S. Krumbholz, H. Reichl, *Low profile power inductors based on ferromagnetic LTCC technology*, in *56th Electronic Components & Technology Conference 2006, Vol 1 and 2, Proceedings*. 2006. p. 528-533.

18. B. Orlando, R. Hida, R. Cuchet, M. Audoin, B. Viala, D. Pellissier-Tanon, X. Gagnard, and P. Ancey, "Low-resistance integrated toroidal inductor for power management", *IEEE Transactions on Magnetics*, 42 (10), 3374-3376, 2006
19. D. Flynn and M. P. Y. Desmulliez, "Design, Fabrication, and Characterization of Flip-Chip Bonded Microinductors", *IEEE Transactions on Magnetics*, 45 (8), 3055-3063, 2009
20. P. Kamby, A. Knott, M. A. E. Andersen, and I. I. E. Society, "Printed Circuit Board Integrated Toroidal Radio Frequency Inductors", *38th Annual Conference on IEEE Industrial Electronics Society (IECON 2012)*, 680-684, 2012
21. J. Li, K. D. T. Ngo, G.-Q. Lu, and H. Xie, "Wafer-level fabrication of high-power-density MEMS passives based on silicon molding technique", *Integrated Power Electronics Systems Conference (CIPS 2012)*, 1 - 5, 2012
22. J. Qiu and C. R. Sullivan, "Radial-Anisotropy Thin-Film Magnetic Material for High-Power-Density Toroidal Inductors", *Integrated Power Electronics Systems Conference (CIPS 2012)*, 1 - 6, 2012
23. J. Kim, J.-K. Kim, M. Kim, F. Herrault, and M. G. Allen, "Microfabrication of toroidal inductors integrated with nanolaminated ferromagnetic metallic cores", *Journal of Micromechanics and Microengineering*, 23 (11), 2013
24. X. Fang, R. Wu, L. Peng, and J. K. O. Sin, "A Novel Silicon-Embedded Toroidal Power Inductor With Magnetic Core", *IEEE Electron Device Letters*, 34 (2), 292-294, 2013
25. X. Yu, J. Kim, F. Herrault, and M. G. Allen, "Silicon-embedded toroidal inductors with magnetic cores: Design methodology and experimental validation", *Applied Power Electronics Conference and Exposition 29th (APEC) 2014*, 763 - 767, 2014
26. Agilent Technologies, *Impedance measurement handbook*, 2009